Research on Manufacturing Mirror Segments for an Extremely Large Telescope

This thesis is submitted for the Degree of Doctor of Philosophy of the University College London (UCL)

by

Hongyu Li

Department of Physics & Astronomy

University College London

April 2012

I confirm that the work presented in this thesis is my own. Where information has been derived from other sources, I confirm that this has been indicated in the thesis. The 'tool lift' software and initial experiment were developed by Zeeko Ltd before the ESO segment tender, and solid rubber tools were optimised by the Design Team at OpTIC Glyndwr, following a prototype by Zeeko Ltd. The experimental optimisation of parameters, data analysis, modelling and interpretation were conducted by the author.

Signed: *Hongyu Li*
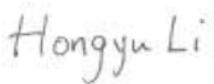
Hongyu Li

19 June 2012

Abstract

This thesis concentrates on the development of a process-chain for the manufacture of the mirror segments for the European Extremely Large Telescope (E-ELT). This revolutionary scientific project with a 39.3m primary mirror will be the largest optical/near-infrared telescope in the world. The primary mirror design consists of 798 aspheric hexagonal segments, each 1.44 metres across-corners, but only 50mm thick. The manufacture of these aspheric segments poses many challenges. Edge mis-figure is regarded as one of the most difficult technical issues for segment production, impacting directly on the telescope's science output, such as the detection of extrasolar terrestrial planets. The other challenge is how to speed up the process for the manufacture of almost 1000 segments in a reasonable time and cost.

The *'Precessions'* polishing technique is an advanced polishing method with high precision and efficiency. To achieve the specification of E-ELT's segments, there are some key techniques that need to be researched, such as: edge control, removal of mid-spatial frequency errors and a massive improvement in process speed c.f. classical methods. The research work in this thesis contributed to the delivery of an effective process, including the characterisation of tool influence functions for the *'Precessions'* technique; optimisation of the process parameters; edge control; diagnoses of edge asymmetry of hexagonal parts, and speeding-up the whole process. Two process-chains giving substantially different depths of removal have been developed and demonstrated on a hexagonal Zerodur part (200mm across-corners) with edge control, and the results meet the E-ELT specification. As a result, different top-level strategies for addressing the manufacture have been considered, leading to a preferred direction for the research.

Contents

Chapter 2

Review of aspheric surface polishing and figuring techniques 65

Chapter 3

'*Precessions*' polishing 85

Chapter 6

Diagnoses of edge asymmetry of a hexagonal part 159

Chapter 7

Experimental demonstration of the process-chain.............................. 178

Chapter 8

Conclusion and future work **196**

Appendix **203**

List of Publications **204**

Bibliography **205**

List of Abbreviations

ALOT — Advanced Large Optical Telescope

AJP — Abrasive Jet Polishing

CAD — Computer Aided Design

CCP — Computer Controlled Polishing

COM — Centre for Optics Manufacturing

CNC — Computer Numerical Control

CTE — Coefficient of Thermal Expansion

DOF — Degree of Freedom

E-ELT — European Extremely Large Telescope

ESO — European Southern Observatory

FEA — Finite Element Analysis

FJ — Fluid Jet

GMT — Giant Magellan Telescope

GTC — Gran Telescopio Canarias

HET — Hobby-Eberly Telescope

IBF — Ion Beam Figuring

IRAS — Infrared Space Astronomical Telescope

JWST — James Webb Space Telescope

MRFJ	Magneto-Rheological Fluid Jet
MMT	Multiple Mirror Telescope
MRF	Magneto-Rheological Finishing
MSS	Master Spherical Segment
NPL	National Physical Laboratory
PV	Peak-Valley
RAPT	Reactive Atomic Plasma Technology
RMS	Root Mean Square
SALT	Southern African Large Telescope
SAP	Swing Arm Profilometer
SiC	Silicon Carbide
SNR	Signal to Noise Ratio
SRT	Solid Rubber Tool
TIF	Tool Influence Function
TMT	Thirty Meter telescope
TPG	Tool Path Generator
ULE	Ultra Low Expansion
VLT	Very Large Telescope
VP	Virtual Pivot

List of Figures

List of Tables

Acknowledgements

This thesis would not have been possible without the help and support of many people around me. Therefore, here is my long list – thanks everybody.

First and foremost, a special thanks to my family for their support and great patience throughout my studies.

I would like to express my sincere gratitude to my primary supervisor Professor David Walker for giving me the opportunity to undertake this PhD and for his continuing support in all aspects over the last three years. His knowledge and guidance has been invaluable, his passion to science has been infectious and made my entire PhD experience enjoyable.

A special thanks goes to Dr. Guoyu Yu for his endless help in many ways. Without his assistance in many things in the year I was a PhD candidate, this study would not have been possible. I thank Professor Tegid Jones and Dr. Giorgio Savini for their helpful comments and support during my studying. Thank Angela Cooper from UCL Language Centre for correcting my English during writing my thesis. Thank also Professor Alan Smith and Professor Gordon Love for their valuable time to read and correct my thesis, and encouragement during my viva.

In my daily work, I have been blessed with a friendly and cheerful group at OpTIC Glyndwr and I have received many helps from them. I specially thank Mike Parry Jones, he was very generous with his personal time to read my thesis and provided valuable feedback and advice. He has always been patient to correct my English. Ian Baker helped me with ANSYS software. Rob Evans assisted me with the ADE white-light texture interferometer. Andy Sayle helped me to set up force measurement device. Seraj Hamidi gave me many useful suggestions in my thesis. Also a thank you to everyone in the ESO Project team at OpTIC Glyndwr for their support and help:
Tony Fox-Leonard, Caroline Gray, Paul Rees, John Mitchell, Gary Davies, Steve Waine, Colin Philips, Pim Messelink, Matthew Bibby, Keith Stutter, Carolyn Atkins and Samantha Thompson.

I would like to acknowledge the financial support from OpTIC Glyndwr Ltd. and the department of Physics and Astronomy, UCL, which enabled me to undertake this study. I also acknowledge the support given to me by my University (Harbin Institute of Technology, China) by granting me study leave to complete this PhD degree.

When I consider thy heavens,

The work of thy fingers,

The moon and the stars

Which thou hast ordained,

What is man, that thou art mindful of him?

Psalm 8:3, 4

Chapter 1

Introduction

'(I have seen) stars in myriads, which have never been seen before, and which surpass the old, previously known, stars in number more than ten times. But that which will excite the greatest astonishment by far… and which indeed especially moved me to call the attention of all astronomers and philosophers, is this, namely, that I have discovered four planets, neither known nor observed by any one of the astronomers before my time' (Galileo, 1610).

Galileo invented the first astronomical telescope to observe the sky, and discovered Jupiter's four major satellites. His startling discoveries were described in the book, *Sidereus Nuncius* (usually translated into English as *Sidereal Messenger*), which was published in March 1610 (Barker, 2004).

From the time of the earliest developments of the telescope in the 17th century, optical elements have steadily increased in size. This is because these telescopes with a large primary mirror are capable of gathering more light and achieving high image resolution (Canales et al., 2006). Monolithic primary mirrors for ground-based optical/near-infrared telescopes have probably reached their limit with the 8.4m diameter mirror today (Martin et al., 2004 and 2006; Walker et al., 2011A).

The next generation of optical/infrared telescopes, collectively known as Extremely Large Telescopes (ELTs), will see primary apertures greater than 20m. This is a huge increase over

the current 8-10m facilities and will revolutionise ground-based capabilities, increasing photon collecting power and theoretical angular resolution (Gilmozzi, 2004).

The European Extremely Large Telescope (E-ELT) is a revolutionary scientific project with a 39.3m primary mirror telescope that will be the largest optical/near-infrared telescope in the world and will gather 13 times more light than the largest optical telescopes existing today (Ramsay et al., 2010). The primary mirror design consists of 798 aspheric hexagonal segments, each 1.44 metres across-corners, but only 50mm thick. The manufacture of these aspheric segments poses many challenges. The research work in this thesis has been involved in developing an advanced process for the fabrication of the E-ELT segments.

1.1 Overview of this thesis

1.1.1 Outline of this thesis

Chapter 1 gives an introduction to the subjects involved.

Chapter 2 summarises various aspheric surface polishing techniques currently employed to fabricate segments.

Chapter 3 describes the '*Precessions*' polishing technique in detail.

Chapter 4 characterises tool influence function based on modelling and measurement.

Chapter 5 presents three edge control techniques for the fabrication of E-ELT segments by experiments.

Chapter 6 diagnoses the edge asymmetry of a hexagonal part and a strategy that can avoid the edge asymmetry is given and verified by experiments.

Chapter 7 demonstrates the whole process-chain for the fabrication of E-ELT segments and reviews the results with comparison to E-ELT specification.

Chapter 8 summarises the work done and suggests future work.

1.1.2 Contribution of this thesis

This thesis concentrates on developing the processes for the production of E-ELT's prototype segments, and aims to achieve ESO's specification (discussed in **Section 1.9**). The E-ELT segment process-chain is described in **Figure 1.1**. The research work in this thesis is helping to deliver an effective process. The original academic contributions that have been made to the subject in this dissertation are as follows:

1. Different top-level strategies for addressing the manufacture have been considered, leading to a preferred direction for the research.

2. The tool influence functions (TIFs) characterise the local effect of the process and therefore is of fundamental importance. TIFs have been characterised based on computer simulation and experimentation, which helps to achieve a successful deterministic '*Precession*' process. (in **Chapter 4**)

3. Two novel edge control techniques for segments are demonstrated. For the 'tool lift' edge control technique, to obtain the full tool influence function at the edge, a novel hybrid-measurement method is presented, which uses both simultaneous phase interferometry and profilometry. (in **Chapter 5**)

4. A strategy that can avoid edge asymmetry is given and verified by experiments. (in **Chapter 6**)

5. Two possible process-chains giving substantially different depths of removals have been developed and demonstrated on a hexagonal Zerodur part (200mm cross-corners) with edge control, and the results meet the E-ELT specification. (in **Chapter 7**)
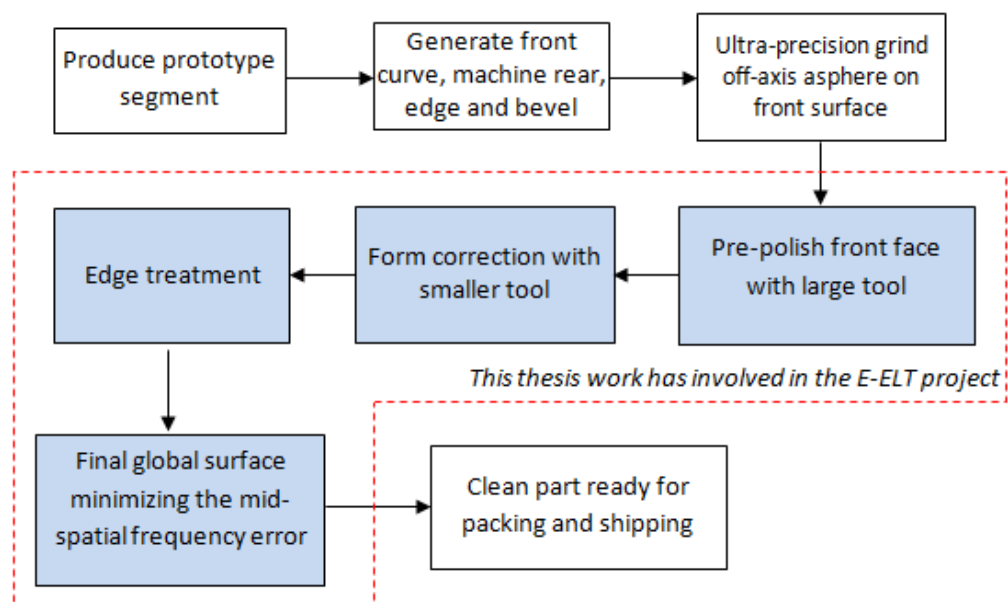
Figure 1.1 The contribution of this thesis for the E-ELT project (drawn by the author)

1.2 Science drivers for E-ELT

Although this thesis is not about astronomy, it is useful to understand the science drivers for the next generation of telescopes. This provides the context for the research in mirror fabrication.

Since the invention of the telescope, generations of astronomers have expanded the boundaries of the known universe ever further. The largest telescopes in operation today have primary mirrors of 8-10 m in size. Since 1995, using these telescopes, astronomers have discovered over 300 planets outside our solar system and have made the first direct image of giant self-luminous planets orbiting nearby stars (Cunningham, 2009).

Now astronomers want to detect extra-solar terrestrial planets and the first generation of stars and galaxies. The enormous improvements in light gathering power and image resolution to be offered by E-ELT will have a profound effect on scientific observations as follows:

1. The habitable zone is the narrow region in a planetary system where water exists in liquid form, which is a prerequisite for life as we know it. For over a decade, we have known that exoplanets exist, but we have not yet been able to detect the faint signatures of Earth-like planets directly (Gilmozzi, 2004). The E-ELT will have the resolution to obtain the first direct images of such objects, and even analyse their atmospheres for the biomarker molecules (such as oxygen, ozone, water, methane and nitride) that might indicate the presence of life (Hook, 2004).

2. Trying to understand galaxy formation and evolution has become one of the most active fields of astronomical research of the last few decades, as large telescopes have reached out to high redshifts. Yet distant galaxies cannot be resolved into individual stars. The unique angular resolution (50 milliarcsec at 10 um wavelength) of the E-ELT

will revolutionise this field by allowing us to observe individual stars in galaxies out to distances of tens of millions of light-years (Hook et al., 2005 and Pantin, 2012).

3. Black holes have excited physicists and astronomers since they were first postulated in relativistic form a century ago by Karl Schwarzschild (Celotti et al., 1999). Observations have implied that these bizarre objects exist and on a grand scale (Hook et al., 2005). However, it is not known how supermassive black holes grow and what their role is in the formation of galaxies.

4. For the first 380 000 years after the Big Bang, the Universe was so dense and hot that light and matter were closely coupled. Only after the Universe had expanded and cooled sufficiently, could electrons and protons 'recombine' to form the simplest element, neutral hydrogen, and photons could decouple from matter. Only then could the first stars form and start to become organised into large structures. The E-ELT will allow scientists to look all the way back to these times to see how this phase of astrophysical evolution began (Hook 2004 and Hook et al., 2005).

To answer these exciting questions, a telescope with a substantial advantage in Signal to Noise Ratio (*SNR)* over the state-of-the-art is crucial for observing the fainter and more distant objects. The *SNR* of a telescope is expressed as (Roggemann et al., 1994):

$$SNR = \frac{N}{\sqrt{N_S + N_B + N_R^2 + N_T}}$$

Where, *N* is the integrated photon signal from the object;

$\sqrt{N_S}$ is the shot noise from the source;

$\sqrt{N_B}$ is the background shot noise;

N_R is the readout noise;

$\sqrt{N_T}$ is the thermal noise.

Now that detectors approach the fundamental limits of performance, the *SNR* of the telescope can be increased by three main factors:

1. Increasing the aperture of the primary mirror to collect more signals from the object

2. Increasing the quality of the surface of the optics to sharpen the image and improve contrast against the background

3. Reducing the degradation of image due to effects of the atmosphere, through adaptive optics (see **Section 1.7**)

Three ELT projects have been proposed: the Thirty Meter Telescope (TMT) (Sanders, 2008), the Giant Magellan Telescope (GMT) (Martin et al., 2004) and the European Extremely Large Telescope (E-ELT) (Ramsay et al., 2010). The E-ELT with a 39.3m primary mirror (consisting of 798 aspheric hexagonal segments) will be the largest ground-based telescope in the world. The specification of manufacture of these segments (as discussed in **Section 1.9.2**) is extremely challenging. The **Figure 1.2** shows the E-ELT compared to TMT and GMT.

Figure 1.2 E-ELT compared to other future ELTs (pictures are from GMT, TMT and E-ELT project website and put together by author, 2011)

1.3 Evolution of ground telescopes

The very first telescopes were believed to have begun to appear around the year 1608 (NPG, 2001). These early refracting telescopes consisted of a convex objective lens and a concave eyepiece. Galileo invented the first astronomical telescope to observe the sky, and discovered Jupiter's four major satellites. His telescope also enabled Galileo to produce the first maps of the Moon, revealing its rough terrain (NPG, 2001).

However, the main disadvantage of the refractors was the tendency for the object glass to focus different wavelengths of light at different distances, causing them to produce rings of false colour around stars and planets (chromatic aberration). The optical theory of the refractor made no advance after Galileo because the physical origin of the dominant colour aberration was not understood, which blocked further development of the refractor for over 50 years (Wilson, 2004).

In 1663, Scottish mathematician, James Gregory, pointed out that a reflecting telescope with a mirror that was shaped like part of a conic section would correct spherical aberration, as well as avoiding the chromatic aberration seen in refractors. He designed the first reflecting telescope, composed of a concave parabolic primary mirror with a central hole and a concave ellipsoid secondary mirror as shown in **Figure 1.3**. Gregory's design proved extremely difficult to build because of the fabrication of aspheric elements (NPG, 2001). Therefore, his early attempts to build the telescope failed, since he could find no optician capable of actually constructing one.
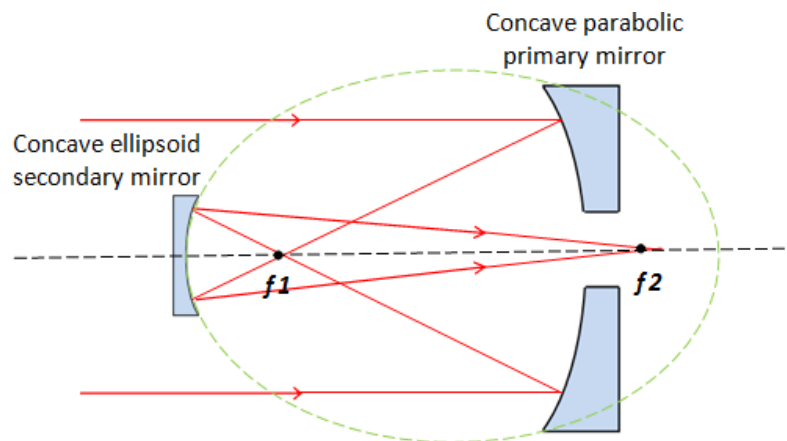
Figure 1.3 Gregorian reflecting telescope design, where the primary mirror is a concave parabolic and the secondary mirror is a concave ellipsoid. The secondary mirror relays the conjugated *f 1* to *f 2*, which is geometrically perfect on-axis (drawn by the author)

However, his idea was not forgotten; three and a half centuries later this idea became the basis for some reflection telescopes. Compared to Cassegrain telescopes (introduced in the following section), Gregorian telescopes have the advantage of a real exit pupil, a position along the beam path where the secondary forms an image of the primary mirror surface. A larger primary-to-secondary distance is a structural disadvantage, especially for large instruments (Stark et al., 1997). Currently, there are several large modern telescopes that use the Gregorian configuration, such as the Vatican Advanced Technology Telescope, the Magellan telescopes, the Large Binocular Telescope (Martin et al., 2006) and the Giant Magellan Telescope (Martin et al., 2004).

In 1671, Isaac Newton simplified Gregorian's design and built the first reflective telescope (Wilson, 2004). His simple construction based on the use of a concave spherical primary mirror instead of a parabolic mirror and a flat diagonal tilted secondary instead of a concave elliptical mirror. Though this could not avoid the spherical aberration, a spherical primary mirror is sufficient for high visual resolution at focus ratios of *f/8* or longer (Wilson, 2004). Today, the

modern Newtonian design has a parabolic primary mirror. The Newtonian reflecting telescope

design is shown in **Figure 1.4**.
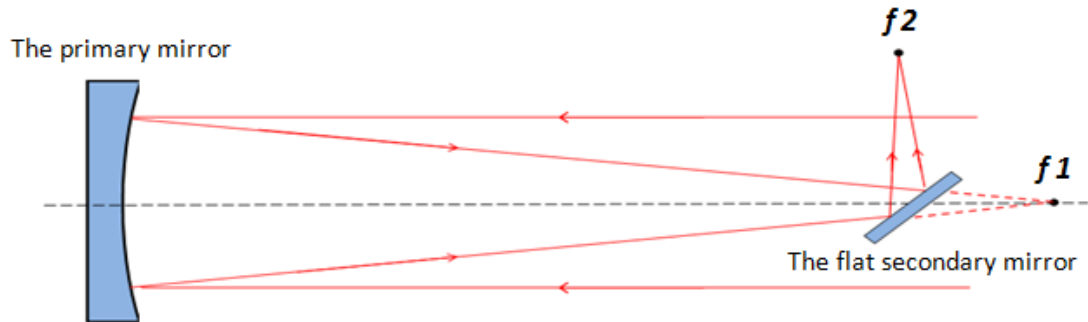
Figure 1.4 Newtonian reflecting telescope design, where, in the original design, the primary
mirror is spherical concave mirror. The modern Newtonian primary mirror is parabolic. The
light from infinity relays at the focus of the parabolic primary mirror *f1,* which is geometrically
perfect on-axis (drawn by the author)

The aspheric shapes are very difficult to produce. In fact, astronomers would have to wait until

1721 for Hadley to grind the first non-spherical telescope mirror (Wilson, 2004).

In 1672, another reflecting telescope, invented by French sculptor Cassegrain is more

convenient, whose design is shown in **Figure 1.5**. The secondary mirror is convex and placed

between the primary mirror and its prime focus; this makes the telescope more compact. The

combination of concave and convex mirrors also reduces the off-axis aberrations introduced

by the primary mirror. The reduction in the overall length of the Cassegrain telescope

(compared to the Newtonian telescope) directly reduces the size of its construction and dome,

with a consequent saving of cost. Thus, the Cassegrain telescope quickly became popular for

astronomical use (NPG, 2001).
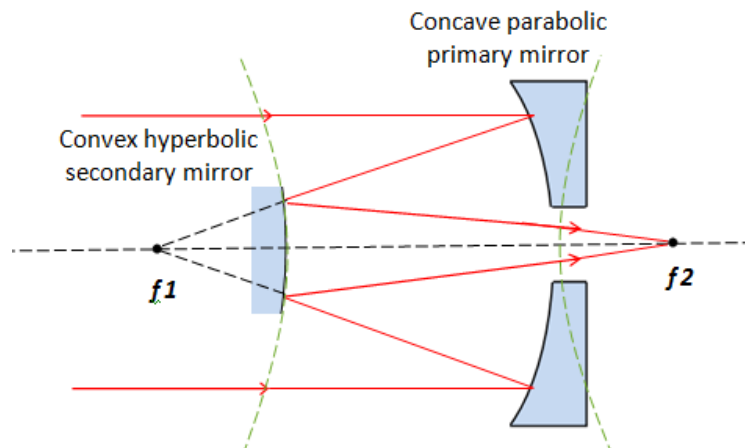
Figure 1.5 Classical Cassegrain reflecting telescope design, where the primary mirror is a concave parabolic and the secondary mirror is a convex hyperbolic. The secondary mirror relays the conjugated *f 1* to *f 2,* which is geometrically perfect on-axis (drawn by the author)

The classical system is not affected by spherical aberration. However, it is perfect only on axis and suffers from coma, an optical aberration of the parabolic primary mirror. Coma causes a point source off the centre of the field to be spread out into a comet shaped image. A modification of classical Cassegrain was proposed by Schwarzschild in 1905 and fully developed by Ritchey and Chretien in 1910 (Bely, 2003). It is called the Ritchey-Chretien system, in which both the primary and secondary mirror are hyperbolic. This configuration could correct the coma over a large field while retaining freedom from spherical aberration.

For much of the time since the earliest developments of the telescope in the 17th century, the evolution of the telescope was very slow. At the beginning of the 20th century, the primary mirror diameter scarcely exceeded one meter (Enard et al., 1996). The essential technical difficulties in producing the primary mirror, the cost and the construction time, were the main limitations to progress in this field, see **Figure 1.6**. Each advance in telescope aperture has

provided unexpected observation on the threshold of detection, which has driven the science

case for yet larger telescopes.
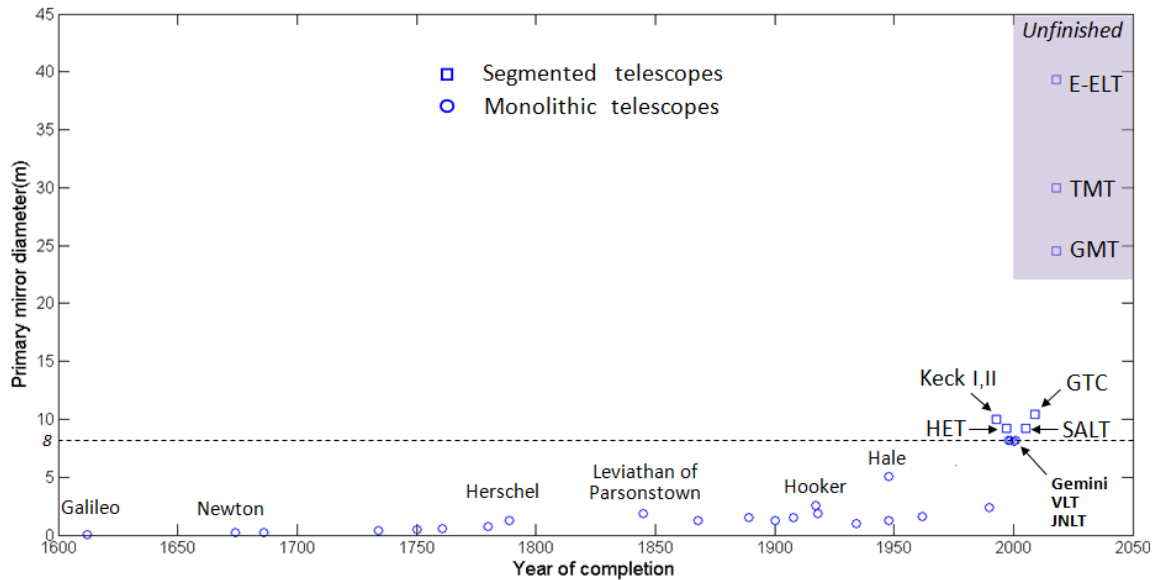
Figure 1.6 Increase in telescope diameters over time. E-ELT with 40m primary mirror will be the largest ground -based telescope in the world (graph by the author)

The Hale 5.1m telescope went into operation in 1948, at the Palomar Observatory in California (Baade, 1948). It was the world's largest telescope for 45 years (1948-1993) until the construction of the Keck I in 1993. It is still a workhorse of modern astronomy. It represented the culmination of continual telescope design improvements since the invention of the reflecting telescope (Tokunaga et al., 2006). **Figure 1.6** shows the increases in telescope aperture over time. After the completion of the Hale telescope, astronomers recognized that building a larger telescope would require completely new approaches. Simply scaling classical techniques would lead to a primary mirror that would be too massive, and an observatory (including the dome enclosure) that would be too costly to build (Tokunaga et al., 2006).

Since 1990s, computer technology has developed to enable light-weight mirror design and active control in use, and a number of ground-breaking approaches have been tried and several 8m generation telescopes have been built (VLT, JNLT, and Gemini) (Iye et al., 1994 and Oschmann et al., 1997). However, with technology limited (see **Section 1.4.1**), 8.4m seems to be the practical maximum diameter for monolithic mirrors. Therefore, due to these limitations, increasing the aperture diameter of an optical telescope by scaling it up is not a realistic solution, transportation is a key issue (Flores et al., 2003).

Nelson (2000) and Malacara et al., (2001) who were interested in building a large telescope for increasing resolution and light-gathering capabilities, adopted mirror segmentation. This approach avoids the overwhelming challenges of manufacturing and shipping a large monolithic primary mirror. Segmented mirrors have successfully been applied in Keck I&II, HET, SALT and GTC telescopes (Geyl et al., 2004 and Semenov et al., 2004). They will be introduced in the following section.

1.4 Segmented mirror

A segmented mirror is an array of smaller mirrors designed to act as elements of a single large curved mirror. The segments can be either spherical or aspheric. The idea of the segmented mirror was originally from Guido Horn D'Arturo, director of the Bologna Observatory in 1932 (Marra, 2000). The necessary technologies were initially developed under the leadership of Jerry Nelson at the Lawrence Berkeley National Laboratory and University of California during the 1980s, and have since spread worldwide to the point that essentially all future large optical telescopes plan to use segmented mirrors (Mast et al., 1982 and Nelson 2005).

1.4.1 The needs for segmented mirrors

As mirrors grow to such large sizes (above 8m), they become extremely difficult to produce. This is because of the technological limit of a primary mirror made of a single rigid piece of glass (Jones, 1982). Using a monolithic mirror much larger is prohibitively expensive due to the cost of both the mirror and the massive structure needed to support it. A mirror beyond that size would also sag more under its own weight as the telescope was rotated to different positions, changing the precision of the surface and requiring a more complex support system.

Monolithic mirrors larger than the current 8m generation are impractical to produce, and would set severe constraints on the design of their support structures, to maintain their shape and alignment (Kendrick, 2009). This is because:

1. The transportation for such huge mirrors is impractical (maybe impossible), shipping is limited by the road infrastructure(e.g. bridge)

2. The mirror support and handling system become very delicate

3. It is difficult to cast the mirror blank and retain homogeneity of the material

4. It needs special equipment for polishing

As a result, segmentation seems to be the only promising solution to reach diameters of 20m and beyond (Storm et al., 2003). Small segments are easier to manufacture and transport than a large monolith. They can be much thinner and lighter, reducing the overall weight and cost of the mirror and maintaining their shape more easily.

1.4.2 History of segmented mirror telescope

Hence, the idea of a segmented mirror was proposed in 1932 and Guido Horn D'Arturo, created a 1.8-meter mirror composed of 61 hexagonal tiles 20 cm across in 1950 (Marra, 2000). The mirror was static and could be used only horizontally.

In 1970, Pierre Connes in France made a 4.2m segmented mirror telescope for infrared astronomy. It was fully steerable, and active. Unfortunately, the optical quality was too low to be useful for astronomy (Nelson, 2005).

Another type of segmented mirror telescope was developed in the 1970s and completed early in 1980s. This was called the Multiple Mirror Telescope (MMT), and was built in southern Arizona. The telescope was made of six 1.8m primary mirrors, each axisymmetric and circular (Nelson, 2005).

In the late 1970s, a very ambitious project to build a 10 m diameter segmented mirror telescope was begun, called the Keck Observatory. This project was formally started in 1984 and completed and began science observation in 1993 (KECK, 2011). Due to the success of Keck I telescope, Keck II was completed in 1996. The success of the Keck telescopes led to building of HET, SALT and GTC telescopes. They are the largest telescopes in operation today. The details are introduced in the following section.

1.4.3 The current large segmented telescopes

1. Keck I and II Telescopes (USA, 1993 and 1996)

Large scale segmentation was first implemented successfully in the optical and near IR Keck I and II telescopes, which were commissioned in 1993 and 1996 respectively at Mauna Kea, Hawaii, USA. Their primary mirrors are made of 36 hexagonal 1.8m across-corners segments, for an effective aperture of approximately 10m, making them at that time the largest optical telescopes in the world, although superseded by the Gran Telescopio Canarias (Nelson et al., 1994). **Figure 1.7** shows a picture of the primary mirror of the Keck telescopes (KECK, 2011).

Figure 1.7 Keck I & II 10m telescopes: up, the telescopes inside their enclosures; bottom, front view of the segmented M1 (Keck, 2011)

2. The Hobby-Eberly Telescope (HET, USA, 1997)

The Hobby-Eberly Telescope (HET) is orientated at a fixed elevation with a segmented spherical primary mirror array and a moving star tracker at the prime focus to follow astronomical objects. The stars are tracked by moving the instrument package to follow the image as seen in the stationary primary mirror. The attitude of the telescope structure is fixed at 35° to the zenith and the telescope is able to be rotated through 360° in azimuth to access different regions of the sky. The final image is formed by a 4-mirror double-Gregorian spherical aberration corrector (Palunas et al., 2006). The HET was designed to be the prototype for the construction of an extremely cost-effective large telescope and was completed in 1997. The HET is located at the McDonald Observatory in West Texas. The primary mirror of the HET is about 11m by 9.8m and composed of 91 spherical segments. All segments are identical regular hexagons with 1m edge to edge (as shown in **Figure 1.8**). At any given time, not all the primary area is used, and the effective aperture is 9.2m (Krabbendam et al., 1998).

Figure 1.8 Hobby-Eberly Telescope (HET) (HET, 2011)

3. The Southern African Large Telescope (SALT, South African, 2005)

The Southern African Large Telescope (SALT) was planned to be a copy of the HET i.e. fixed-altitude, segmented spherical primary mirror with an aperture of approximately 11m x 10m. All 91 segments are identical regular hexagons with 1m edge to edge (as shown in **Figure 1.9**). The SALT was funded by a consortium of international partners including South Africa, the

United States, Germany, Poland, India, the United Kingdom and New Zealand (Meiring et al., 2003). The construction phase of the SALT was completed at the end of 2005 at Sutherland, South Africa.

Figure 1.9 South African Astronomical Observatory (SALT, 2011)

4. Gran Telescopio Canarias (GTC, Spain, 2009)

Gran Telescopio Canarias (GTC), inaugurated in 2009, is based on a design very similar to that of Keck, with a slightly larger segmented primary mirror of 10.4m diameter (75 square meters light collecting surface) (Alvarez et al., 2010). It is currently the biggest telescope in the world and located at one of the best astronomical sites in the Northern Hemisphere: La Palma in the Canary Islands. The GTC primary mirror is made up of 36 hexagonal segments. GTC is the last of the so-called generation of 8-10 meter telescopes, as shown in **Figure 1.10**.

Figure 1.10 Gran Telescopio Canarias (GTC) (GTC, 2011)

1.4.4 Challenges for the segmented mirror

A segmented mirror has several advantages such as lower blank cost, ease in handling and transporting and less risk of breakage, simpler coating equipment and the telescope is more lightweight and compact. However, segmented mirrors present their own set of challenges (Amodei et al., 2003 and Nelson, 2005). These challenges are discussed in the following paragraphs:

1.4.4.1 Segments are difficult to polish

The fabrication of the individual segments poses certain problems. Segments are usually fabricated such that together, their surfaces match those of their parent monolithic mirror. As the primary mirrors of the next generation of telescopes will be aspheric, the asphericity of segments grows as they are located further away from the vertex of the primary mirror and all the segments will be off-axis sections of the desired aspheric surface (Bastaits, 2010). Segments are no longer all identical and have slightly different radii of curvature and aspheric profiles. The primary mirror of E-ELT has been designed with 6-fold symmetry. There are 133 families of identical segments. The details are discussed in **Section 1.9.1**. Furthermore, a curved surface cannot be tessellated with identical hexagons and achieve uniform gaps. Either the hexagons will not be regular or the gaps will vary. Therefore, the fabrication processes cannot rely on figure symmetry. Polishing an aspheric surface is difficult because polishing traditionally only works well when the polishing tool fits the glass surface, to obtain the desired smoothness (Nelson, 2005). In addition, the segments must have a good figure right to their edges. Significant edge errors are unacceptable for segments since the edges would be in the aperture of the composite mirror produced by the segments. The edge effect is introduced in **Section 1.5**.

1.4.4.2 The diffraction effect

The segment's edges and inter-segment's gaps will introduce diffraction effects (Troy and Chanan, 2003). A monolithic mirror produces a circular symmetric Airy pattern. The diffraction effect of segmented mirrors is complicated. The gap and the segment edge mis-figure produce a regular pattern of the higher-order diffraction peaks (Espinosa et al., 1997 and Yaitakova et al., 2003).

1.4.4.3 Segments increase infrared emissivity

In the infrared region, with wavelengths longer than 2.2μm, the thermal emission from the environment (including the telescope and optics) becomes an important source of background noise (Nelson, 2005). The infrared emission is derived based on the Stefan-Boltzmann law (heat radiation law), and increases as T^4, T being the temperature (K) of the object surface (Lin et al., 2011). An extra-solar terrestrial planet will be at similar temperature to the telescope and so has a similar black body spectrum. Thus, the infrared emission from the telescope could dominate the faint planet.

Bevels are typically added to the mirror to avoid chipping of the edges, and the air gaps between segments are there to avoid mirrors touching each other during installation and removal. There is also an additional thermal background effect due to material behind the gaps between the segments. Therefore, segmentation of the mirror increases the infrared emissivity of the telescope.

1.4.5 Hexagonal mirror segmentation

Generally, there are two patterns of segmentation geometry: 'petals' and hexagon, as shown in **Figure 1.11**. The 'petals' pattern is tessellated using annular rings, which provide a maximum of identical segments. This geometry was used for ALOT (Advanced Large Optical Telescope, A 4 - meter space telescope, NASA) (Bely, 2003). The hexagonal segmentation was used for Keck I&II, HET, SALT and GTC telescopes.

Figure 1.11 Segmentation with 'petal' (left) and hexagon (right) (Bely, 2003)

There are significant advantages of choosing the hexagonal section. This is because it is possible to fill the entire aperture with segments that have similar dimensions, therefore, making mirror cell design, handling and maintenance easier. In the segmented mirror, the gaps between the segments should be as small as possible to ensure best possible performance in the infrared observations. Segmentation with a hexagonal shape is able to achieve the minimum gaps (Anderson et al., 2003 and Nelson, 2005). The segments are supported on whiffletrees that have 120° (triangular) symmetry. Therefore, it is convenient to preserve the triangular symmetry for the structural design of the primary mirror cell, because it makes it

possible to apply a systematic and regular structure. Furthermore, the corners of a hexagon are easier to polish than triangular or square shapes.

The choice of the segment size is mainly a cost minimisation issue. Large segments are thicker and hence the blank cost is larger and mechanical supports more complex. Small segments increase the number of edge sensors and amount of associated electronics. Small segments also increase the total length of edges and area of the gaps of the primary mirror. The segmentation of the primary mirror must be optimised in a trade-off of cost, weight and performance (Edward et al., 1998).

1.5 Edge effect of segmented mirrors

A segmented mirror introduces a serious issue that is the mirror edge effect (Zeiders et al., 1998; Troy et al., 2003; Wang et al., 2007; Yaitakova et al., 2011). The edge effect can adversely affect the science mission performance by:

1. Increasing the diffraction effect (side-loads to image)

2. Increasing the total scattered light and background noise (infrared emission)

3. Reducing the wave front quality or total clear aperture due to edge roll-off

The edge effect is a serious contributor to light diffusion around the central spot of the image delivered by a segmented aperture telescope. This would make the detection of faint objects much more difficult, i.e. exoplanets, close to bright stars. Such a type of discovery is one of the main motivations to construct large (>10m) telescopes; it is therefore clear that great attention should be given to such an edge effect (Geyl et al., 2004). The turned edge could be marked with black paint, however, that paint would be at about 280K and would radiate infrared emissions as well.

Most polishing techniques induce a surface error at the edge of the mirror, which is generated by the non-continuity of the surface, and the boundary conditions of the pressure field applied to the edge of the part under polishing (Guo et al., 2006, Kim, et al 2009, Hu et al., 2011 and Ruch, 2011). This sudden-edge effect tends to be localized in the last millimetres of the mirror surface.

The edge effect significantly dominates the performance of the segmented-mirror telescope. This is because the total length of the edge of the segmented optical systems is much longer compared to the conventional system with one mirror. For example, there are near 4000m in total length of edges in the E-ELT's primary mirror. These edges are distributed across the whole pupil.

1.6 Mirror materials for ELTs

1.6.1 A brief history of mirror materials

Early reflecting telescopes were made with metal mirrors (speculum), because they were easier to make than glass, and in any case, at that time, there was no process for silvering glass. Once figured and polished, these metal mirrors would begin to corrode after only a few months, whereupon it would need to be polished again. In 1835, a process for depositing a layer of silver on glass was developed by the German chemist, Justus Leibig (Tobin, 1987). This was a major step forward because when the silver tarnished, it could be chemically removed and a new layer redeposited without altering the curvature of the mirror, due to the chemical stability of glass. Material experimentation has been ongoing for more than a century.

Compared to the metal material, glass makes a good optical substrate due to its low softening point, low hardness and its absence of a grain structure. This allows it to be formed, ground and polished into complex shapes with a precise figure and very smooth surface finish.

From the mid-20th century, glass and ceramics were the materials of choice for telescope mirrors. The main constituents of this category include borosilicate (also known as Pyrex or BK7 glass), fused silica and ultra low-expansion fused silica (ULE), Zerodur ceramic glass and silicon carbide.

1.6.2 Advanced mirror blank materials

Traditional glasses such as borosilicate have a relatively high Coefficient of Thermal Expansion (CTE), about $3x10^{-6}$/°C, which make them less attractive materials for making a large mirror blank, as thermal gradients spread through the volume very slowly. Another issue is that the intrinsic inhomogeneity of the material can cause large thick substrates and a high number of cracks, fissures or bubbles (Dierickx, 2000). This makes polishing and grinding difficult. To overcome these problems, advanced materials have been developed.

1.6.2.1 Ultra low-expansion ceramics

The primary mirror segments material for the large telescopes require extremely low thermal expansion to minimise distortions from thermal changes. Four categories of ultra low-expansion ceramics are briefly reviewed in this section: Zerodur®, ULE®, Sitall® and Clearceram®, and compared in **Table 1.1**.

1. Zerodur® (Schott)

The near zero-expansion glass ceramic Zerodur® was developed at Schott in Germany in the late 1960s. It is a well-established material for astronomical mirrors. Due to continuous improvements, it has been the preferred mirror blank material for most of the existing large segmented telescopes (Keck I, Keck II, HET). The success of this material is based on a set of outstanding properties (Dohring et al., 2004 and 2006):

1. The very low (less than ±0.05 x 10^{-6}/°C) linear CTE (Coefficient of Thermal Expansion), **Figure 1.12** illustrates the typical CTE over the entire temperature range. It can be seen that Zerodur® shows a near zero CTE in the room temperature range

2. The excellent polish ability allows a roughness of less than 1nm without special coatings

3. The outstanding reproducibility of the material's properties and quality is a very important requirement for the production of E-ELT's segments, because these segments (nearly 1000 segments in E-ELT) will be produced over several years with consistent high quality

Figure 1.12 Plot of the coefficient of thermal expansion of Zerodur® (Glaswerke, 2006)

For the casting of Zerodur® mirror blanks with diameters of 1 m, 2 m or 4 m, usually circular moulds are used. This leads to an excellent quality of circular mirror blanks. Hexagonal mirror blanks for most of the present 10 m class telescopes were also cut from those circular discs. The main disadvantage of this procedure is that much more material is needed. Therefore, a direct casting of hexagonal shaped castings was developed to reduce the amount of raw material used during the GTC projects. The advantages are less casting time, better stress distribution and significant material savings (Dohring et al., 2006; Hartmann et al., 2006).

2. ULE® (Corning)

Ultra-Low Expansion (ULE®) glass is a near-zero thermal expansion material, developed by Corning Incorporated (USA). It is unique from other low expansion materials in that it is fabricated by a flame hydrolysis process instead of being poured. The advantage of this process is the minimisation of impurities. ULE® is a titanium silicate glass, not a glass-ceramic (Sabia et al., 2006). Corning Incorporated has been making ULE® glass for astronomical applications since the 1960's. ULE® has been successfully employed for numerous monolithic and lightweight mirror telescopes, including the 2.4m Hubble Space Telescope and the Subaru Telescopes (Japan's 8.2m optical telescope, located at Mauna Kea, Hawaii).

3. Sitall® (LZOS)

Sitall® (or Astrositall®) was developed by the Russian company LZOS. It is a crystalline glass ceramic material with ultra low CTE (about $0.15 \times 10^{-6}/°C$ in the temperature range -60°C to +60°C) (Abdulkadyrov et al., 2004). The Southern African Large Telescope (SALT) has selected Sitall optical glass-ceramic for the manufacturing of its 91 primary mirror segments (Ponin et al., 2003).

4. Clearceram® (Ohara)

Clearceram® is another glass ceramic with an ultra low thermal expansion coefficient (for the regular Clearceram®, it is about $0.1 \times 10^{-6}/°C$ at room temperature). It was developed by the Ohara Company in Japan. Ohara has manufactured Clearceram® for many years. This material is used in the industrial ultra-precision instruments such as photolithography equipment (OHARA, 2012). Recently, Ohara established a manufacturing process and capability for large diameter blanks (about 2m diameter) (Kishi et al., 2010).

1.6.2.2 SiC

SiC (Silicon carbide) is a family of materials used for reflective mirrors. The basic material is composed of a tetrahedron of carbon and silicon atoms with strong bonds in the crystal lattice. SiC is not attacked by any acids, alkalis or salt up to $800^{o}C$. The high thermal conductivity, low thermal expansion and high strength give SiC exceptional thermal qualities. The specific numbers can be found in **Table 1.1** in the following section. SiC technology is being increasingly adopted for future space observatories, such as Herschel, whose secondary mirror was made from SiC (Spano et al., 2006).

However, to date, SiC optical components have not been produced in sizes exceeding 1.5m, and their performance beyond this figure remains to be proven. Several attempts were made to produce Gemini M2 blanks adopting SiC, but all cracked during cool-down. As a result, Zerodur® was adopted as a back-up solution (Bougoin et al., 2004). The polishing pressure required for SiC mirrors was up to four times greater than for a glass ceramic. In addition, SiC mirrors are known for their high cost and SiC manufacturing facilities are extremely specialized and technically demanding (Bougoin et al., 2004). In 2006, UCL aborted two 1m SiC blanks from different vendors, but both failed in manufacture (Walker, 2012A).

1.6.2.3 Vaporised Beryllium (Be)

Beryllium (atomic number: 4) is a promising material for mirror substrates and like aluminium substrates, it is normally nickel coated before polishing. Its surface is highly resistant to oxidization in air and its Young's modulus is high, therefore the mirror becomes stiff. Beryllium also has a relatively low coefficient of thermal expansion. Beryllium has been used in the cryogenic space telescope as the primary mirror for the past 30 years, as on program IRAS (Infrared Space Astronomical Telescope) (Parsonage, 2004). In a ground astronomical telescope, the four secondary mirrors for the VLT (Very Large Telescope) were made from Beryllium (Cayrel et al., 1996). A new grade of Beryllium was chosen for the primary mirror on the 6.5m JWST (James Webb Space Telescope) (Parsonage, 2004).

One important disadvantage is its extreme toxicity, causing diseases of the skin and lungs (Matson et al., 2004). Stringent safety precautions have to be applied when working with this material, thus increasing the cost of manufacture.

1.6.3 Comparison of mirror materials

Evaluating materials and processes for the fabrication of a large optical mirror is a rather complex task, which depends on budget, schedules and acceptable risks. The essential characteristics of material selection for large segment mirrors are (Bougoin et al., 2004):

1. Specific stiffness and thermal stability

2. Cost effective manufacturing and a reasonable time span

In order to reach a low mass and a high stiffness, a material with a small ratio of density and Young's modulus is required. Furthermore, the ratio of the coefficient of thermal expansion

and thermal conductivity should be low as well. A graphic example is shown in **Figure 1.13**, which compares some mirror materials for their thermo-mechanical figures of merit. From this graphic, it can be seen that some potential materials for ELT are on the left-bottom.

Beside their thermo-mechanical quality, those of cost and production difficulties are also important for large astronomical telescopes. There is an overview of possible materials, which are suited for the optical mirror in **Table 1.1**.

Figure 1.13 Thermo-mechanical figures of merit for a variety of mirror materials (ρ/E specific stiffness, where E is the Young's modulus and r the density and CTE/k, steady state thermal distortion coefficients, where CTE is the Coefficient of Thermal Expansion and k the thermal conductivity) (Dierickx, 2000)

Table 1.1 Materials comparison for candidate lightweight mirrors (Abdulkadyrov et al., 2004; Frank et al., 2005; Sabia et al., 2006; Kishi et al., 2010)

	Desired Value	Al	Be	SiC® (CVD)	Zerodur®	ULE®	Sitall®	Clearceram®
Density [kg/m3]	Low	2,700	1850	3,210	2,530	2,210	2,460	2,550
Young's modulus [GPa]	High	68	287	465	91	67	92	90
Coefficient of Thermal Expansion [1×10^{-6}/°C]	Low	22.5	11.3	2.4	0.05	0.03	0.15	0.1
Thermal Conductivity [W/m x °C]	High	167	216	198	1.64	1.31	1.18	1.51
Ability to be Diamond turned	High	High	High	Low	Low	Low	low	low
Difficulty of Superpolishing	Low	Medium	High	High	Low	Low	Low	low
Cost of finished Mirror	Low	£	£££	£££	££	££	££	££

1.7 Active optics and Adaptive optics in ELTs

Although the technology about active and adaptive optics is beyond the research work of this thesis, it is necessary to review their fundamentals. An ELT to deliver its science case would be impossible without active/adaptive optics (Love and Saxena, 1994). The E-ELT segments will have a warping harness which enable low order aberrations to be 'tuned out' and this has been taken into account in ESO's specification (ESO, 2011).

Active optics generally refers to the figure control of optical elements at low bandwidth (less than one Hertz) to correct residual aberrations and gravity and thermal effects. Adaptive optics refers to the correction of high frequency (above a few Hertz) wavefront disturbances by atmospheric turbulence (Bely, 2003; Kendrew, 2006). The basic principle of both techniques is introduced in the following paragraphs:

1. Active optics

The primary mirrors of the next generation of large ground-based optical telescopes are highly segmented which will involve thousands of degrees of freedom in the primary mirror. An active supporting system is crucial to ensure good positioning and orientation of the segments with respect to their parent shape, because of the inevitable distortions of the steel structure that support the segments. To reduce the total mass of ELTs, primary mirror segments will be made very thin cf. classical telescopes (for ELT's segments, 1.4m cross-corners, are only 50mm thick). It would be impractical to keep them rigidly in the correct relative positions. Therefore, active optics are required to maintain the figure of the overall primary mirror during operation of the telescope.

Figure 1.14 is a schematic of an active optics system (Wilson et al., 1987A). Starlight from the telescope is simultaneously sent to the focus and to a wavefront sensor by a beam splitter. The computer analyses the output of the wavefront sensor and sends control signals to the primary mirror to correct any errors from the optical elements of the telescopes, such as rigid body movements of the mirrors and deformation of the mirrors, by adjusting the support forces.

Figure 1.14 Active optics fundamental principles (Wilson et al.*,* 1987A)

2. Adaptive optics

The performance of high-resolution imaging with ELTs is severely limited by atmospheric turbulence. Adaptive optics is a technique that allows ground-based telescopes to remove the blurring effects caused by the Earth's atmosphere.

Adaptive optics was first proposed by astronomer Babcock (1953) for improving the performance of ground-based telescopes in 1953. Adaptive optics offer real time compensation (a few milliseconds time constant) of the atmospheric turbulence. The simplified principle of adaptive optics is shown in **Figure 1.15**. If there was no atmospheric turbulence, the wavefront of the light from stars would be plane. However, over large fields of view, atmospheric effects are considerable for the ELTs. The adaptive optics system uses a

guide star (either natural guide stars or artificial laser guide stars) as a calibration source and then deforms a small mirror (adaptive mirror) to correct for distortions caused by the atmosphere (Love et al., 2004).

Figure 1.15 Simplified diagram of an adaptive optics system (Tokunaga and Jedickle, 2006)

1.8 European Extremely Large Telescope (E-ELT)

The European Extremely Large Telescope is a proposed ground-based facility featuring an optical/near-infrared telescope operation. It is being designed by the European Southern Observatory (ESO). The E-ELT completed its detailed-design phase at the end of 2011 and final approval for its construction is planned for 2012. The artistic illustration of E-ELT is shown in **Figure 1.16**.

The primary mirror of the E-ELT was originally proposed as 42m in diameter, 84m radius, with 984 aspheric segments, as shown in **Figure 1.17**. In the summer 2011, ESO Council endorsed a revised design for E-ELT with the purpose of a trade-off of the budget and risk. The new design slightly reduces the diameter of the primary mirror to 39.3m, 69m radius, which will be composed of 798 hexagonal segments, each 1.44 meters across corners. The details of the 39.3-metre primary mirror are introduced in the following section.

Figure 1.16 Artist's rendition of the E-ELT (ESO, 2011)

Figure 1.17 E-ELT's original primary mirror pattern with 984 hexagonal segments (Preumont et al., 2009)

The E-ELT is a five-mirror telescope design that includes a three-mirror anastigmat optical solution (M1, M2 and M3), one 2.5m adaptive optics mirror (M4) and one 2.5m tip-tilt mirror (M5). Adaptive optics are fully integrated in the telescope design (M4) for fast correction of the ground layer atmospheric turbulence (Ramsay et al.*,* 2010). The five mirror design is shown in **Figure 1.18**.

Figure 1.18 Five mirrors design of E-ELT (ESO, 2011)

1.9 E-ELT segments and specification

1.9.1 E-ELT segments

The revised E-ELT primary mirror is a 39.3m diameter elliptical concave mirror with a conic surface expression as following:

$$z = \frac{c \cdot \rho^2}{1 + \sqrt{1 - (k+1) \cdot c^2 \cdot \rho^2}}$$

where:

c is the curvature of the vertex, $c=1/R=1/69000$mm^{-1};

k is the nominal conic constant ($k=e^2$, where e is the eccentricity), $k=-0.995882$;

ρ is the distance between point (x, y, z) and original point ($0, 0, 0$) in the XOY system ($\rho^2=x^2+y^2$).

The E-ELT primary mirror is made of off-axis aspheric segments, which have a quasi-hexagonal contour. The segments are about 1.44 m across corners (maximum dimension) and 50 mm thick. The total manufacturing requirement is 931 segments, only 798 of which are installed in the telescope. In view of the 6-fold symmetry of the assembled mirror (shown in **Figure 1.19**, left), there are 133 (798/6) families of identical segments, allowing one spare for each family of segments. Having 7 identical segments per family allows for a realistic operation scheme in relation to coating, as a cluster of segment taken out of the telescope for recoating (segments need to be re-coated periodically) can immediately be replaced by another cluster (of the same family), which has been prepared beforehand (ESO, 2011).

Figure 1.19 Layout of E-ELT primary mirror (on the left) and location of 7 prototype segments (on the right) (ESO, 2011)

The specifications of these segments' surface are highly challenging and the manufacture of 931 such segments in a few years demands a new process that requires deterministic, automation of fabrication, metrology and handling, minimization of manual interventions and streamlining of data-flow for measurement analysis and process-control. European Southern Observation (ESO) awarded OpTIC, St. Asaph UK, a contract for the production of seven prototype segments for the E-ELT project. At the time, OpTIC was owned and operated by the Wales Assembly Government as part of the Technium network. OpTIC was subsequently acquired by Glyndwr University and took its current name 'OpTIC Glyndwr'. These prototype segments are located on the peripheral region of the primary mirror (as shown in **Figure 1.19**, right) and production of these seven segments will be the most difficult in the E-ELT primary mirror system as they are highly off-axis. The manufacturing of each of them is highly challenging. The details of the specifications are introduced in the following section.

1.9.2 Specifications of the segments

As mentioned previously, the design of primary mirror for the E-ELT was changed from 42 metres to 39.3 metres in diameter. However, the prototype segments still correspond to the original design of 42 metres.

1 The form specification of useful area

The 'useful area' is defined as the bulk surface excluding the 10mm wide peripheral zone. The data need to be measured by interferometry. The maximum allowable surface errors (RMS) over the useful area of any single prototype segments are:

(a) 50nm (RMS) for the overall surface error, which covers all term including curvature deviation

(b) 30nm (RMS) for the residual surface error, which allow the terms of Tip/Tilt, Defocus and Astigmatism to be removed

2 The edge specification

From interferometry data, the 'edge zone' is defined as 10mm wide peripherals of the useful area of the segment. A 0.5mm wide band around the periphery of the segments is allowed to be removed for the final bevelling. The 10mm wide hexagonal ring is divided into six individual trapezoidal edge-segments, each of which is analysed separately to provide the PV of the edge mis-figure values, as shown in **Figure 1.20**. The edge specifications are:

(a) The maximum edge mis-figure (PV) of six edges shall be less than 200nm surface error

(b) The average edge mis-figure(PV) of six edges shall be less than 100nm surface error
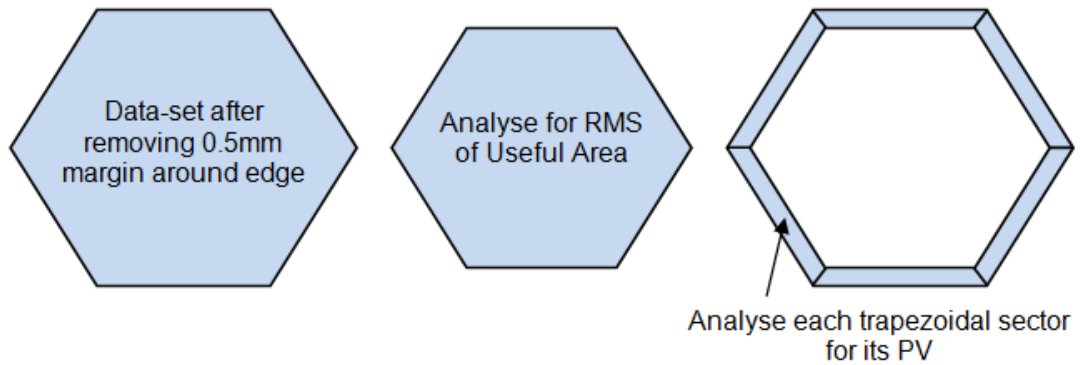
Figure 1.20 Analysis of interferometry data for edge mis-figure (Walker, 2012B)

The ESO specification is ambiguous regarding the datum with respect to which edge mis-figure is measured, also the method of measurement (interferometry or profilometry etc). D.D. Walker proposed to ESO a refined measurement protocol, that ESO accepted, in which the 95% PVq (rather than 99% PVq adopted previously) represented a significant but reasonable concession on the segment of ESO (Walker, 2012B).

3 The Roughness

The roughness of the polished surface of any prototype segment shall not exceed 3nm. The definition of the metric with respect to how roughness is measured was not specified by ESO. In this thesis, the measurement region of 1.4mm x 1mm with 1000 pixels is adopted, with any tip/tilt & defocus term remained in analysis.

The specification of the E-ELT segments is summarised in the **Table 1.2.**

Table 1.2 Specification of the E-ELT segments (ESO, 2011)

	Specifications
The useful area (excluding the 10mm wide peripheral zone)	Overall surface error: <50nm (RMS)
	Residuals surface error after removal of low- and mid-spatial frequency terms: <15nm (RMS)
The edges (the 10mm wide peripherals of the useful area of the segment)	The maximum edge mis-figure (PV) of six edges shall be less than 200nm surface error
	The average edge mis-figure (PV) of six edges shall be less than 100nm surface error
The roughness	The roughness of the polished surface shall not exceed 3nm in the surface area

1.10 The techniques for fabrication of the large aspheric part

Three fundamental techniques for fabrication of large aspheric part are listed in **Table 1.3**. The details of these aspheric fabrication approaches are introduced in **Chapter 2**.

Table 1.3 Three fundamental techniques for fabrication of large aspheric part

	Polish techniques	Limited range
1	Stressed mirror polishing	Only circular parts, and residual distortion after cutting hexagonal requiring rectification
2	Large stressed-lap polishing	Only circular parts can be processed
3	Small sub-aperture polishing	From general shape up to extreme aspheric shape; Challenge of edge mis-figure

Chapter 2

Review of aspheric surface polishing and figuring techniques

This chapter is based around a discussion of optical aberrations, and then polishing and figuring techniques for fabrication of the large aspheric part are reviewed. A brief comparison of these techniques is given at the end of this chapter.

2.1 Introduction

In general, spherical optics produce wavefront aberrations which blur the image, and may be offset by other optics, at the expense of added weight and size. A high quality optical system often consists of several groups of lenses with spherical surfaces. This adds weight, and precision mechanics that are required to mount and align these surfaces, increase the cost considerably.

More and more, aspheric surfaces are used in optical systems. Aspheric surfaces provide the designer with additional degrees of freedom in ray-tracing optimization, compared with an all-spherical solution. In general, this allows independent correction or balancing of various aberrations (Schulz, 1987). Finally, it achieves some or all of the following: fewer elements, more compact packaging, and lower mass and superior imaging performance.

However, manufacturing difficulties and the cost of producing aspheric surfaces is substantially

higher than that of spherical surfaces optical elements (Yuan and Wang, 1999; Pollicove et al.*,* 2000). Producing an aspheric surface poses several challenges using traditional polishing methods. For example, the part radius of curvature varies across the surface, and so a rigid tool can make intimate contact in only one zone. Imperfect contact introduces low and high pressure spots, leading to zonal errors. This tends to force the craft optician to use a range of small tools with consequent reductions in volumetric removal rates and increases in manufacturing time.

The breakthrough in modern optical processing compared to traditional technique was the advent of computer controlling 'small tool' polishing. The processing technology is often referred to as computer controlled polishing (CCP). Its technical ideas were first proposed by Rupp and Jones of the American Company Itek in the 1970s (Jones, 1977). The computer-controlled small polishing tool technique was based on the Preston hypothesis (the details are discussed in **Section 2.3**), and modelling of the polishing process (Jones, 1978). Thus, this method is also known as the certainty polishing technique (Jones and Rupp, 1991).

A more modern word is 'deterministic' which basically means the result conforms to the computer model. In the processing of large-scale optical components, particularly these that are non-spherical, these computer controlled polishing technologies are increasingly being applied. These polishing technologies are usually aimed at, at least some of, three characteristics: low tooling cost, deterministic material removal, and embedded process control intelligence (Jacobs, 2004; Kim et al.*,* 2005).

Currently, the developing deterministic polishing or figuring technology includes a variety of technologies, such as dynamic stressed lap polishing technology, magnetorheological finishing (MRF), fluid-jet finishing (FJ), ion beam figuring (IBF), reactive atomic plasma technology (RAPT) and the '*Precessions*' process. These techniques have been developed over the last few

decades for the fabrication of aspheric optical surfacing (Pollicove et al.*,* 2000; Burge et al.*,* 2009). An overview of these techniques is introduced in a later section.

2.2 Optical aberrations and Zernike polynomials

Before considering the manufacturing technologies any further, it is useful to introduce the problem that these technologies aim to solve. This is considered below at the most fundamental level – the image defects that arise in optical systems.

A perfect optical system would focus the light of a distant point source into a diffraction-limited image on the focal surface, to establish a point-to-point correspondence between an object and its image. Any deviation of the wavefront away from the spherical causes a deterioration in the quality of the point images as shown in **Figure 2.1**. It can be seen that rays emerging from a spherical wavefront converge towards a single point in the image plane (on the top), and rays emerging from an aberrated wavefront form an extended area, spreading the light energy (on the bottom) (Bastaits, 2010).

Figure 2.1 Diagram of wave aberration and image (Bastaits, 2010)

In general, it is convenient to express wavefront data in a compact polynomial form to help in the interpretation of optical test results. Zernike circle polynomials (because of their orthogonality over a circular pupil) are often used for this purpose as they are made up of terms, which are the same form as the types of aberrations often observed in optical tests (Zernike, 1934). Zernike circle polynomials are formed as:

$$W(\rho, \theta) = \sum_{i=1}^{n} a_i Z_i(\rho, \theta)$$

where $W(\rho, \theta)$ and $Z_i(\rho, \theta)$ are respectively the wavefront and the ith Zernike polynomial expressed in polar coordinates, a_i is the coefficient of the polynomial $Z_i(\rho, \theta)$. In this polynomial, a series of radial orders can be demonstrated as different wavefront error maps. **Table 2.1** contains a list of Zernike polynomials up to 4th order and their meanings relative to the optical aberrations. The description of optical aberrations by Zernike polynomials is depicted in **Figure 2.2**.

However, Zernike circle polynomials are not appropriate for noncircular pupils, such as annular, hexagonal, elliptical and square pupils, due to their lack of orthogonality over such pupils. Various approaches for calculating the Zernike coefficients for noncircular pupils were carried out, including when such a pupil is treated as being circular (Hou et al., 2006, Dai et al., 2008 and Lee, 2010).   It is a common practice to draw a unit circle around the interferogram, define a centre, and use the circle polynomials to determine the content of the aberration function represented in the interferogram (Dai and Mahajan, 2008).

Table 2.1 Zernike Polynomials (up to 4th order) (Zhu et al., 1999)

order	$Z_i(\rho, \theta)$	Meaning
0	1	Piston
1	$2\rho\sin(\theta)$	Tilt in *y* direction
1	$2\rho\cos(\theta)$	Tilt in *x* direction
2	$\sqrt{6}\rho^2\sin(2\theta)$	Astigmatism with axis at 45^0
2	$\sqrt{3}(2\rho^2 - 1)$	Defocus
2	$\sqrt{6}\rho^2\cos(2\theta)$	Astigmatism with axis at 0^0
3	$\sqrt{8}\rho^3\sin(3\theta)$	Trefoil
3	$\sqrt{8}(3\rho^3 - 2\rho)\sin(\theta)$	Coma along *y* axis
3	$\sqrt{8}(3\rho^3 - 2\rho)\cos(\theta)$	Coma along *x* axis
3	$\sqrt{8}\rho^3\cos(3\theta)$	Trefoil
4	$\sqrt{10}\rho^4\sin(4\theta)$	Trefoil
4	$\sqrt{10}(4\rho^4 - 3\rho^2)\sin(2\theta)$	Secondary Astigmatism
4	$\sqrt{5}(6\rho^4 - 6\rho^2 + 1)$	Spherical Aberration, Defocus
4	$\sqrt{10}(4\rho^4 - 3\rho^2)\cos(2\theta)$	Secondary Astigmatism
4	$\sqrt{10}\rho^4\cos(4\theta)$	Trefoil

Figure 2.2 Zernike Polynomials (up to 4th order) (Bastaits, 2010)

In general, most of the wavefront errors due to misfiguring, thermal distortions and misalignment, can be described by combining the first 20 polynomials. However, they are limited in their ability to describe those errors at mid-spatial and very high spatial frequencies, such as surface roughness of mirrors and point defects, which would require high order terms.

The precision of manufacturing optical surfaces is limited by the accuracy of the metrology, because the error in a test will be inputted into the surface on the next run. The real attribute of the low order aberrations in the optical test is analysed in **Table 2.2**:

Table 2.2 The real attribute of the low order aberrations in the test (Walker, 2012A)

Aberrations	The real attribute
Tip/tilt	The misalignment in the test, normally removed in data analysis
Defocus	The error in base radius of the asphere, or a Z-distance error in an interferometry test
Astigmatism	The principle bending modes of a plate-as may occur on a defective support system
Coma	The decentration of part in a test
Trefoil	The print through of a 3 point support

2.3 Preston equation

The theoretical basis for estimation of removal rates in polishing was provided by Preston (1927) in 1927, and underpins most CCP techniques. This simple model is commonly used to describe the optical surface for processing, as follows:

$$\Delta h(x,y) = k \cdot v(x,y) \cdot p(x,y)$$

where:

$\Delta h(x, \text{y})$ - Removal in unit time at point (x, y)

K - Preston coefficient, related to the part-material, polishing-tool, polishing liquid and temperature of work area

$v(x, y)$ - Instantaneous relative speed of the polishing tool at point (x, y)

$p(x, y)$ - Instantaneous pressure exerted by the polishing tool at point (x, y)

Preston simplified the complex mechanism of material removal during polishing: the local material removal rate is determined by tool pressure and relative speed. Many Computer Controlled Polishing technologies (CCP) are based on the Preston equation to optimize the dwell time map.

2.4 Traditional polishing approach (Craft)

The traditional polishing technique has been used for figuring the optical surfaces for centuries, and is mainly used for the generation of flat and spherical optical surfaces. A polishing tool has the inverse form of the part. The intimate contact between the polishing tool and the workpiece, working with the abrasive slurry, slowly enhances the surface finish. The material removal takes place by chemo-mechanical modes.

A pitch layer is one of the most historic surfaces for a polishing tool and Wilson (2004), referred to the fact that Isaac Newton might have been the first optician to use a pitch lap for polishing on an optical surface in 1668. Pitch is a viscoelastic material with complex material properties, such as a low softening point (55-70°C) (OSA, 2011). Compared to glass, pitch is very soft; therefore, it takes the shape of the part during polishing and remains in close contact without scratching.

Polishing pressure and dwell time are controlled by a repetitive stroke made by hand; therefore, the accuracy and efficiency of the process very much depends on the experience of the optician (as shown in **figure 2.3**).

The process is based on feedback from a test, and the fabricator works on the part for a while and checks the surface. Reacting to the results, the experienced fabricator controls various parameters to improve the errors on the surface in an interactive procedure. Clearly, higher quality surfaces require more time to polish. Flats and spheres can be produced by the conventional method down to 10nm RMS or better, depending on the size and surface shape. Aspheric surfaces can be made by the traditional method with a few adjustments; however, they are considerably more difficult to polish.

Figure 2.3 Craft polishing process (picture by the author, 2011)

2.5 The techniques of polishing aspheric part

As already mentioned in **Section 1.10**, there are three fundamental techniques of fabrication for aspheric parts, which are stressed mirror, stressed lap and small tool polishing. This section gives a brief review of these techniques.

2.5.1 Stressed mirror

The stressed mirror polishing technique was developed by Lubliner and Nelson in 1980 (Lubliner and Nelson*,* 1980). The principle of this method is based on the theory of elasticity; the mirror blank is stressed to a different shape - the inverse of the asphere required. Thus, a mirror could be polished into a sphere, then when the forces are released, the mirror relaxes back into the desired asphere.

Figure 2.4 Stressed mirror polishing on Keck's segment (Mast and Nelson, 1990)

This method was successfully used to polish the 1.8m, across corners, hexagonal segment mirrors of the Keck's primary mirror. The diagram of the stressed mirror polishing is shown in **Figure 2.4**. Forces and moments are applied under and at the edge of the part by a set of 24

levers. The spherical shape was polished by a traditional pitch lap. Finally, the forces and moments were released and the mirror elastically deformed to the desired hyperboloid (Mast and Nelson, 1990). Keck's segments were polished from circular blanks, then after polishing had been completed, they were cut into a hexagon shape using a diamond saw.

Stressed mirror polishing allows an aspheric part to be polished as a spherical part. However, the high order error is difficult to bend. Thus, this method provides a low process precision. It has been reported that the surface form error of 225nm RMS was achieved after stressed mirror polishing of Keck's segment (Mast and Nelson, 1990). This residual error was addressed using ion beam figuring. This is introduced in **Section 2.5.3.3**.

2.5.2 Stressed lap

The stressed mirror polishing technique stresses the mirror to the inverse asphere, and it can be polished with standard spherical tooling. The stressed lap is the exact opposite approach – the tool is deformed.

The Stressed lap polishing technique was demonstrated by the Steward Observatory Mirror Laboratory, University of Arizona in the early 90s (Anderson et al., 1991). In the beginning, the research effort led to the development of a new deformable large-tool polishing technique, ultimately to polish 8m glass mirrors with highly aspheric figures. For example, a rigid passive lap cannot maintain an accurate fit to a paraboloidal surface because of the variations in curvature across the surface. In principle though, a large stiff tool is advantageous because it produces high glass-removal rates and natural smoothing over a wide range of spatial frequencies. The stressed lap permits the use of a large stiff tool on highly aspheric surfaces, because the tool's surface form is actively changed as it is moved over the surface. The form

changes are induced in a large circular plate through the application of bending and twisting edge moments.

The stressed lap consists of a metal disk with actuators attached to the upper face and coated on the lower face with the traditional squares of pitch (Martin, 1990). It is pressed against the mirror prior to polishing. When the polishing run starts, the actuators must induce the correct changes in form as the lap moves relative to the mirror. Stressed lap polishing technique has been adopted as the core technique for the Giant Magellan Telescope (GMT) segments. The GMT's segments have 15 mm peak-to-valley aspheric departure (Martin et al., 2004). As shown in **Figure 2.5,** under the effect of 12 variable torques generated by the installed drives around the lap, the stressed lap can be deformed according to the requirements of the polishing process. The actuators are programmed to make the lap shape match the ideal aspherical surface. In large optical component processing, actively stressed lap polishing has some advantages, such as high processing efficiency and natural smoothness.

Figure 2.5 A 1.2m 'stressed lap' tool is used to polish an 8.4m diameter segment for GMT (Martin et al., 2004)

The Steward Observatory Mirror Laboratory has been improving this technique since 1990 and has completed two 8.4 metre diameter primary mirrors for the Large Binocular Telescope. The mirrors were figured to an accuracy of 15 nm RMS surface after subtraction of low-order aberrations (Martin et al., 2006). However, there are some difficulties in processing large aspheric surfaces using stressed laps. The stressed lap is very complex and needs to be highly maintained especially for deep off-axis aspheric surfaces. The tool has to be re-built for each new process (Chen et al., 2010). There are no published reports available on processing non-circular (for example, hexagon) parts using stressed-lap techniques.

2.5.3 Small tool polishing and figuring techniques

Rather than deforming the part or the tool, the aspheric misfit problem can be addressed by reducing the tool's contact area, and introducing some mechanism for passive compliance over the area of contact, such as: Magneto-rheological finishing (MRF), Fluid-Jet (FJ), Ion Beam Figuring (IBF), Reactive Atomic Plasma Technology (RAPT) and '*Precessions*' polishing.

2.5.3.1 Magneto-rheological finishing (MRF)

The MRF approach for processing optics was invented at the Luikov Institute of Heat and Mass Transfer in Minsk, Belarus in the late 1980s by a team led by William (Prokhorov et al., 1992; Jacobs et al., 1998). It is a deterministic method for producing complex optics. This process was developed at the Center for Optics Manufacturing (COM) by a group of international collaborators (Jacobs et al., 1995) and commercialized by QED Technologies Inc. (Golini et al., 1999 and 2001). It is mainly used in the field of high quality optical production for nonmagnetic materials.

MRF's schematic setup is shown in **Figure 2.6**. MRF is based on a magneto-rheological fluid with nonmagnetic abrasive particles. The polishing fluid includes magnetic particle (typically carbonyl iron), and may be stiffened in a controlled manner by an applied magnetic field. The stiffened fluid constitutes the polishing 'tool' that removes material from the sample (Harris, 2011). On optical glasses a typical removal rate of 10μm/min is observed and surface roughness can be achieved up to 1 nm rms. Form errors can be reduced from a few λ to $\lambda/5$ PV (Tricard et al*.,* 2006; Schinhael et al*.,* 2006).

The safety issue (slurry has to contain magnetic sensitive particles) and high cost of Magneto-rheological fluid are the MRF's disadvantages (Demarco, 2005). It is also a finishing process and is not used directly to polish a ground part.

Figure 2.6 Schematic view of the MRF setup (Harris, 2011)

2.5.3.2 Fluid-Jet (FJ)

Fluid-jet was first developed at Delft University of Technology in 1998. Fähnle's research (1998A, 1998B, 1999) showed that it is feasible to utilize Fluid-jet for precision polishing. With Fluid-jet, they polished one flat BK7 optical glass with surface roughness of the surface (RMS) which decreased from 475nm to 5nm.

The Fluid-jet system uses a nozzle to guide premixed slurry as a jet to the workpiece at high speed. Material is removed by collision and shearing actions between an abrasive and the workpiece. An overview of the Fluid-jet setup is shown in **Figure 2.7**. Therefore, this method is also called Abrasive Jet Polishing (AJP). It is a novel deterministic precision optical manufacturing technique.

Figure 2.7 Overview of the Fluid-jet schematic setup (Brug et al.*,* 2002)

Compared with classic polishing methods, Fluid-jet's advantages are: the precision of the surface shape can be controlled easily and the tool is cooled. In addition, Fluid-jet is suitable for polishing various complex surfaces with no edge effects, because the tool is a liquid column (Gonzalez et al., 2004 and Salinas et al., 2006).

However, Fluid-jet is still in the early stage and has shortcomings such as low removal rate and difficulty in controlling the stability of influence function. Thus, Fluid-jet is usually used at the stage of final surface finishing. Another application of Fluid-jet is to remove diamond turning marks on diamond turned mirrors (Li et al., 2010).

The magneto-rheological fluid jet (MR-Jet) has been developed by QED Technologies Inc, which has a long standoff distance (tens of centimetres). This enables the polishing of steep concave surfaces (principally the inside of missile cones) that are impossible to reach with a MRF wheel-based tool (Kordonski et al., 2003).

Zeeko Ltd. has developed Fluid-jet on their hybrid machines, which accommodate both the fluid-jet and bonnet processes (Walker et al., 2006B). The jet direction is precessed to give a Gaussian-shaped influence function. It has potential for edge-correction; this is introduced in **Section 3.3**.

2.5.3.3 Ion Beam Figuring (IBF)

IBF is a deterministic and non-contacting optics processing technique. Error-correction by ion beams uses a focused broad ion beam, which is raster-scanned across the surface of the part, according to the dwell time map, to remove the surface error (typically, surface error of 5nm RMS can be achieved) as shown in **Figure 2.8**.

Figure 2.8 Error correction processing scheme of IBF (Zeuner and Nestler, 2010)

IBF has been used for more than 30 years to figure high quality optics of various materials and dimensions. The early work on the IBF of optical components was performed by Gale (1978) in 1978. IBF was first demonstrated by Wilson et al. (1987B) at the University of New Mexico in 1987. The Kodak Company and Carl Zeiss Company have investigated its application in the mirror fabrication field of large telescope systems since 1987 (Drueding et al., 1995). The IBF process has been successfully used on the final processing of the primary mirror of Keck telescope at Kodak.

The extremely slow material removal is the main disadvantage of IBF. The segment has first to be polished to the final requirement before going to IBF. In the case of 'Keck', a 1.8m corner-corner hexagonal segment required 14 days to correct the residual error (RMS 0.762µm) after stressed mirror polishing (Mast and Nelson, 1990).

2.5.3.4 Reactive Atomic Plasma Technology (RAPT)

Reactive Atomic Plasma Technology is a new technology for the processing of mirrors, which has been developed by RAPT Inc (US) and was patented in 2002. UCL and Cranfield University are developing the reactive atomic plasma machine for the production of high power lasers, after previous work directed at mirror segments (Fanara et al., 2006A and 2006B).

The material removal is performed by a stream of reactive atoms, that is directed onto the surface of the glass and produces the volatile SiF_4 and CO_2 by reaction, both of which are exhausted gaseously. The schematic of RAPT processing is shown in **Figure 2.9**.

Figure 2.9 RAPT processing (Subrahmanyan and Gardopee, 2008)

RAPT is a non-contact, sub-aperture, deterministic material removal technology with a wider material removal rate capability. In 2008, Subrahmanyan and Gardopee (2008) reported that a 100 mm diameter fused silica part has been figured by RAPT from RMS 0.124λ to 0.015 λ in 24 minutes.

RAPT is an atmospheric pressure process, which precludes the need for expensive vacuum chambers for processing larger mirrors that makes RAPT potentially more cost-effective than ion beam figuring. Unfortunately, it does not work on Zerodur-type material. Even on ULE, it degrades surface texture, requiring post-polishing (Cranfield University, 2011).

2.5.3.5 Introduction to the *'Precessions'* polishing technique

The *'Precessions'* polishing technology was developed at UCL in the early 90s and commercialized by Zeeko Company in 2000 (Bingham et al.*,* 2000; Walker et al.*,* 2001A and 2001B). It is an advanced and rapidly expanding innovative technology to polish ultra precision surfaces for telescope mirrors and other optical surfaces (Walker et al.*,* 2005; 2006A; 2006B and 2011A).

The *'Precessions'* process is a deterministic, ultra-precision optics processing technique based on computer controlled polishing (CCP) technique. *'Precessions'* uses a spinning, bulged and compliant bonnet tool covered with a suitable standard polishing cloth (such as polyurethane), and working via an abrasive slurry.

2.6 Comparison and summary

Polishing an aspheric surface is very difficult because there is a mismatch between the polishing tool and the surface of the glass. In the special case of E-ELT mirror's segments, they must have a good figure right to their edges.

The techniques for polishing aspherics have been reviewed in this chapter. The comparison of these techniques is summarised in **Table 2.3**.

To fabricate almost 1000 segments in a few years with a challenging specifications; the process also requires deterministic, automation of fabrication and minimization of manual intervention. The *'Precessions'* technique with many advantages has been proposed for the fabrication of the prototype segments for E-ELT project. The details of the *'Precessions'* process will be discussed in **Chapter 3**.

Table 2.3 The comparison of the aspheric surface polishing and figuring techniques (Mast and Nelson, 1990; Kim, 2000; Martin et al., 2004; Harris, 2011)

Aspheric surface polishing techniques		Description	Advantages	Disadvantages
Stressed mirror polishing (Keck Observatory)		The mirror blank is stressed during polishing. When forces are released, the mirror relaxes to the desired form	The aspheric part could be polished as a spherical part	High order error is difficult to bend, which causes the low processing precision and needs subsequent final figuring process; Only circular part
Stressed-lap polishing (Steward Observatory Mirror Lab)		Tool is actively deformed to match the local asphere	Large tool provides high material removal rate	Complex tool has to be re-built for each new part; Only circular part can be processed
Small sub-aperture tool polishing or figuring	Magneto-rheological finishing (MRF)	Magneto-rheological fluid abrasive is stiffened by magnetic field	Tool conforms to local aspheric surface	Safety issue(slurry contains magnetic sensitive particle); High cost of Magneto-rheological fluid; Will not polish
	Ion Beam Figuring (IBF)	Bombardment with ion particle removes the material	Highly deterministic and no edge effect	Extremely low material removal rate
	Fluid Jet (FJ)	Kinetic energy of collisions between the abrasive and the part	It is suitable for polishing complex surface and no edge effect	Low material removal rate and difficulty in controlling the stability of influence function
	Reactive Atomic Plasma Technology (RAPT)	Stream of reactive atoms	Deterministic technique with no edge effect	Still at an early stage; It is not applicable for Zerodur and similar material; Degrades texture

Chapter 3

'*Precessions*' polishing

The research work reported in this thesis is based on the '*Precessions*' polishing method. This chapter presents this technique in detail and provides an overview of the machine, choice of polishing tools, '*Precessions*' process parameters, tool paths and metrology that are employed in this study.

3.1 The principle of the '*Precessions*' polishing

The basic principle is a section of a compliant spherical bonnet that is pressed against the surface to create a circular contact spot. The bonnet is rotated about its axis, and the rotation-axis precessed, to create a near-Gaussian removal influence function (Walker et al., 2003). The geometry of the bonnet is shown in **Figure 3.1**. The tool contact-area (spot) and polishing-pressure can be modulated independently by changing respectively the axial position of the tool and its internal pressure. The 'Z-offset' (bonnet compression) defines the delivered spot-size for a specific size of bonnet. Different ranges of spot-size can be provided by exchanging bonnets between runs, and radii of curvature of bonnet from 20mm to 320mm are available. This gives the capability to optimise the process automatically using a limited range of different spot-sizes across a surface, and manually using different tools for different stages of the work, or for the different demands of smaller and large work-pieces.
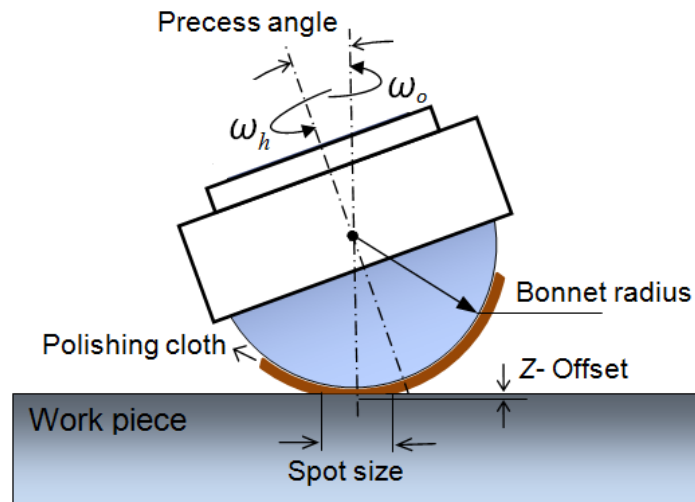
Figure 3.1 Detailed geometry of bonnet for '*Precessions*' polishing (drawn by the author)

In the '*Precessions*' polishing technique, a pre-polish process can be chosen for constant material removal ('onion skin' removal). This removes surface and the sub-surface features from prior grinding or *grolishing* (a hybrid technique between grinding and polishing) process, whilst preserving the surface form. Pre-polishing is conducted under the constant feed rate (Walker et al.*,* 2007).

Corrective polishing is performed by moderating the polishing tool's dwell-time at each location, according to the required removal needed to correct the measured local error. The resulting dwell-time map is interpreted by the machine as a varying traverse speed along a pre-determined tool-path. The tool-influence-function (TIF) is stable and the accuracy of convergence is typically 80% under well-controlled conditions, but can, under ideal conditions, reach 90%. These factors, combined with the ability to change continuously the polishing pressure and contact-area, render the method well-suited to both the texture control and form control of flats, spheres and aspherics and freeform surface.

'*Precessions*' has many advantages over the classical pole-down configuration of a spinning tool beside that of no mismatch when processing the aspheres (Walker et al.*,* 2003). First, the

surface is rubbed in different directions, giving rise to superior surface-texture with almost no directional properties, as shown in **figure 3.2**. Secondly, the tool influence function (TIF) integrated over 0°, 90°, 180°, 270° precess positions is near-Gaussian, symmetrical, and lacks the high spatial frequencies and centre-zero of removal. Thirdly, the novel polishing tool with 7-axis motion (see **Figure 3.5**) provides the capability to polish flat, sphere, asphere, even freeform surface and almost no glass material limit.
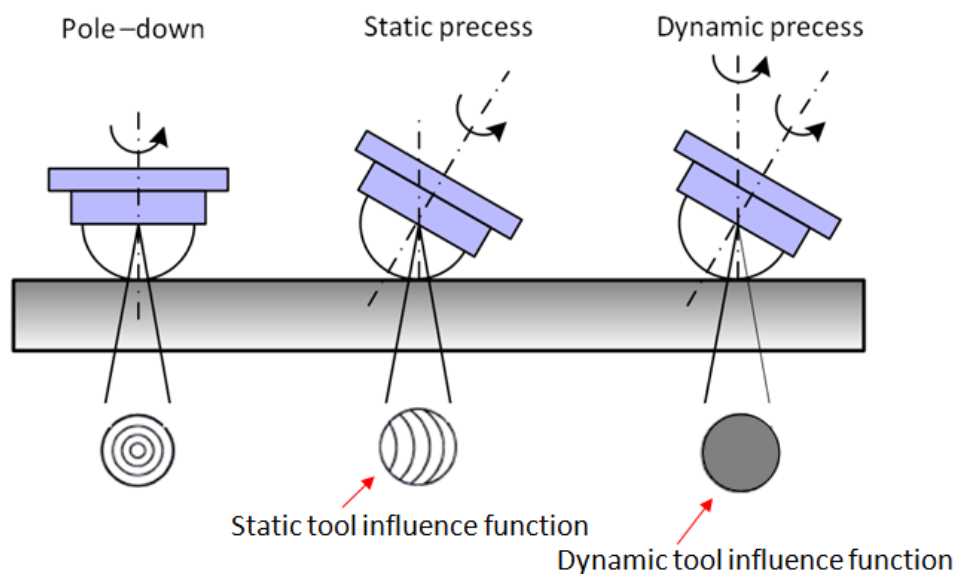
Figure 3.2 Trace comparisons of pole-down polishing and 'processions' polishing (drawn by the author)

The inflated bonnet tool moulds itself around the local curvature of an asphere, to maintain (to first order) a constant influence function as the tool traverses the surface. Traditional hard lap tools suffer from mismatch during processing an asphere that produces a high spatial frequency error on the surface. Due to the flexibility of the bonnet tool, there is no mismatch between the tool and the aspheric surface, as shown in **Figure 3.3**.
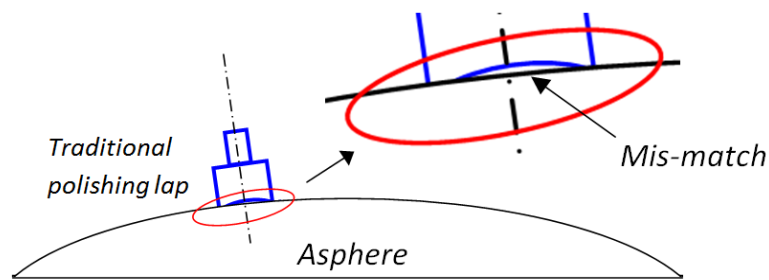
(a) Traditional polishing lap tool introduces mismatch on the aspheric surface
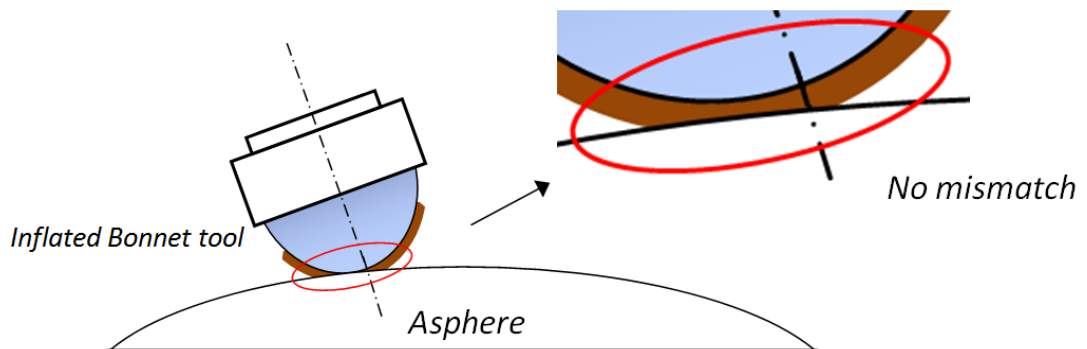
(b) Inflated bonnet tool performs an intimate contact with aspheric surface

Figure 3.3 Comparison of traditional lap and bonnet tool (drawn by the author)

3.2 Overview of polishing machines

The Zeeko '*Precessions*' polishing process is implemented in a series of CNC machines. Since an

IRP200 with 200mm capacity was first successfully assembled in 2000 (Walker et al.*,* 2001B),

Zeeko has developed a range of machines with a capacity of up to 1600mm diameter with

associated metrology for the corrective polishing of complex optical surfaces. **Figure 3.4** shows

a range of IRP machines from 50mm to 1600mm capacity.

Figure 3.4 Zeeko's machines (Zeeko, 2011)

Mechanical and control systems of these machines are built according to CNC machine-tool

principles, and move the polishing tool with respect to the work-piece surface in X, Y, Z, and

two rotational axes (A, B). The work-piece itself may be rotated (C- axis) and the tool is also

spun (H-axis) for high removal rate (Walker et al., 2006A). **Figure 3.5** shows the 7-axis motion

of an IRP1200 machine. The A and B axes intersect at a point in space (virtual pivot) located on

the axis of rotation of the tool spindle. The centre of curvature of the spherical polishing tool

(bonnet) is arranged to coincide with the virtual pivot.

The IRP1200 machine (the main machine used in the work of this thesis) is bridge based and built on a 6000kg polymer-granite cast base. This gives excellent stability and damping. Two symmetrical Y slide-ways carry a hollow polymer-granite bridge. The bridge carries X slide-ways and a driver/encoder system. The Z-axis carriage is mounted off the X-axis, and carries the virtual pivot assembly. The part is mounted on the horizontal turntable with its axis vertical, via a bespoke mounting fixture. For processing small parts on the large machine, standard Schunk chuck adaptors are available (Walker et al., 2006A).
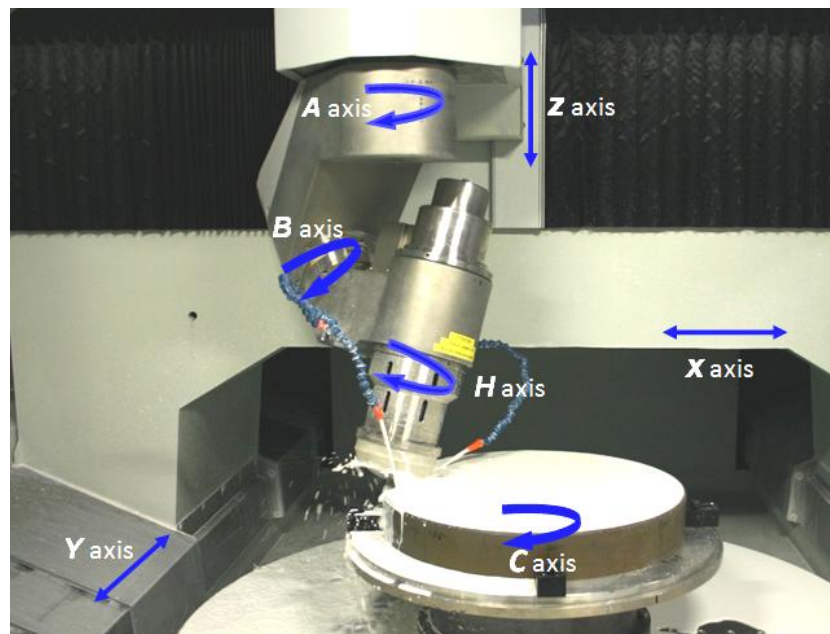
Figure 3.5 7-axis motion of IRP1200 machine (picture by the author, 2011)

A Zeeko IRP1600 CNC polishing machine (1600mm capacity) with integrated test tower has been installed at OpTIC Glyndŵr in St Asaph, North Wales, in 2010 for the production of prototype segments for the European Extremely Large Telescope (E-ELT). This is of similar construction to the IRP1200, as shown in **Figure 3.6**.

A master-spherical-segment (MSS) provides the reference for the measurement of E-ELT aspheric segments. It is a 1.5m corner-to-corner hexagon, 84m radius part, and was polished on the IRP1600 in June 2011. The form error was PV= 88.5 nm, RMS = 16.8 nm. The MSS constitutes the reference with respect to which all segments will be compared in radius and off axis distance (Walker et al., 2011B).

Figure 3.6 IRP1600 machine and test tower (picture by Dr. Yu, May 2011)

3.3 Choice of tooling

Zeeko IRP-machines support a wide range of sub-diameter tooling (Walker et al.*,* 2006B and 2006C). This flexibility provides the possibility of accommodating different process steps on the same machine, reducing the risks of transportation and greatly saving process time and cost.

3.3.1 Bonnet tools

This is the standard tooling. The bonnet tool comprises an inflated membrane or solid elastomer, covered with a standard polishing cloth such as polyurethane or Uni-Nap cloth. It operates in the presence of pumped, re-circulated slurry, typically cerium oxide. A range of tool sizes has been designed from R20mm up to R320mm for the different process stages, as shown in **Figure 3.7**. For instance, large bonnets can be selected for the removal of sub-surface damage and low spatial frequencies, whereas a small bonnet may be used for the final correction and edge quality.
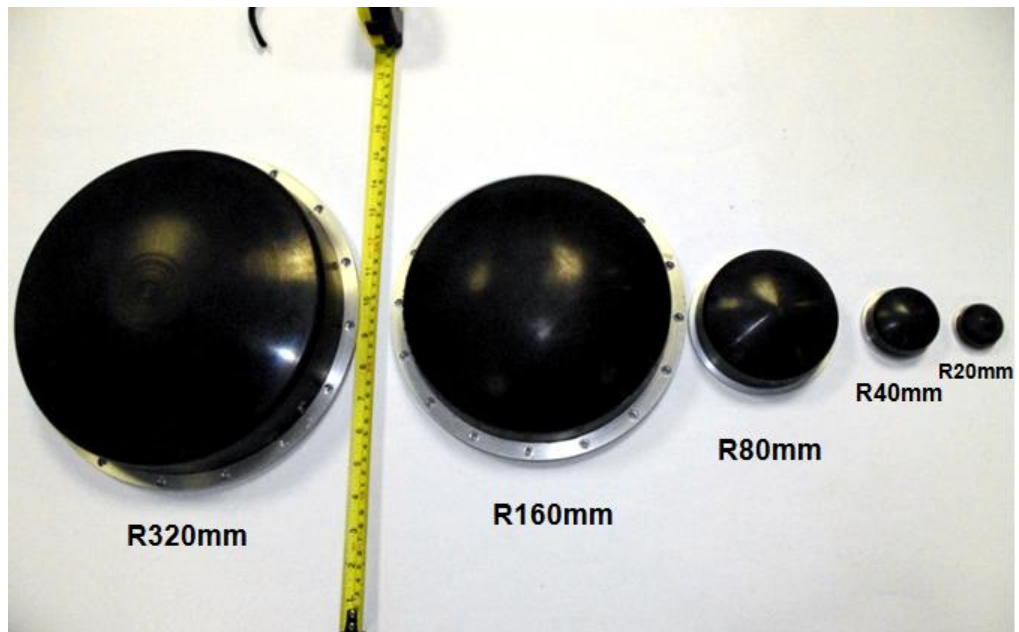
(a) Inflated bonnet tools with different size
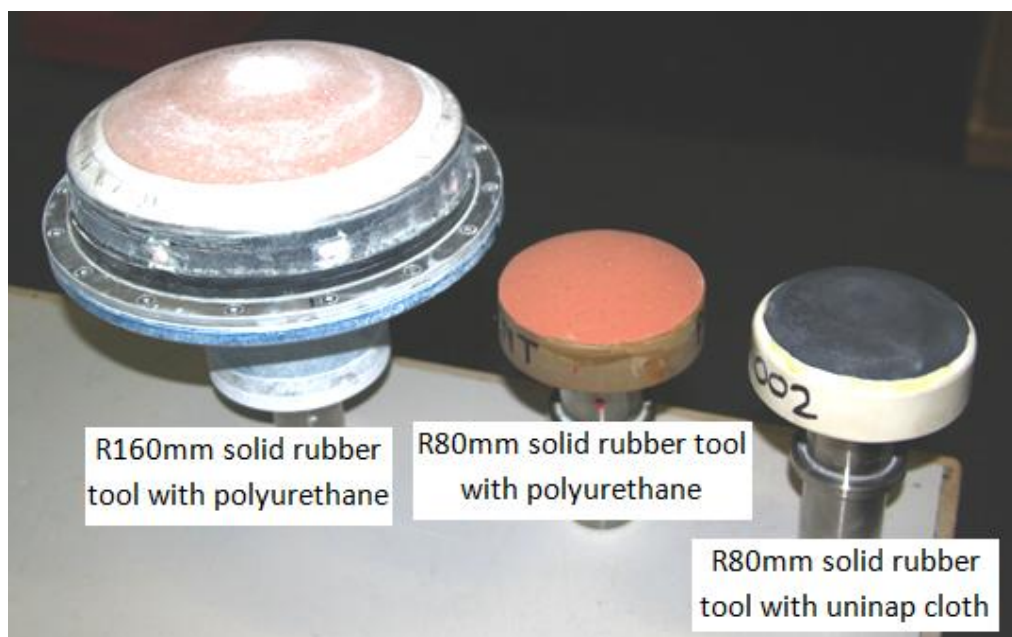
(b) Solid rubber bonnet tools with different polishing cloths

Figure 3.7 A range of bonnet tools for '*Precessions*' polishing technique (picture by the author, 2011)

3.3.2 Pitch process

Typically, it is an effective 'smoothing process' to remove mid-spatial frequency residuals in the final stage. The polishing pitch can be designed variously (for example, different sizes and shapes, as shown in **Figure 3.8**) and mounted on the 'Zeeko' machine, working with cerium oxide. This flexibility is currently being developed for the edge-control programme. The details will be discussed in the **Chapter 7**.
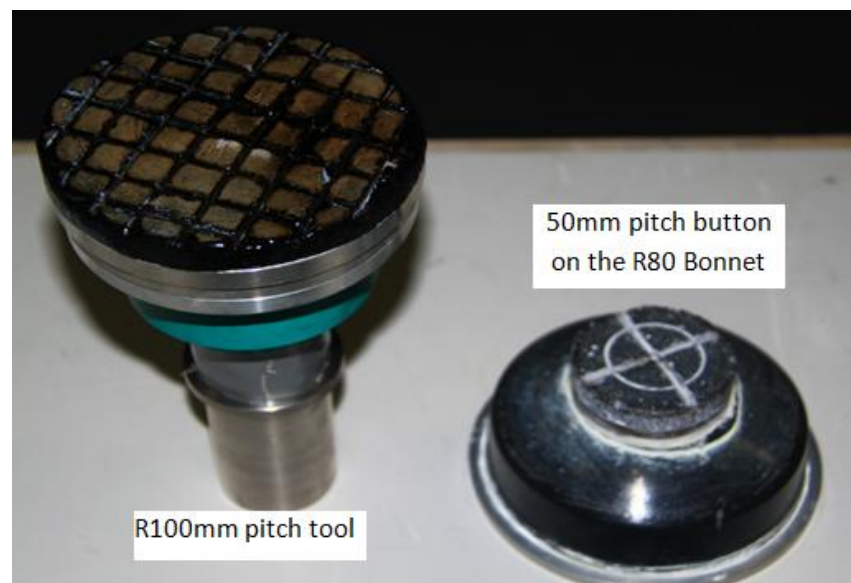
Figure 3.8 The different pitch tool design (picture by the author, 2011)

3.3.3 Grolish process

BoX™ grinding technology has been adopted in the E-ELT segment process chain to grind the aspheric form directly into the surface. There is only a single edge of the 'cup wheel' which contacts the working surface in the BoX™ grinding process, and such a small contact-area introduces mid spatial frequency features.

The grolishing process is a wide range of intermediate processes between grinding and polishing. The main role of this process is to remove mid spatial features from grinding, and provide a fast material removal process. In this case, the working surface cemented to the surface of the bonnet is hard, and typically a metal such as aluminium or brass. The loose-abrasive slurry may be carborundum or diamond, and applied locally rather than by a recirculation pump. In 2007, D. D. Walker et al., (2007) have investigated the variations on three types of grolishing processes as applied to Zerodur and SiC. The volumetric material removal rate of up to 37mm^3/mins was achieved. The results also show approximately 10µm of sub-surface damage that is of an equivalent level to the BoX™ ultra-precision grinding process (using a hard tool). This is due to the flexibility of the bonnet tool, which absorbs the vibrations during the grolish processing. **Figure 3.9** shows a grolish tool mounted on the Zeeko polishing machine of which a 50mm diameter brass-button has been cemented on the R80 inflated bonnet tool (Yu et al., 2011).

Figure 3.9 Grolishing tool mounted on the IRP1200 machine (Yu et al., 2011)

3.3.4 Zeeko-Jet

In this model, slurry is pumped at high pressure through jets, and removes material by direct impact with the surface of the part. Hybrid machines (such as IRP1200, IRP1600) accommodate both jet and bonnet based processes with a simple interchange (Walker et al*.,* 2006B). This is invoked by unscrewing and removing the Schunk Chuck that holds the *Classic* bonnet, and replacing it with the jet nozzle assembly. The jet is directed towards the virtual pivot point of the machine, which is the intersection of the machine's A and B rotation axes. The machine is adjusted so that this point is located exactly on the surface of the part, as shown in **Figure 3.10**. This mode on the Zeeko polishing machine provides an alternative process for the stage of final surface finishing. It has potential for edge-correction, and reaching into deep feature (e.g. moulds and dies).

Figure 3.10 The Zeeko-Jet module on the IRP1200 machine (Walker et al*.,* 2006B)

3.3.5 Specialised tooling

The standard machine tooling interface can carry a variety of specialized tooling such as ring-laps, hard tools etc. Any Gaussian process will leave some high frequency residue, so these specialised tools are designed with aim to clean these up. **Figure 3.11** shows a ring tool on the IRP600 machine with a 500mm diameter part. The ring tool carries a compliant neoprene layer on which hard polishing facets are mounted. The tool is passively articulated in order that it remains in intimate contact with the part.

Figure 3.11 Ring tool on the IRP600 machine (Walker et al.*, 2006B)

3.4 Preparing for polishing

Similar to other computer controlled polishing techniques, the '*Precessions*' process uses a well characterized bonnet tool driven by a numerically controlled machine. For corrective polishing, the motion of the bonnet is optimized to vary the dwell time on the surface of the part according to the desired removal and the tool influence functions. This is an iterative process, which is continued until that target accuracy of the surface of the part has been

achieved. The dwell time map and tool path are defined separately. The traverse speed along

the tool path is modulated, thus that the integrated time at each point on the surface accords

with the dwell time map. However, this may demand speeds/acceleration beyond the machine

capability, due to high slopes or minimal required removal. This is overcome by adding a DC-

pedestal to the overall removal profile. The '*Precessions*' process flow is shown in **Figure 3.12**.

The Zeeko machines are supplied with a series of software for the '*Precessions*' process which

include Metrology Toolkit, Precessions optimization software and Tool Path Generator (TPG).

These software provide standard interfaces between metrology devices and the polishing

machine. The Metrology Toolkit is capable of reading data from a wide variety of metrology

instruments, in order to process and analyze it. '*Precession*' software is used for the

optimization of the dwell time map, and TPG outputs a CNC file which is to control the

polishing machine.
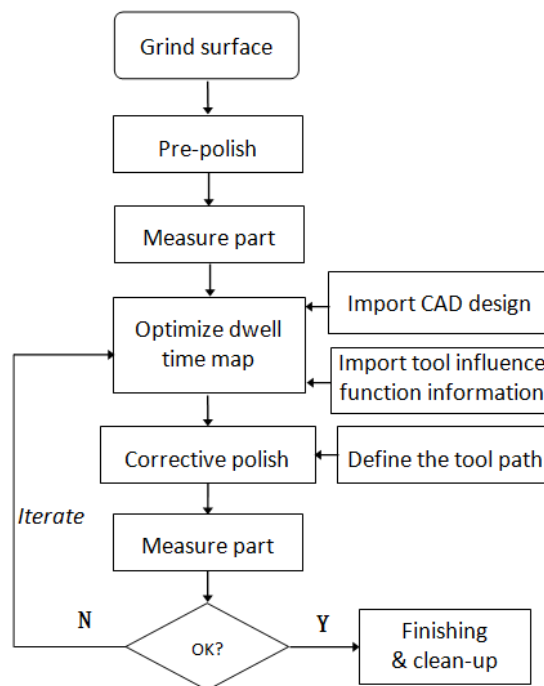
Figure 3.12 '*Precessions*' process flow (graph by the author, 2011)

3.4.1 Preparing bonnet tool

The A and B rotation axes of the machine intersect at a virtual pivot (V-P) point. The centre of curvature of the bonnet surface should be at the V-P. Significant departure can lead to asymmetry of the final figure of the part, the details will be discussed in **Chapter 6**. For an unused bonnet, a dressing operation 'trues' the surface and removes local irregularities as a result of gluing the cloth to the rubber membrane of the bonnet. The procedure of the operation is shown in **Figure 3.13**.

The cloth is pressed into a metal mould pair to take the spherical form of the bonnet, and then cemented in place. The bonnet with cloth is mounted in the machine's Schunk chuck and inflated to its operating pressure. The surface of the cloth is trimmed using either a fixed single-point tool or a grinding cup wheel.
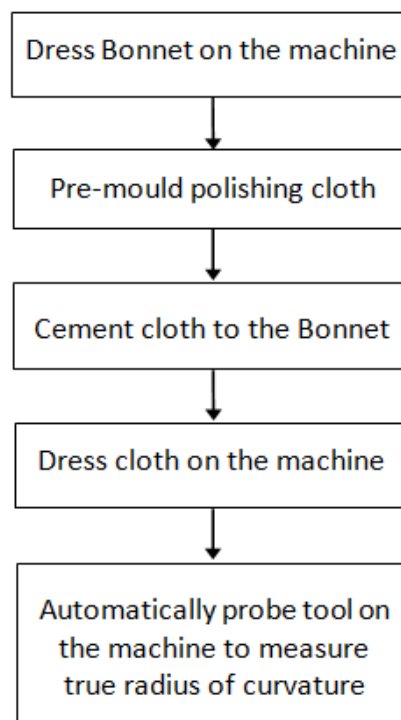
Figure 3.13 Tool preparation procedure (graph by the author)

After the cloth has been trimmed and trued-in, the absolute radius of curvature of the bonnet system and mismatch of the bonnet surface need to be tested. The machine is furnished with a precision reference ball mounted on a shaft that is located in the Schunk chuck on the machine, as shown in **Figure 3.14**. This is used to probe the surface of the bonnet in an automated procedure.
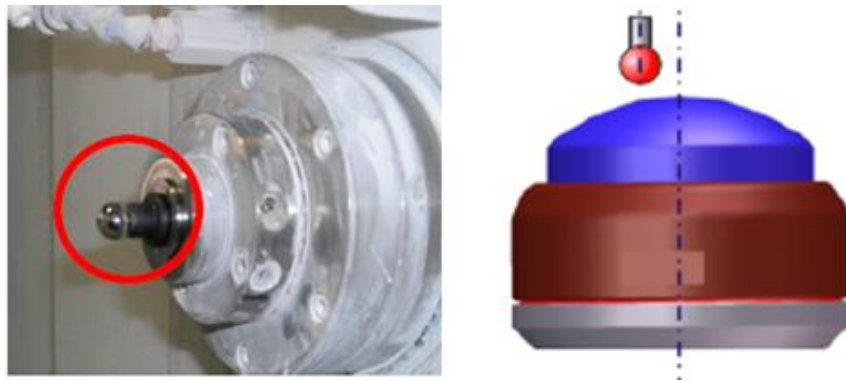
Figure 3.14 Probing of bonnet surface using a reference ball on the machine (picture on the right by author; the picture on the left is from Zeeko CNC software)

3.4.2 Tool path

The tool path is defined as the movement of the polishing tool, which covers the entire surface. The different tool path can affect the final characteristics of the finished surface, such as the surface texture and form errors. Zeeko software provides several tool path patterns.

A raster tool path is the most often used in Zeeko software and is suitable for any shape of the part, which covers the entire part efficiently and does not produce any anomalies, because the entire surface gets the same treatment from the tool, as shown in the **Figure 3.15** (a). The repetitive action of the raster path creates a periodicity in the texture of the surface, which can be reduced by decreasing the track spacing or increasing spot size, or by using an auxiliary treatment such as a pitch tool.

An adaptive tool path has been developed with edge control using a 'Nodding bonnet' technique (e.g. on a polygon). This starts as a polygonal spiral at the periphery of the part, and then progressively transforms into a regular spiral towards centre, as shown in **Figure 3.15** (b).

In 2008, Dunn et al., (2008A and 2008B) developed a 'unicursal' tool path, which is called the 'random tool path', which never crosses itself, see **Figure 3.15** (c). Because of this property, the 'random tool path' can avoid periodic signature on the surface, which happens with a regular tool path.
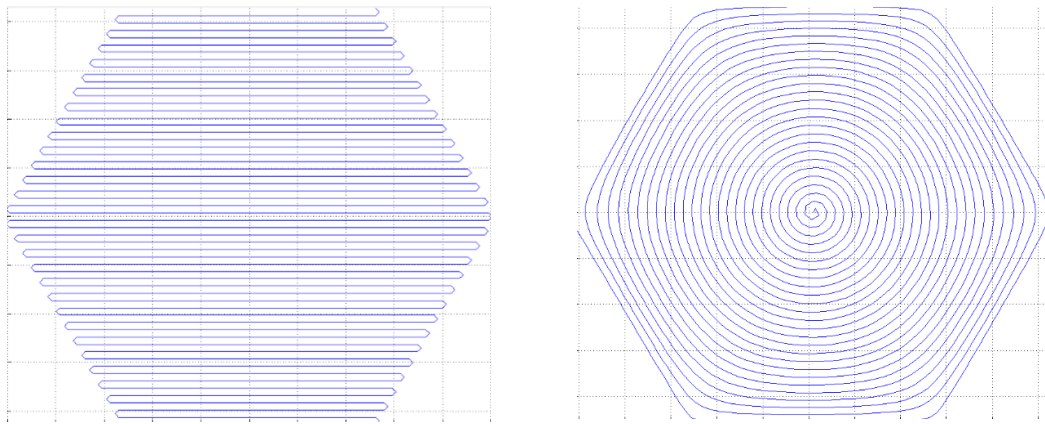
(a) Raster tool path   (b) Adaptive tool path
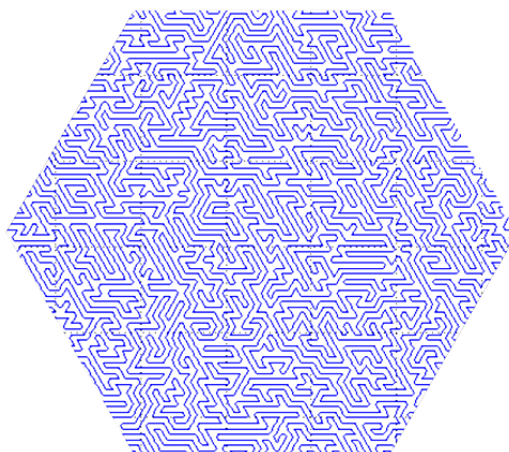
(c) Random tool path

Figure 3.15 The different tool paths (pictures from Zeeko software TPG2.0.0.b7)

3.4.3 Polishing parameters

To achieve the polishing accuracies, there are several machine parameters, which need to be chosen. The settings of these parameters will vary depending on the form and material of the part. **Figure 1.16** shows the parameters interface in Zeeko software.
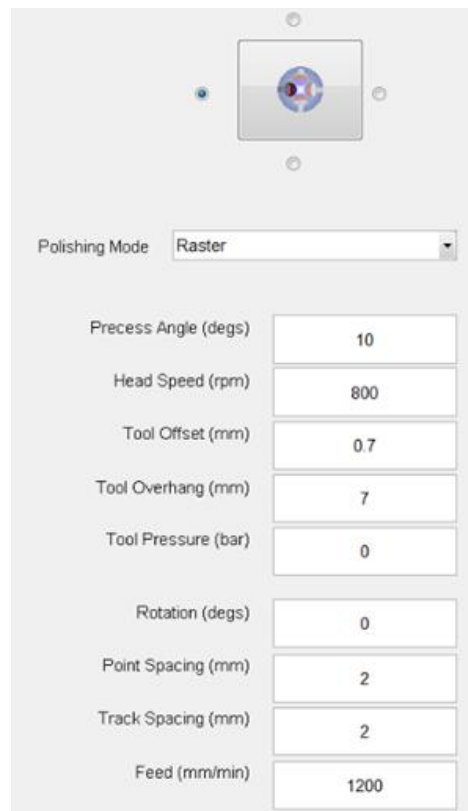
Figure 3.16 The interface of polishing parameters (picture from Zeeko software TPG2.0.0.b7)

1. Precess angle (degs)

The precess angle is related to the angle at which the centre line of the bonnet and the 90° perpendicular between part and bonnet intersect as shown in **Figure 3.1**. This parameter determines the removal rate and texture of the surface of the part. 10 to 20 degrees is the

normal range that can be chosen for the bonnet tool. At the grolishing and pitch tool mode, 0 degree precess angle is chosen.

2. Head speed (rpm)

This parameter is the speed of rotation of the H-axis (tool spindle) of the machine. The H-axis can be rotated in either a clockwise or an anticlockwise direction. Head speed determines the removal rate according to the Preston equation. Head speed can be chosen up to 2000rpm on the IRP1200 machine and depends on the size of the bonnet.

3. Tool offset (mm)

The tool offset (bonnet compression) defines the delivered spot-size for a specific size of bonnet. Progressively lifting the bonnet gives scope to reduce the spot-size as the spot encroaches on the edge of the part, which has been successfully used for the edge control programme (this is discussed in **Chapter 5**). Different ranges of spot-size can be provided by exchanging bonnets between runs, and radii of curvature from 20mm to 320mm are available.

4. Tool pressure (bar)

The bonnet tool can be pressurised by a pump integrated in the Zeeko machine. Up to 3 bar can be chosen depending on bonnet size.

5. Raster & Spiral track spacing (mm)

The track spacing affects the 'cusping' feature on the surface of the part. A diagram of the 'cusping' feature is shown in **Figure 3.17.** Selection of track spacing depends on the tool size, spot-size and removal depth.
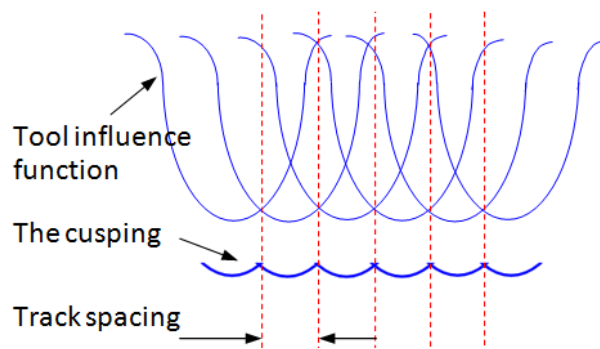
Figure 3.17 The diagram of the 'cusping' feature (drawn by the author)

6. Traverse Speed (mm/min)

Traverse feed determines the dwell time at each demanded contact point on the surface of the part. The 'dwell time map' is the main output from optimisation, and the polishing tool is traversed by the CNC machine according to the 'dwell time map' to achieve target surface of the part.

3.5 Surface metrology

For the different process steps, the specific metrology instruments and techniques for this thesis are outlined below:

3D-Form measurement

The form term is measured by the 4D simultaneous phase-shifting interferometers at 633nm in the work of this thesis. The 4D interferometers can be set up horizontally or vertically on the measurement table, and also can easily be set up above the IRP polishing machine, as shown in **Figure 3.18**. The CCD format is 1000 by 1000 for PhaseCam6000 and 600 by 800 for PhaseCam4010. A set of lenses (f/1, f/2.2, f/4, f/6, and f/8) is available for measurement of different curvatures.

Figure 3.18 4D interferometers (PhaseCam6000 on the left, PhaseCam4010 on the right) (picture by the author, 2011)

2D-Form Talysurf

'Extended Range' Form Talysurf (shown in **Figure 3.19**) is used for measurements of 2D form or 2D tool influence functions (TIFs). This Form Talysurf has a 300mm capacity and an accuracy of 0.3μm peak-to-valley over the full range. In the work of this thesis, for the case of which edges of part have been rolled down or turned up, the resulting slopes can be beyond the measurement range of full aperture interferometry. To identify the shape of the edges, 2D scannings are required. Moreover, 2D Profilometer data is convenient to build an absolute removal depth by making a fiducial groove on the surface of the part.
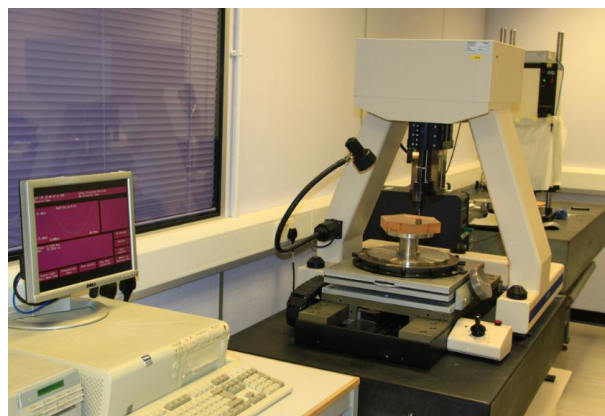
Figure 3.19 'Extended Range' Form Talysurf (picture by the author, 2011)

Swing Arm Profilometer for measurement of 3D tool influence functions

For the measurement of the influence function of a bonnet tool, 2D profiles are adequate; but for the full 3D correction of surface, 3D maps of tool influence functions (TIFs) may be required; specially, for those TIFs with non-axial symmetry (for example, TIFs of 'Nodding' bonnet). For the ESO project, spot sizes up to 150mm are required for fast removal. The traditional measurement is to use a profilometer with 3D capability, such as the 3D Taylor Hobson Talysurf, which has a 300mm gauge range. A swing arm profilometer with 600mm diameter measurement range was built at National Physical Laboratory (NPL), which is used for measurement of 3D TIFs, as shown in **Figure 3.20**.

Figure 3.20 Swing Arm Profilometer (Jing et al., 2010)

Surface Texture

Surface texture is measured using an ADE Phase Shift MicroAXM white-light texture interferometer (as shown in **Figure 3.21**), which has sub-nanometre resolution. The current instrument is mounted on a microscope stand that gives 250mm measurement range.

Figure 3.21 ADE-MicroVAX light texture interferometer (picture by the author, 2011)

Recently, 4D Technology has developed an instantaneous white light interferometer for Zeeko Ltd, which is called Zeeko STA1. This is designed to operate in the tooling chuck of Zeeko IRP machines. The STA1 has been used for the surface texture measurement of 1.5m master-spherical-segment (MSS) hexagonal part on the IRP1600 machine, shown in **figure 3.22**.

Figure 3.22 STA1 light texture interferometer on IRP1600 (Walker et al., 2011B)

3.6 Summary

'*Precessions'* polishing technique has been adopted as the core technique for fabrication of prototype mirror segments for E-ELT. The main research of this thesis is based on Zeeko's machine (IRP1200). This chapter provides the details of this technique, including the principle of '*Precessions*', IRP machines and tooling. The metrologies of the surface for this thesis are also described in this chapter.

Chapter 4

Measurement and modelling of tool influence functions

The tool influence functions (TIFs) characterise the local effect of the process and therefore are of fundamental importance. Identification of the TIF is crucial for achieving a successful deterministic '*Precessions*' polishing process. The main objective of this chapter is to establish a numerical model that is capable of predicting the shape of TIF for a given tool and condition. This model will help to optimise the 'tool lift' parameters for edge control that is discussed in the next chapter.

4.1 The need for modelling of the tool influence functions

The Tool Influence Function (TIF) is a material removal map for a given tool and work piece. Like other Computer Numerical Controlled (CNC) polishing, a predictable and stable TIF is essential for the '*Precessions*' polishing. The shape of the TIF influences the capability of error correction (surface texture and form accuracy). The removal rate of the TIF plays an important role in determining the process time. The TIF of a bonnet tool relies on at least 8 parameters (precess angle, tool Z-offset, head speed, tool pressure, dwell time, polish cloth, slurry and glass type). These polishing parameters have already been discussed in **Section 3.4.3**. A TIF also depends on the precess motion (static or dynamic see **Figure 3.2**). Furthermore, in the case of TIF at the edge of the part, overhang of the edge is another important parameter. The aim of this work is to establish a model that is capable of predicting the shape of TIF for a given tool and condition.

4.2 Material removing model based on the Preston equation

The theoretical basis of prediction of material removal in optical surface polishing was presented by Preston (1927) in 1927. This was discussed in **Section 2.3**. As an emphasis, it is repeated as follows:

$$\Delta h(x,y) = k \cdot v(x,y) \cdot p(x,y) \tag{4.1}$$

where:

$\Delta h(x, \text{y})$ - Removal in unit time at point (x, y)

k - Preston coefficient, related to the work piece material, polishing-tool, polishing slurry and temperature of work environment

$v(x, y)$ - Instantaneous relative surface velocity of polish pad at point (x, y)

$p(x, y)$ - Instantaneous pressure of the polishing pad at point (x, y)

Define the average removal value of surface materials $R(x, y)$ in unit time T as the tool influence function, i.e.:

$$R(x, y) = \frac{1}{T}\int_0^T \Delta h(x, y) \cdot dt = \frac{1}{T}\int_0^T k \cdot v(x, y) \cdot p(x, y) \cdot dt \tag{4.2}$$

Define the revolution period of the polishing tool:

$$T = 2\pi/\omega_0$$

where, ω_0 is the angular velocity of the polishing tool. Since, removal function $R(r)$ can be written as:

$$R(r) = \frac{1}{T}\int_0^T k \cdot v(x, y) \cdot p(x, y) \cdot dt = \frac{k}{2\pi}\int_{-\theta_0}^{\theta_0} v(x, y) \cdot p(x, y) \cdot d\theta \tag{4.3}$$

where, θ is the rotation angle of the polishing tool.

The removal function $R(x,y)$ can be determined by equation 4.3, if the velocity distribution $v(x,y)$ and the pressure distribution $p(x,y)$ can be obtained. The simulation of velocity and pressure distribution is introduced in the following sections.

4.3 Modelling of the velocity distribution *v(x,y)*

A sketch of the movement of a precessed bonnet is shown in **Figure 4.1**. The velocity relation of any point in the polishing contact zone is shown in **Figure 4.2**.
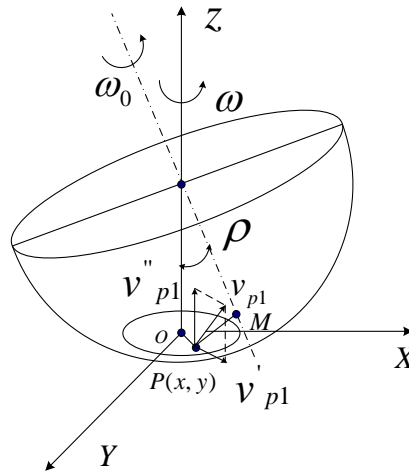
Figure 4.1 Sketch of space movement of the tool of the precess (drawn by the author)
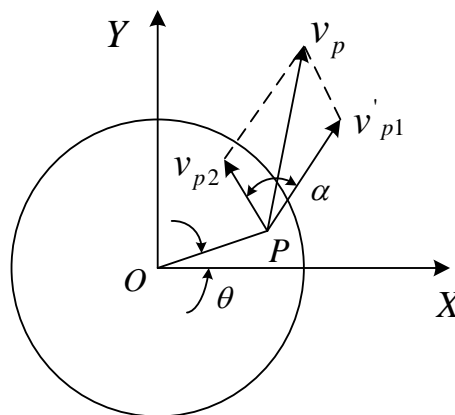
Figure 4.2 Velocity relation of any point in polishing contact zone (drawn by the author)

Where:

$P(x, y)$ is any point in polishing contact zone;

ω_0 is the angular velocity around axis of tool;

ω is the angular velocity around a normal work piece;

o is the centre of polishing spot;

ρ is the process angle;

d is the compression value of tool (Z-offset);

R is the radius of curvature of the tool

According to the geometry of precess in the polishing area, the velocity component distribution $v'_{p1}(x, y)$ can be expressed as:

$$v'_{p1}(x, y) = 2 \cdot \cos \rho \cdot (R - d)^{-1} \sqrt{s \cdot (s - \alpha) \cdot (s - \beta) \cdot (s - \gamma)} \cdot \omega_0 \qquad (4.4)$$

where：

$$\alpha = [(R-r)^2 + x^2 + y^2]^{1/2}; \qquad \beta = (R-d) \cdot (\cos \rho)^{-1}; \qquad \gamma = [y^2 + [(R-d) \cdot tg\rho - x]^2]^{1/2};$$

$$s = \frac{1}{2} \alpha \cdot \beta \cdot \gamma$$

$$v_{p2} = r \cdot \omega \qquad (4.5)$$

$$v_p(x, y) = \sqrt{(v'_{p1}(x, y))^2 + (v_{p2}(x, y))^2 + 2 \cos \alpha \cdot v'_{p1}(x, y) \cdot v_{p2}(x, y)} \qquad (4.6)$$

Based on equation 4.6, relative velocity distribution function in the polishing zone has been simulated using MatLab code. **Figure 4.3** shows the simulation results. The parameters in the

modelling are: 80mm tool radii of curvature, 0.7mm Z-offset and 0°, 15° precess angle. To simplify the modelling process, normalization (scaling magnitude of velocity from 0 to 1) has been applied in the simulation. From **Figure 4.3 (a)**, it can be seen that material removal at central point is zero when precess angle is 0°, because the surface speed at the central point is zero. **Figure 4.3 (b)** is velocity distribution when precess angle is 15°, note the absence of zero surface speed anywhere in the tool influence function.
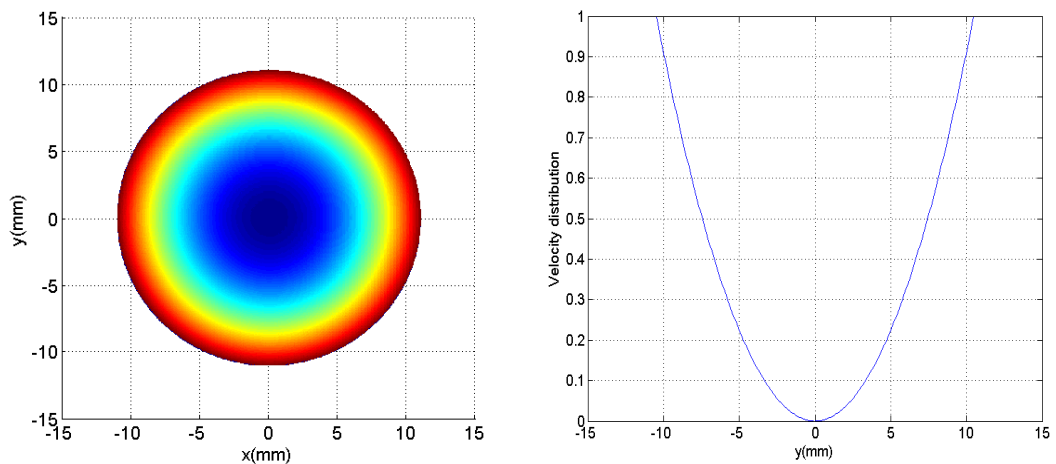
(a) Precess angle=0°
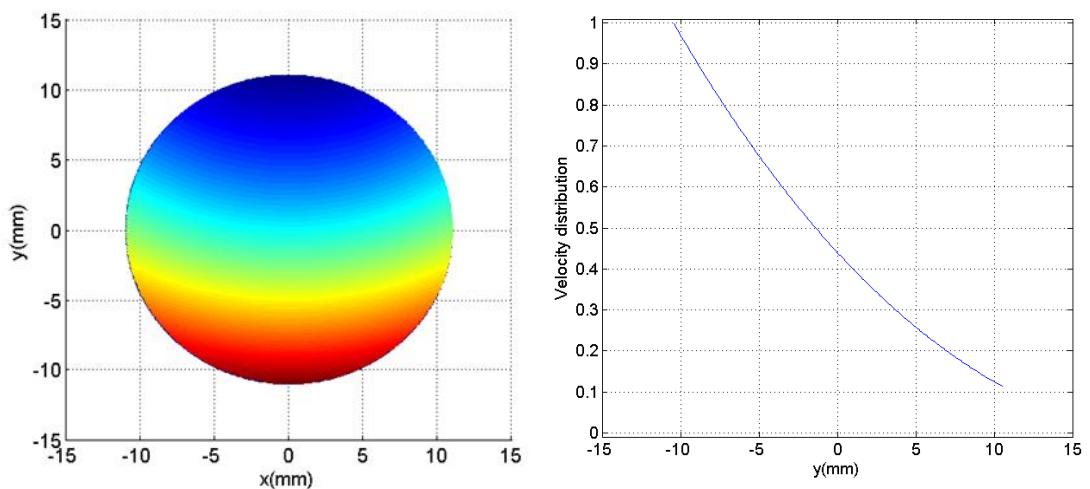
(b) Precess angle=15°

Figure 4.3 Velocity distribution normalised simulation results: R80 tool, Z-offset: 0.7mm, where: (a) Precess angle: 0° (b) Precess angle: 15° (author's data)

4.4 Finite element analysis (FEA) for analysis of pressure distribution *p(x,y)*

The finite element analysis method is widely used for analyzing stress, displacement and strain in complicated structures. The basic theory of FEA is to divide a continuum of analysis of the target into a finite number of smaller individual 'elements'. In the model, these elements are interconnected by a stiffness matrix.

The ANSYS software package is a mature and versatile commercial finite element analysis (developed by ANSYS, Inc.). ANSYS has been adopted in structural simulation to solve many challenging engineering problems since 1970 (ANSYS 2011). In this section, ANSYS 8.0 is adopted for the FEA of pressure distribution of the bonnet polishing.

Two FEAs of pressure distribution are carried out in this chapter:

1. R80mm solid rubber tool, Z-offset: 0.7mm, appropriate for the form-correction

2. R160mm solid rubber tool, Z-offset: 2.8mm, appropriate for the pre-polishing and early stage of form correction

4.4.1 FEA model and boundary conditions

The pressure on the work piece is caused by elastic deformation of the tool. To simplify the problem, a thin layer of polishing cloth is considered to be a second order effect and is neglected in the modelling. A 100mm x 100mm square, 10mm thick, Zerodur part was chosen for the model. The bonnet tool was designed as a molded unit in Natural Rubber (BS-1154: 2003). The material properties for the modelling are listed in **Table 4.1.** For R80mm tool,

0.7mm Z-offset and 15° precess angle is chosen for the modelling. For R160mm tool, 2.8mm Z-offset and 0° precess angle is chosen for the modelling.

Table 4.1 The materials characteristics for the modelling (Dohring et al., 2006):

	Density (kg/m^3)	Yong's modulus (N/m^2)	Poisson's ratio
Zerodur	2.53 x 10^3	9.30 x 10^{10}	0.30
Natural Rubber (BS-1154:2003)	1.12 x 10^3	1.34 x 10^6	0.24

The FEA of the bonnet tool polishing model is defined as a contact problem of two surfaces. A set of contact pair is created between the surface of the tool and the polishing surface of the part.

During the polishing process, the back surface of the part is fixed on the support system. Thus, all degree of freedom (DOF) of the back surface is constrained with 0 displacements. The top surface of the tool is fixed on the polishing machine. The bonnet tool is depressed by the Z-offset to deliver a spot-size along the Z-direction. Thus, the top surface of the tool is constrained with 0 displacements along X-axis and Y-axis and -0.7mm (R80mm tool) and -2.8mm (R160mm tool) displacement along Z-axis. The elements and restraints of the FEA model are shown in **Figure 4.4** and **Figure 4.5**.

The displacement restraints on the back surface of the bonnet (offset=0.7mm)
(x=0, y=0, z= -0.7mm)

R80 solid rubber bonnet

Zerodur part
(100mmx100mm square)

The restraints on the part (fixed)
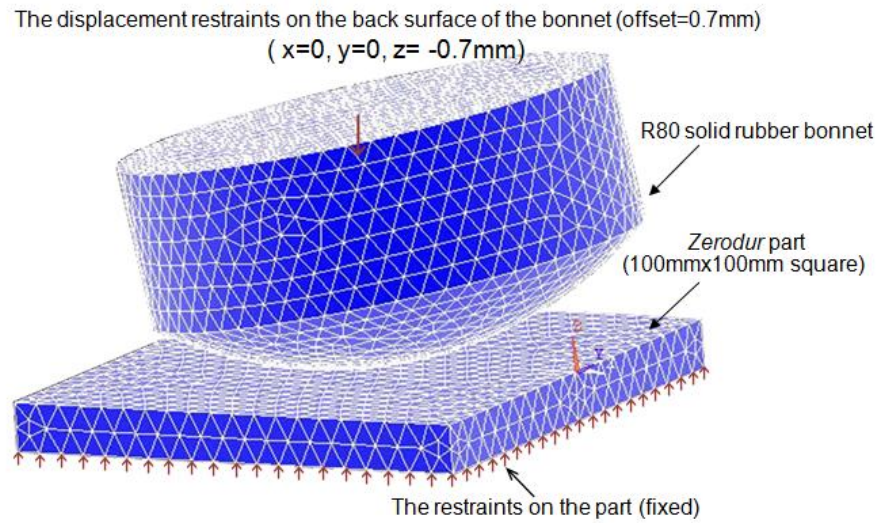
Figure 4.4 The elements and the restraints on the FEM model for R80mm solid rubber tool (author's picture)

The displacement restraints on the back surface of the bonnet (offset=2.8mm)
(x=0, y=0, z= -2.8mm)

R160 solid rubber bonnet

Zerodur part
(100mmx100mm square)

The restraints on the part (fixed)
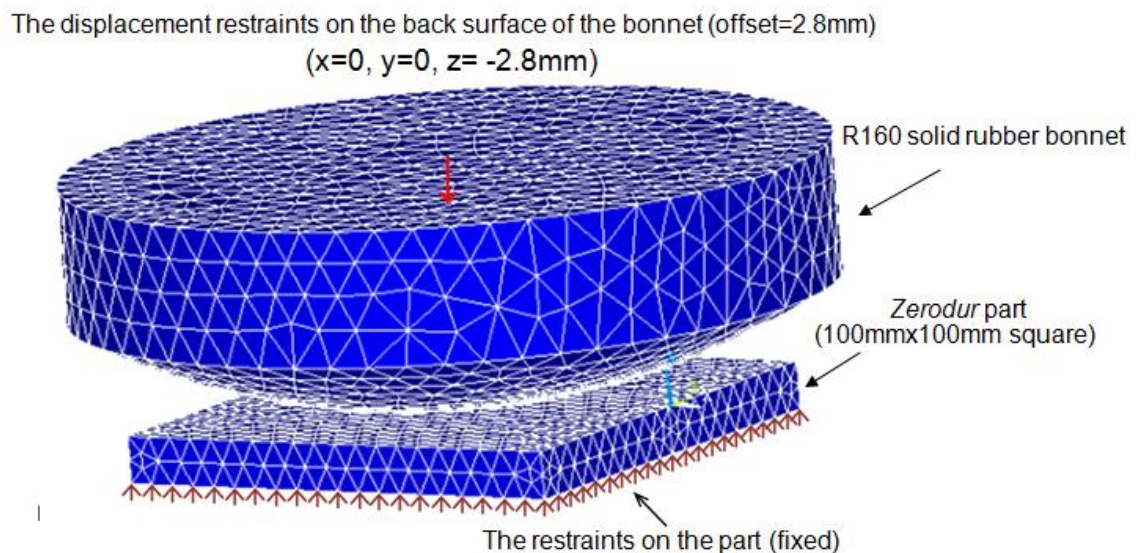
Figure 4.5 The elements and the restraints on the FEM model for R160 tool (author's picture)

4.4.2 FEM results and conclusions

Two simulation runs have been conducted under the boundary and loads conditions, discussed above for R80mm tool and R160mm tool. The simulation results are plotted in **Figure 4.6** to **Figure 4.9**. Note that the slight asymmetry in the **Figure 4.6** and **Figure 4.8** are caused by the precision of the meshing.
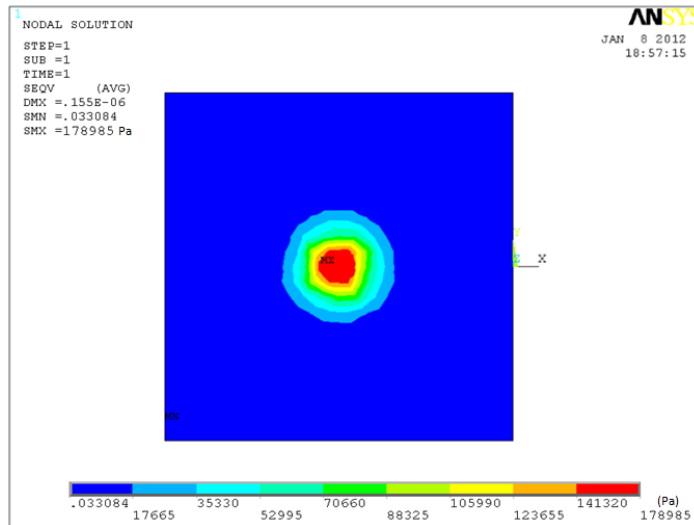
Figure 4.6 R80mm tool absolute pressure distribution simulation results (0.7mm Z-offset, 21mm spot-size) (author's data)
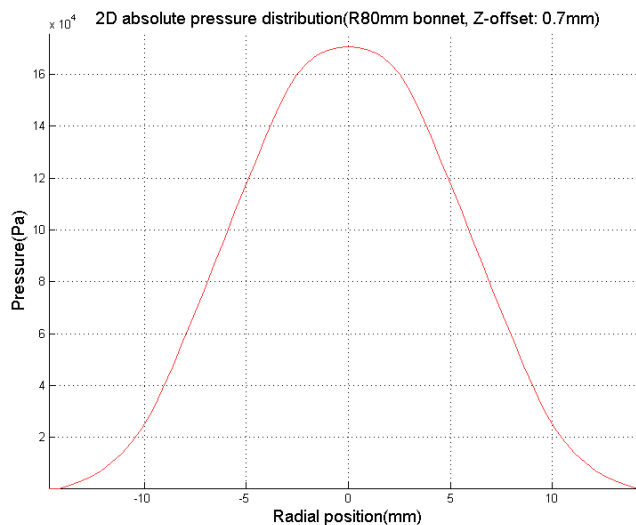
Figure 4.7 2D R80mm tool absolute pressure distribution simulation plot (0.7mm Z-offset, 21mm spot-size) (author's data)
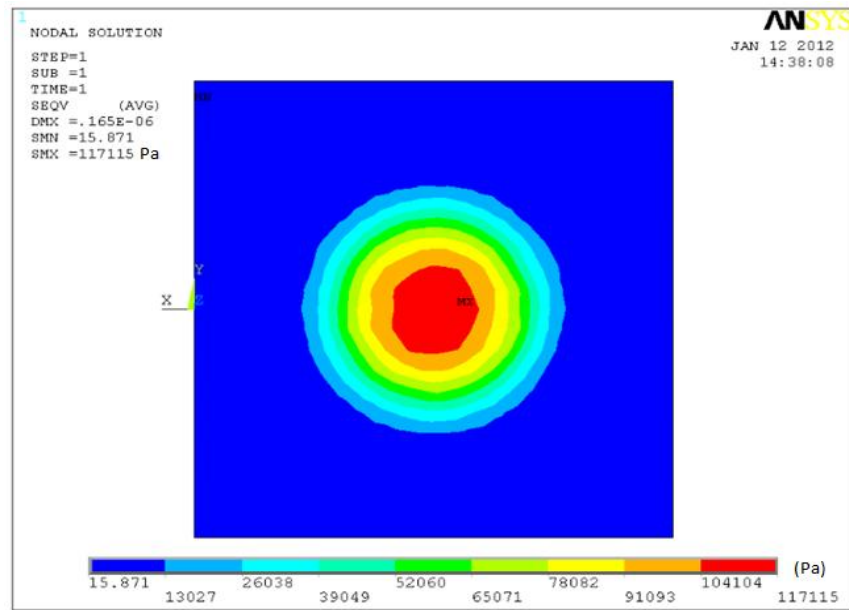
Figure 4.8 R160mm tool absolute pressure distribution simulation results (2.8mm Z-offset, 60mm spot-size) (author's data)
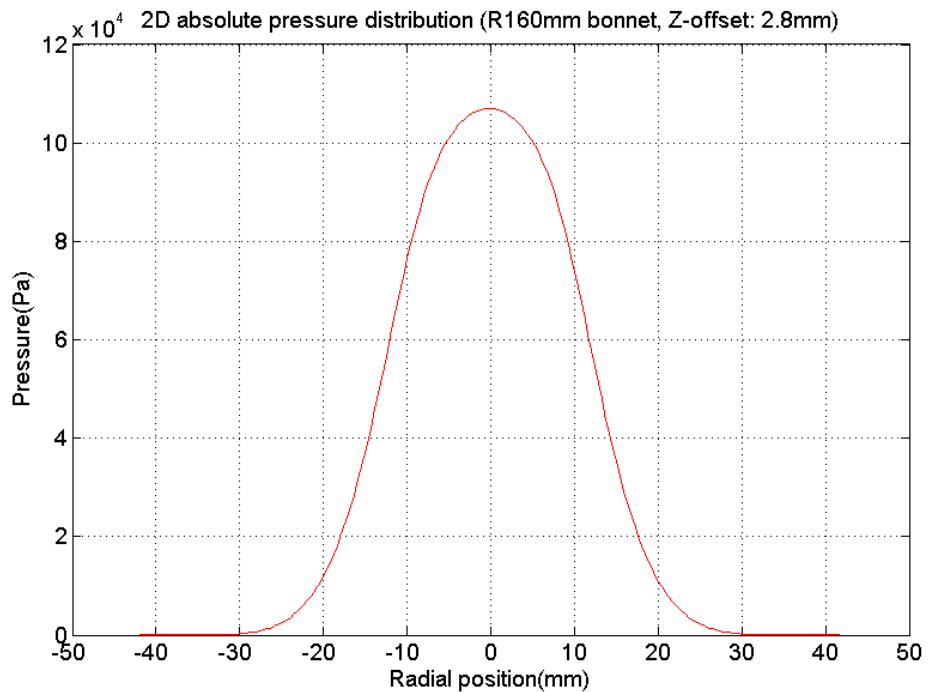
Figure 4.9 2D R160mm tool absolute pressure distribution simulation plot (2.8mm Z-offset, 60mm spot-size) (author's data)

Two conclusions can be made from the FEA results obtained in this section:

1. R80mm solid rubber tool, 0.7mm Z-offset and 15° precess angle, the maximum pressure on the Zerodur part is 1.79×10^5 Pa for the case considered.

2. R160mm solid rubber tool, 2.8mm Z-offset and 0° precess angle, the maximum pressure on the Zerodur part is 1.17×10^5 Pa for the case considered.

To verify the simulation result of pressure distribution, the force on the contact area is measured. The detail of this work is described in the following section.

4.5 Force measurement for verification of the FEA results

The total force f applied on the part should be the same as the integral of the pressure distribution $p(x,y)$ over the part contact area A, which can be described as:

$$f = \iint_A p(x, y)dxdy \qquad (4.7)$$

The pressure distribution simulation results of 0.7mm Z-offset (R80mm tool) and 2.8mm Z-offset (R160mm tool) are shown in **Figure 4.6** to **Figure 4.9.** Thus, the simulated force f_{R80} and f_{R160} can be calculated according to equation 4.7, which are:

$$f_{R80} = 4.19kg$$

$$f_{R160} = 16.43kg$$

To verify the pressure distribution $p(x,y)$ simulation results, the force f on the part has been measured on the machine. OpTIC Glyndwr has developed a device for force measurement. This

device uses three OMEGA (SN: LCM201) standard load cells whose accuracy is ±1.0% (linearity, hysteresis and repeatability combined). The sketch of the set-up of the force measurement is shown in Figure **4.10**. The experimental set-up is shown in Figure **4.11**.
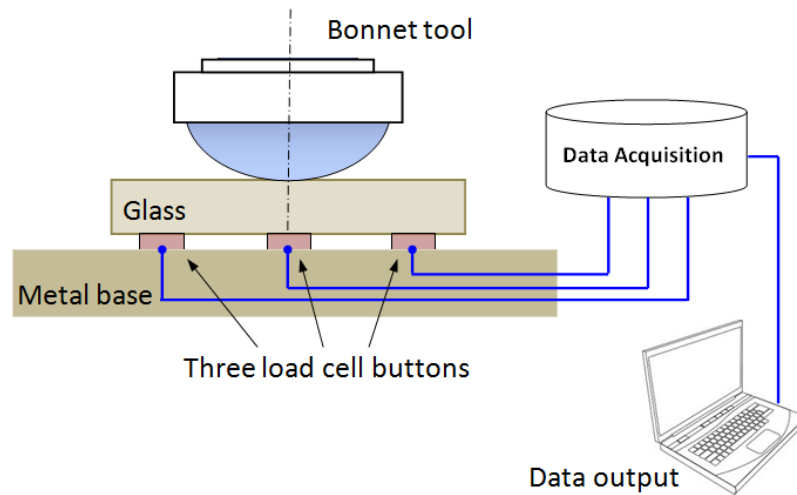
Figure 4.10 The sketch of the set-up of the force measurement (drawn by the author)
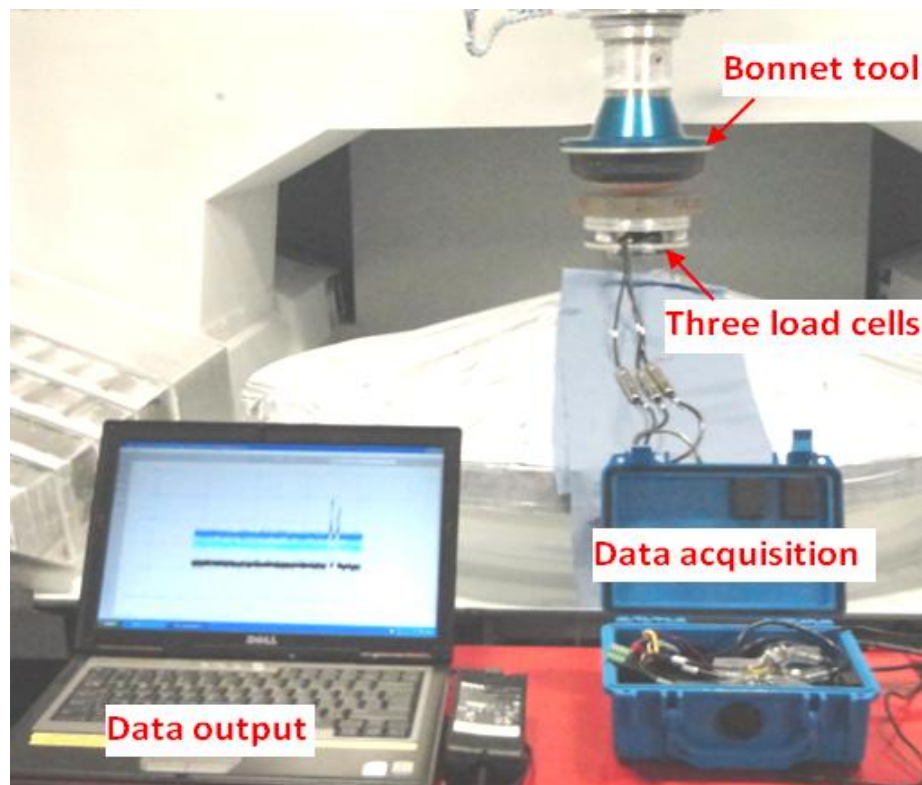
Figure 4.11 The experimental set-up of the force measurement (picture by the author, 2011)

Two sets of force measurements for R80mm tool and R160mm tool were carried out on IRP1200 machine. **Figure 4.12** shows the force of R80mm tool applied on the part with different Z-offset. It can be seen that the force on the part is 4.42kg when Z-offset is 0.7mm for R80mm tool (the simulation result is 4.19kg). **Figure 4.13** shows the force of R160mm tool applied to the part with different Z-offset. It can be seen that the force on the part is 15.87kg when Z-offset is 2.8mm for R160mm tool (the simulation result is 16.43kg). The simulation errors are approximately 5.2% for R80mm tool, and 3.6% for R160mm tool according to the force measurement results.
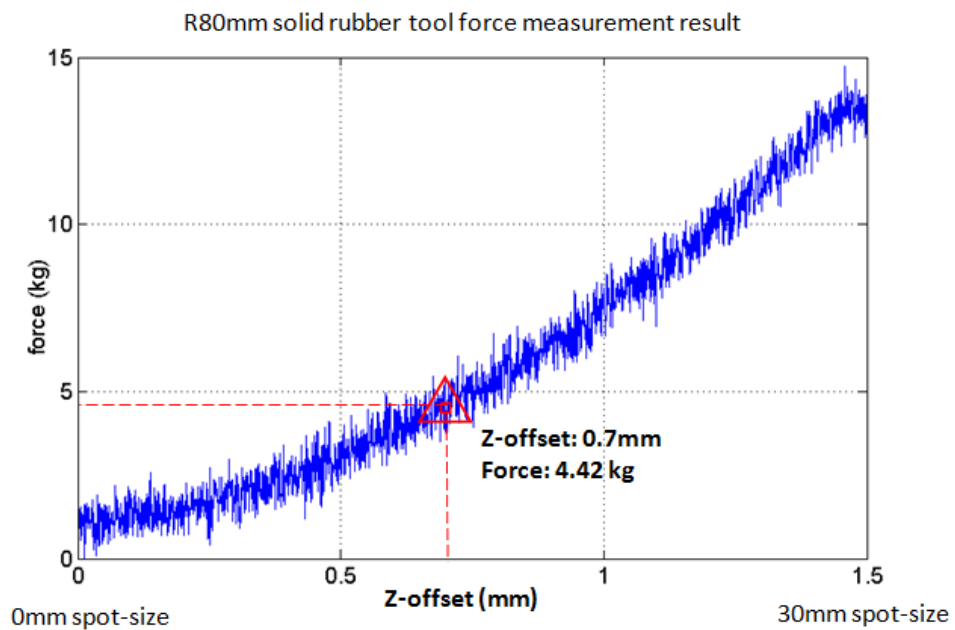
Figure 4.12 The force with different Z-offset measurement result of R80mm solid rubber tool (author's data)
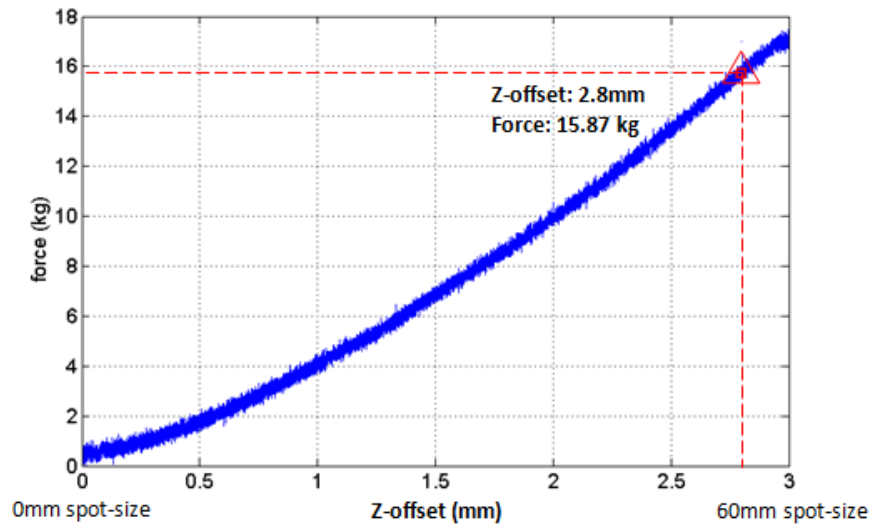
Figure 4.13 The force with different Z-offset measurement result of R160mm solid rubber tool (author's data)

4.6 Modelling of tool influence function (R80mm tool, 0.7mm Z-offset)

After the velocity distribution *v(x,y)* and the pressure distribution *p(x,y)* have been obtained, the tool influence function *R(x,y)* can be modelled according to equation 4.3. This was mentioned in **Section 4.2**, repeated here:

$$R(x, y) = \frac{1}{T} \int_0^T k \cdot v(x, y) \cdot p(x, y) \cdot dt = \frac{k}{2\pi} \int_{-\theta_0}^{\theta_0} v(x, y) \cdot p(x, y) \cdot d\theta$$

As a demonstration of the modelling, the TIF for R80mm tool, 0.7mm Z-offset, 15° precess angle, was modelled using MatLab code. According to the Preston equation, the absolute material removal is also determined by the Preston coefficient *k*, which is a constant, related to the part material, polishing liquid and temperature (see **Section 2.3**). To simplify the modelling result, the magnitude of the TIF has been normalised (scaling of TIF from -1 to 0) in the simulation. The modelling result is shown in **Figure 4.14**.
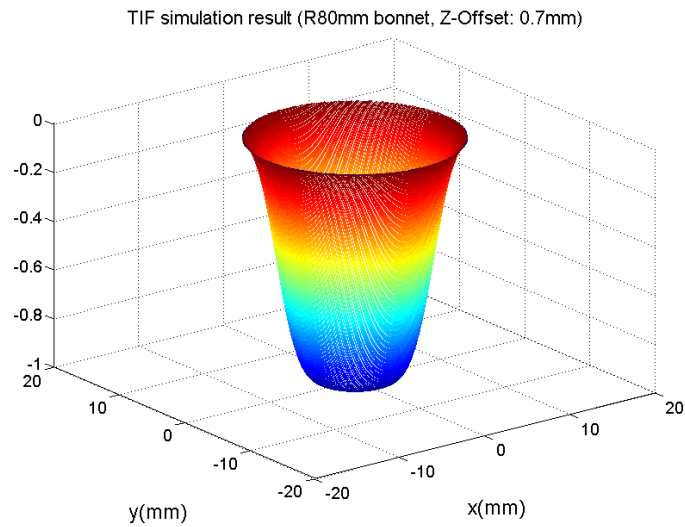
Figure 4.14 The normalised TIF simulation result (R80mm tool, 0.7mm Z-offset, 15° precess angle) (author's data)

To verify the TIF simulation result, an experiment for the generation of TIF has been carried out. The parameters of this experiment are the same as the simulation's parameters (R80mm tool, 0.7mm Z-offset, 15^0 precess angle). For simplification of the comparison with the simulation result, experimental TIF has been normalized by scaling the magnitude of TIF from 0 to -1. The simplified experimental result is shown in **Figure 4.15**.
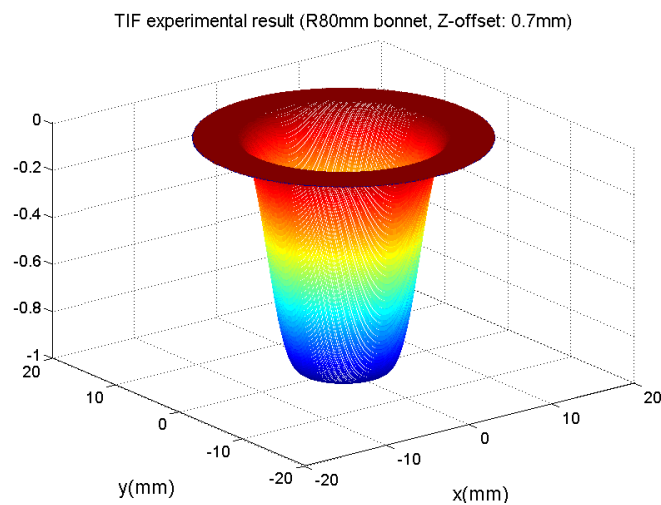
Figure 4.15 The normalised TIF experimental result (R80mm tool, 0.7mm Z-offset, 15° precess angle) (author's data)

Figure 4.16 shows the residuals between normalised experimental and simulated TIF. A 2D comparison of experimental and simulation result is shown in **Figure 4.17**. The relative ratio of residuals and experimental result are 2.2% by RMS and 8.4% by P-V. This shows that simulated TIF's shape is in good agreement with the experimental result. The following sources are believed to contribute to the residual error:

1. The calculation errors of the pressure distributing by FEA

2. The measurement error of the TIF
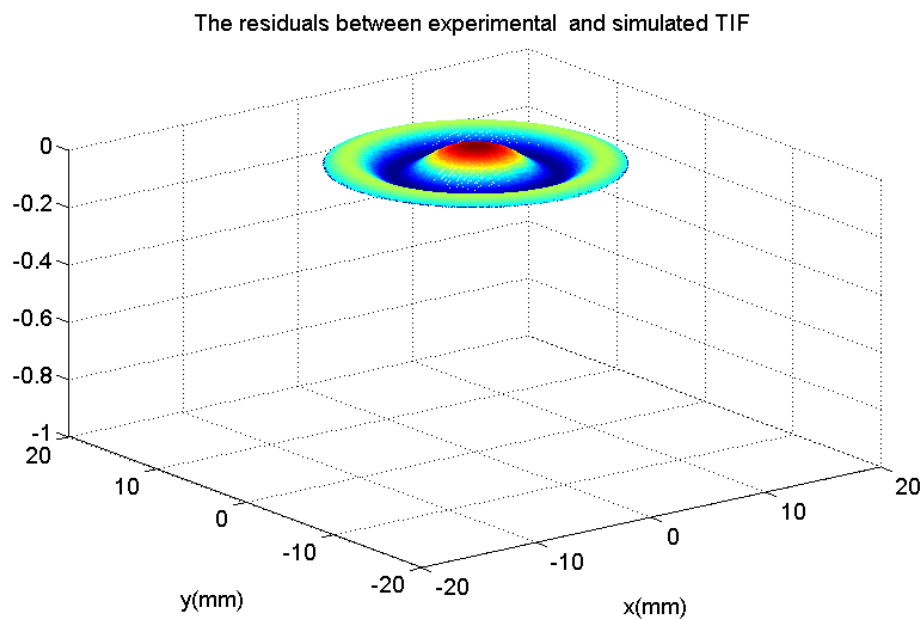
Figure 4.16 The residuals between normalised experimental and simulated TIF (author's data)
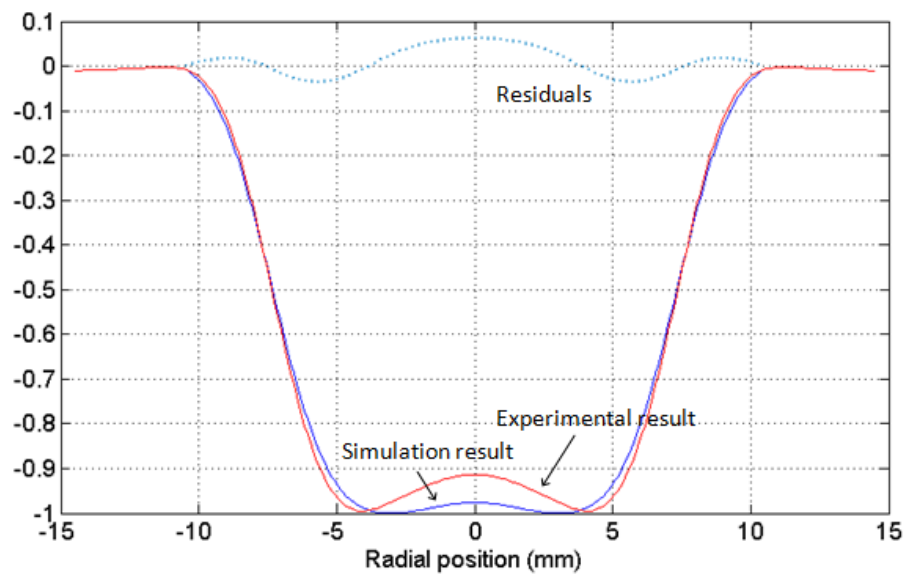
Figure 4.17 The comparison of normalised 2D experimental and simulated TIF (author's data)

4.7 Summary

According to the Preston equation, to establish a model of material removal for '*Precessions*'
polishing, the relative velocity distribution and the pressure distribution are required. In this
chapter, the velocity distribution is obtained based on the geometry of the precess motion. By
means of finite element analysis (FEA), the pressure distribution over the polishing spot has
been calculated. The FEA result is verified by experimental force measurement. Therefore, a
model that can predict the shape of the TIF for a given tool and condition has been established.
The demonstration of simulation (R80mm tool, 0.7mm Z-offset, 15° precess angle) shows a
good agreement with the experimental result. The next chapter will present the edge control
techniques.

Chapter 5

Edge control for the fabrication of segment: modelling and experiment

This chapter starts with an analysis of the edge effects under 'bonnet' tool polishing. Three edge control methodologies are presented: 1) The traditional 'wasters'; 2) The 'Nodding' technique; 3) The 'Tool lift'.

The 'Wasters' method is described in the outline and the reason is given for not pursuing it further. To demonstrate the feasibility of the 'Nodding' technique, the stability of tool influence functions (TIFs) has been investigated and a preliminary trial has been conducted. For 'Tool lift', the 3D TIFs at the edge are achieved by an integrated method in which the data from both a 3D Interferometer and a 2D Profilometer are stitched together. Based on these 3D TIFs at the edge, a model that can accurately predict the edge profile has been developed. The 'Tool lift' technique has been demonstrated with some preliminary success. The comparison of the three edge control techniques is also summarised in this chapter.

5.1 Introduction

The edge effect significantly dominates the performance of segmented-mirror telescopes. This is because the total length of the edge of these segmented optical systems is much longer than those of the conventional system with one mirror. For example, there is nearly 4000m of total length of edge in the E-ELT's primary mirror. These edges are distributed across the whole

pupil. As mentioned in **Section 1.5**, edge-roll degrades the stray-light and IR-emissivity performance. These are key parameters for the key science objectives, such as the detection of extra-solar terrestrial planets.

The edge figuring process is particularly challenging in the fabrication of a segmented mirror. The traditional technique pioneered by Keck is to oversize the segment during the polishing process. When the surface meets the specification, the segment is cut to a hexagonal shape. However, this introduces a risk process step and distorts the surface, requiring ion figuring which is slow (Ruch, 2011).

To obtain a satisfactory profile at the edge, many edge-control attempts were carried out and several techniques are demonstrated in recent research (Guo et al.*,* 2006; Kim et al.*,* 2009; Hu et al.*,* 2011). It was reported that a small-size tool could be used to process the edge area in MRF (Magneto Rheological Finishing) (Hu et al.*,* 2011). However, the processing time is unrealistic for large segments. In 2009, Kim et al. established a parametric modelling of edge effects based on the 'Preston equation' (Kim et al.*,* 2009). However, the cause of the edge effect in 'bonnet' polishing is different because of the distinct of the removal mechanism.

5.2 The edge effects under bonnet tool polishing

The amount of material removal according to the Preston equation (as described in **Section 2.3**) is based on the assumption that the contact spot is fully inside the part (Preston, 1927). When the spot extends beyond the edge of the part, the constant pressure between the tool and the part no longer exists. Wagner and Shannon, (1974), used the force equation in conjunction with the torque equation for static equilibrium. This model, however, presents an important problem. Whenever the tool centre is near the edge of the part, the minimum pressure can become negative, which means that this model is no longer valid. Jones, (1986), suggested a

linear pressure distribution model in 1986. Cordero-Davila et al, (2004), developed this approach further using a non-linear high pressure distribution near the edge of the part; however, they did not report the model's validity by experimental results (Cordero-Davila et al., 2004).

With the inflated bonnet tool, the pressure on the part is provided by internal air pressure and elastic deformation of the bonnet tool. For an elastomeric bonnet (solid rubber tool), the properties are similar to an inflated tool. When such a flexible tool overhangs the edge of the part, the pressure distribution at the edge is complex. **Figure 5.1** shows a sketch of the pressure distribution between the bonnet and the part. On the right is the pressure distribution at the edge of the part. It can be seen that the pressure on the edge becomes extremely high.
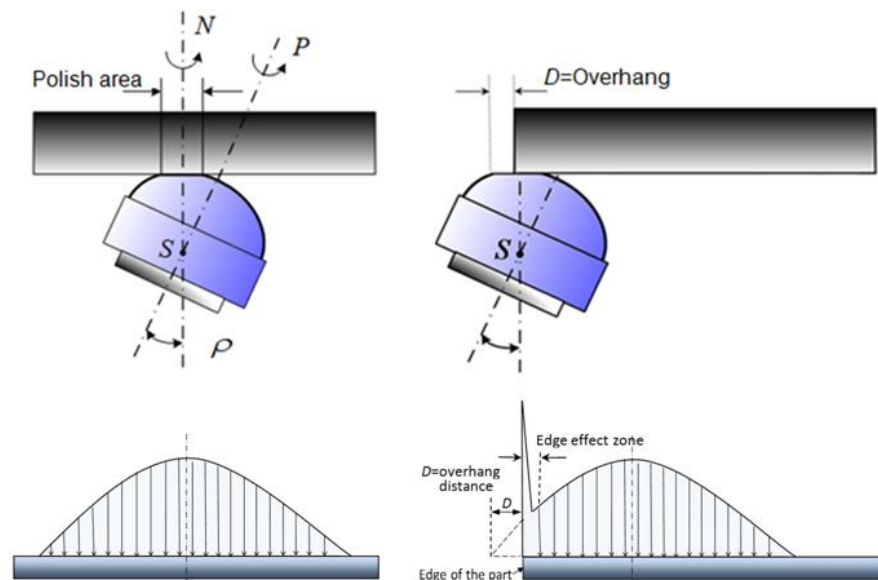
Figure 5.1 A conceptual sketch of the pressure distribution between the bonnet and the part. On the left is the pressure distribution inside the part, on the right is the pressure distribution at the edge of the part (drawn by the author)

In general, edge effects under 'bonnet' tool polishing are caused by the following (Walker, 2012A):

1. When the spot overlaps an edge, the area in contact decreases, thus the pressure increases (for constant force). This causes the edge zone turndown.

2. The membrane of the 'bonnet' tool wraps around the edge of the part, which turns the edge zone down.

3. When the spot falls short of leaving the part completely, a zone near the edge of the part undergoes less polishing than on the bulk area of the part, which turns the edge zone up.

4. The rotating tools give a bow-wave of slurry when the tool 'attacks' the edge of the part. This turns the edge down.

There is interplay between these, but they cannot be made to compensate. If the extreme edge of a segment is rolled-down at any process stage, the entire surface must be re-worked to rectify it. **Figure 5.2** shows that the edge is rolled-down when the bonnet overhangs the edge of the part. In order to avoid this time-consuming process, three edge control techniques are presented in this chapter.
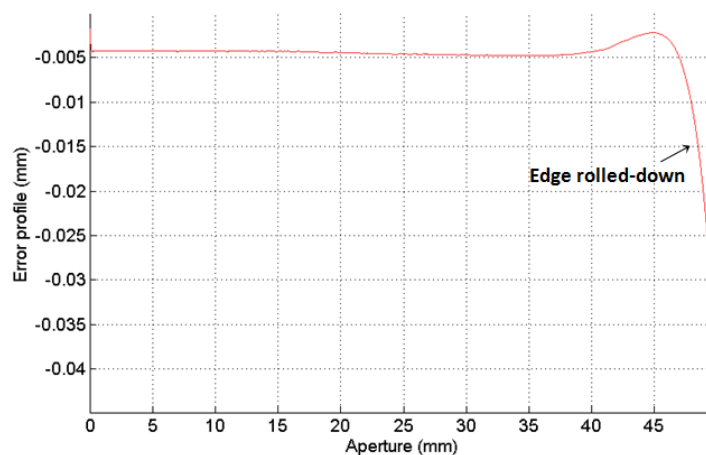
Figure 5.2 The edge profile when the bonnet projects beyond the edge of the part (author's data)

5.3 Traditional 'Waster' pieces on the edge

In traditional lapping, 'Wasters' around the edges of a part are used to overcome the increase in applied pressure as the tool overhangs the edge. After the prescription of the surface of the part has been achieved, the 'Waster' pieces are then detached. Thus, edge roll of the part can be avoided.

In the case of '*Precessions*' polishing, a waster can provide a surface to support the overhanging part of the polishing membrane. Therefore, the wrapping of the membrane around the edge of the part can be avoided, giving a constant angle of attack (Walker et al., 2008), as shown in **Figure 5.3**. The ideal waster material is the same as the part, as the polishing condition and thermal expansion will be identical.
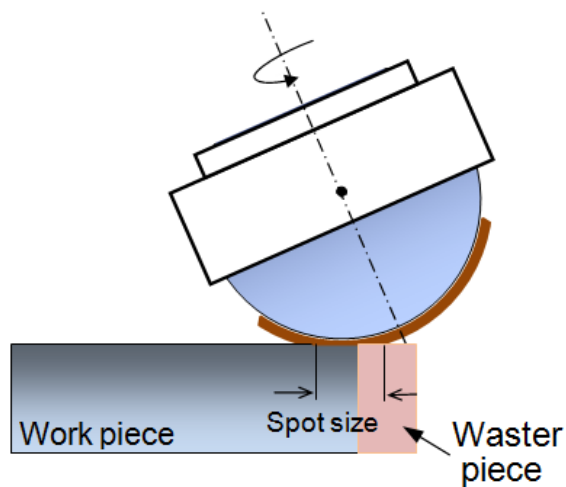
Figure 5.3 The schematic diagram of 'Waster' pieces for edge control (drawn by the author)

Traditionally, 'Wasters' are a very effective edge control approach for small parts. Unfortunately, the author has been unable to find any publication in which the 'Waster' edge control approach has been used in the manufacture of large segments. It is believed that the risks of the approach on large segments are (Walker, 2012C):

1. The issue of waster-adhesives 'pulling' surfaces, that lead to form-distortion on large parts and subsequent form rectification would be required

2. Risk of damage to the edges on detaching the wasters

3. Accidental detachment: if a waster became detached under polishing forces, it could have disastrous consequences

4. Risk of damage in cleaning adhesive from edges after waster-detachment

5. Handling risk: There are nearly 6000 pieces of glass (for 931 hexagonal segments) to be machined, installed and handled in production. An effective waster should accommodate the largest spot (for example, R160mm bonnet/60mm spot) and will weigh approximately 5Kg. This would be difficult to handle manually and would need an automated positioning method.

With the above points taken into account, the 'Wasters' method has been retained as a possible backup solution. The direct processing of the edges without wasters is preferred. Two active edge control techniques are presented in the following section.

5.4 'Nodding' technique for edge control

5.4.1 Methodology of 'Nodding' technique

When the bonnet goes beyond the edge of the part there will be excessive material removal. To avoid this, a 'Nodding' technique is proposed for edge control. This technique requires two conditions:

1. A polishing cloth with a truncated edge, which is able to deliver a tool influence function with a sharp edge. The sharp edge comes into contact with the edge of the part without encroachment.

2. The 'nodding' motion in the edge zone is to maintain the truncated edges of the 'Nodding' tool influence functions, which are always tangential to the edge of the part under polishing, as shown in **Figure 5.4**.

The 'Nodding' motion is controlled by the precess angle continuously changing in the 'Nodding zone'. In this way, the influence function never extends past the edge of the part. This is effectively achieved by starting at the edge with the largest precess angle and decreasing it as the tool is moved away from the edge zone ('Nodding' zone). When the tool goes into the bulk area of the part, the precess angle is maintained constant until the next edge zone is encountered. This strategy can potentially enhance processing of the edges and save processing time on the segments.
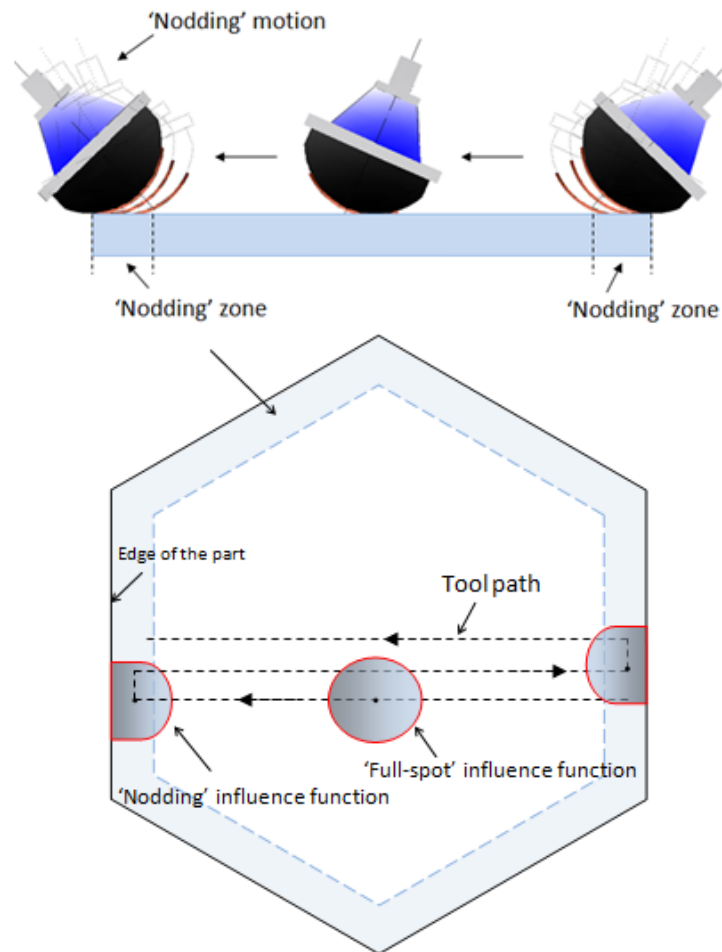
Figure 5.4 The sketch of the 'Nodding' technique for edge control (drawn by the author)

5.4.2 'Nodding' tool and influence functions

1 Preparing the 'Nodding' tool

The 'bonnet' tools are characterised as Rx, where x=radius of curvature in mm. The 'Nodding' tool can be prepared from an R160mm (or R80mm) bonnet by trimming the cloth using a single-point cutting tool. **Figure 5.5** shows the preparation of R160mm 'Nodding' tool. A 3.2mm thick polyurethane polishing cloth is placed on the R160mm bonnet. It has been found that the maximum Z-offset of 1.6mm can be adopted, which gives a spot size of 45mm. The cloth is trimmed to allow a maximum nodding angle of 20.5° for this bonnet.
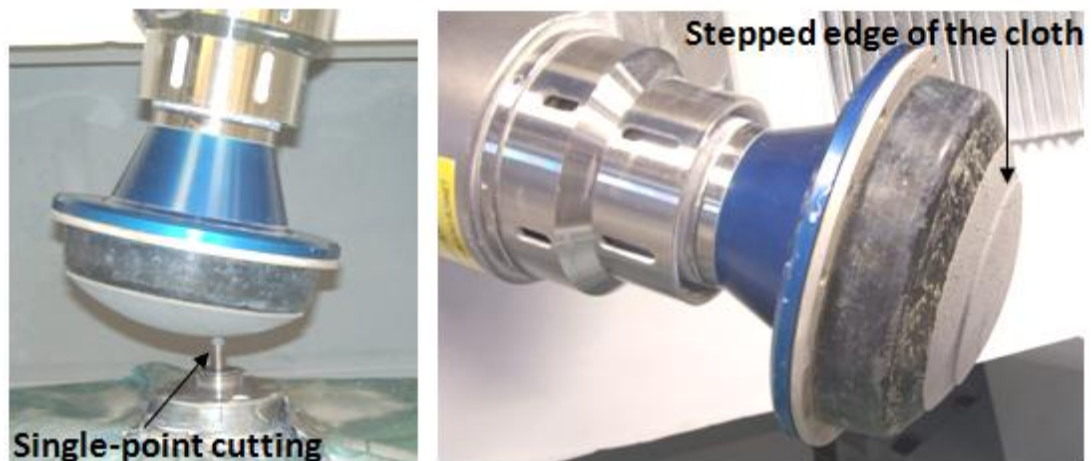
Figure 5.5 Preparation of R160mm 'Nodding' tool (picture by the author, May 2009)

2 Generation of 'Nodding' tool influence functions

The 'Nodding' tool influence functions were generated on a 150mmx150mm square, Zerodur part and measured on a 3D Form Talysurf. The measurement is shown in **Figure 5.6**. For these influence functions, a dwell time of 120 seconds and 0.5mm Z-offset were used. The precess angle is varied between 14° and 20.5^{o}.

From the measurement of the tool influence functions (TIFs), it can be seen that there are two significant and distinctive features between these TIFs with the increase of the precess angle, they are:

1 The edge of the TIFs becomes sharper and straighter

2 The depth of the edge of TIFs becomes deeper

The TIFs with sharp and straight edges are beneficial for edge control. However, the different material removal of TIFs can cause a non-uniform material removal in the edge zone. To avoid this, the parameters (dwell time and Z-offset) in the edge zone need to be optimised to achieve a uniform edge profile.
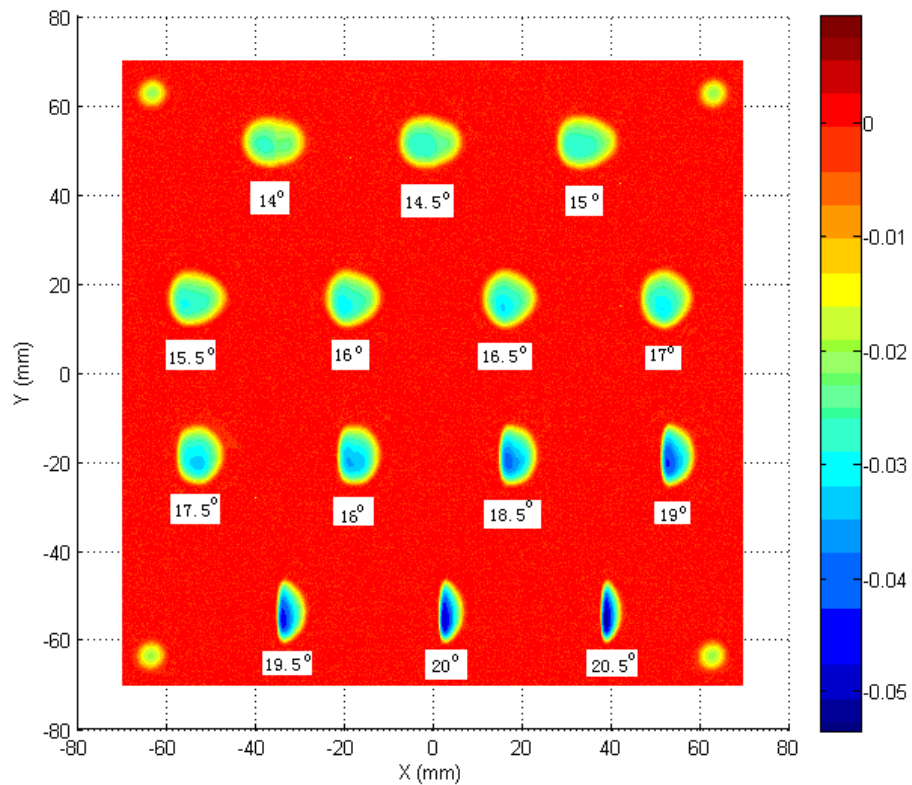
Figure 5.6 The 'Nodding' influence functions with different precess angle, R160mm bonnet, 0.5mm Z-offset, 120 seconds dwell time(Z scale in mm) (author's data)

5.4.3 Stability test of tool influence functions

The danger of any active edge method is the potential for overshoot: turning an edge down. Hence, the stability of the tool influence functions is critical. The aim of this experiment was to test the durability of the edge of the cloth during polishing. This can be implemented by testing the stability of the tool influence functions (TIFs). This experiment was carried out on a 200mm cross corners, hexagonal BK7 glass part. An R160mm bonnet was used. Tool Z-offset was 0.5mm and precess angle was 17.5° where the edge of the cloth passes through the centre of the spot. The head speed was 800rpm. There were altogether 10 TIFs generated. They were placed into two rows and numbered as seen in **Figure 5.7**. TIF1 was generated just after the

cloth had been dressed. From TIF2 to 5, each TIF was generated after the cloth had been worn

in for 10minutes. From TIF6 to 10, the cloth was worn in for 30 minutes prior to making the TIF.

The precess angle was set to be 17.5° all the time. The slurry's specific gravity was measured to

be 1.016 during this experiment.
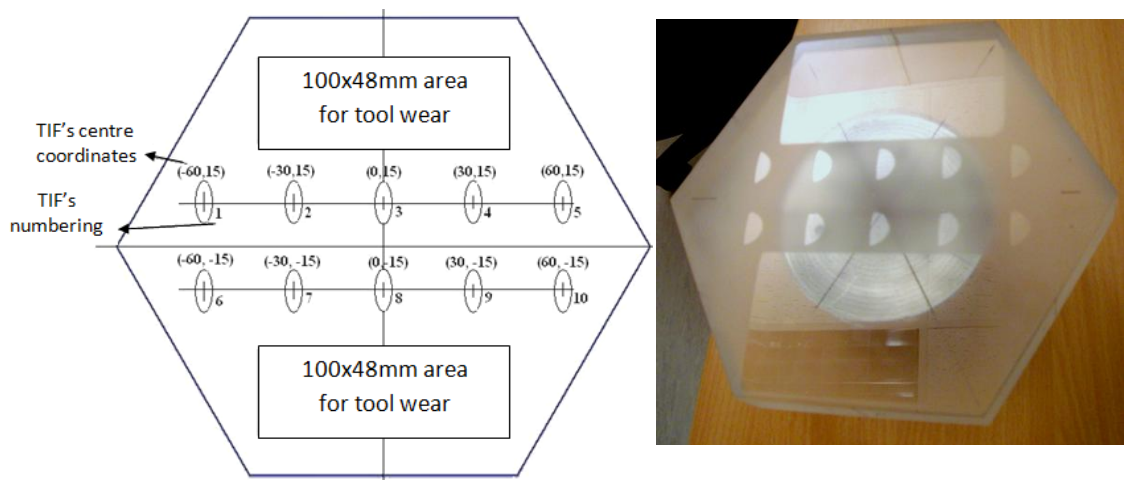
Figure 5.7 The position of the 'Nodding' TIFs on the glass (picture by the author, 2009)

The 3D and 2D TIFs were measured on the Form TalySurf PGI 1240. The results are shown in

Figure 5.8 and **Figure 5.9**. The volume of each TIF is listed in **Table 5.1**. It can be seen that

there is a significant change in size, shape and removal volume between TIF1 to the others.

From TIF2 to TIF10, it evolves slightly. This can be associated to cloth wear. After 106 minutes,

the removal rate becomes stable.
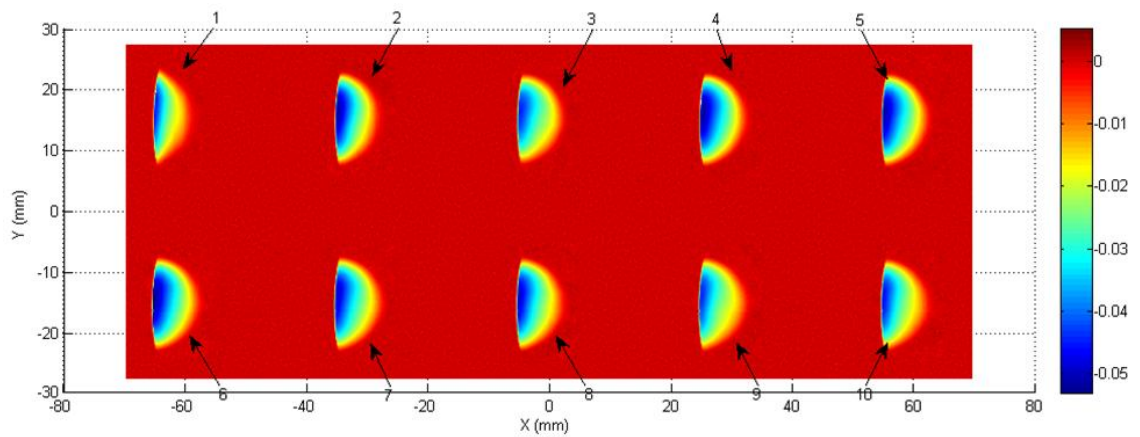
Figure 5.8 The measurement of TIFs on 3D Talysurf for stability testing. R160mm bonnet, precess angle 17.50, Z-offset 0.5mm, dwell time 60seconds, Z scale in mm (author's data, 2009)
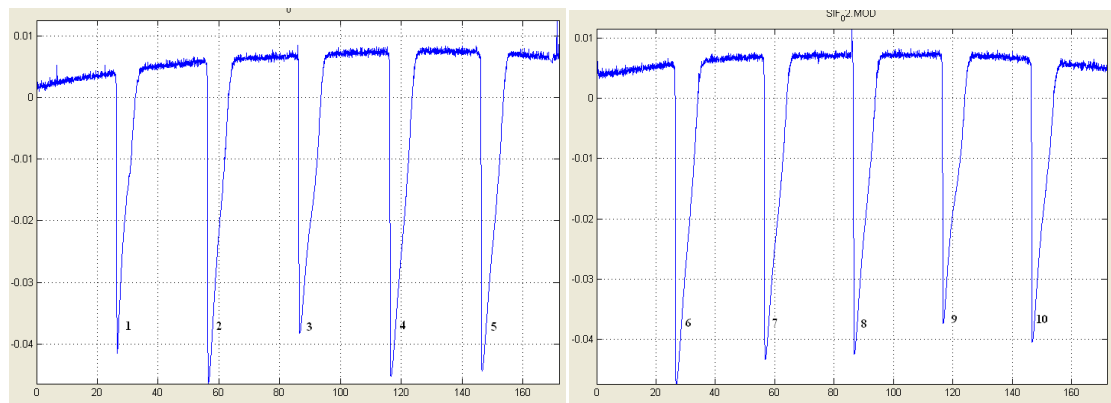
Figure 5.9 The measurement of TIFs on 2D Talysurf, scale in mm (author's data, 2009)

Table 5.1 The volume of each influence function (author's data, 2009)

TIF's numbers	1	2	3	4	5	6	7	8	9	10
Wear time(minutes)	0	11	22	33	44	75	106	137	168	199
Volume (mm^3)	1.5	2.1	2.0	2.4	2.4	2.5	2.1	2.0	2.0	2.0

5.4.4 Experimental demonstration

The 'nodding' bonnet method for edge control on the hexagonal part relies on two aspects. First, a set of TIFs in the edge zone requires stability and accuracy including both removal rate and shape. Second, a nodding motion is required such that the truncated edge of the influence function is tangential to the edge of the part under polishing. A great effort in generating this tool path that fulfils this nodding motion was made by Christina Dunn in October 2009, as shown in **Figure 5.10**. By this tool path, a preliminary experiment was conducted on a hexagonal flat BK7 part.
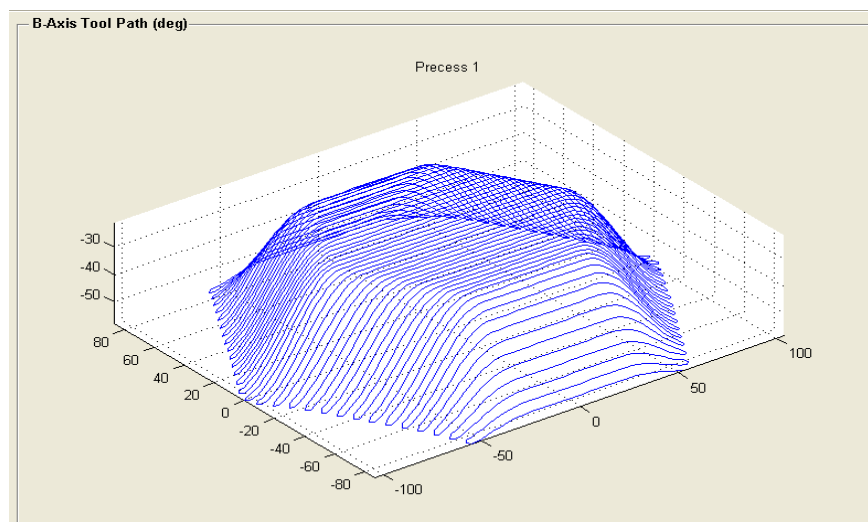
Figure 5.10 The precession angle for 'Nodding' motion, B-Axis tool path (in degree) (Dr. Dunn, 2009)
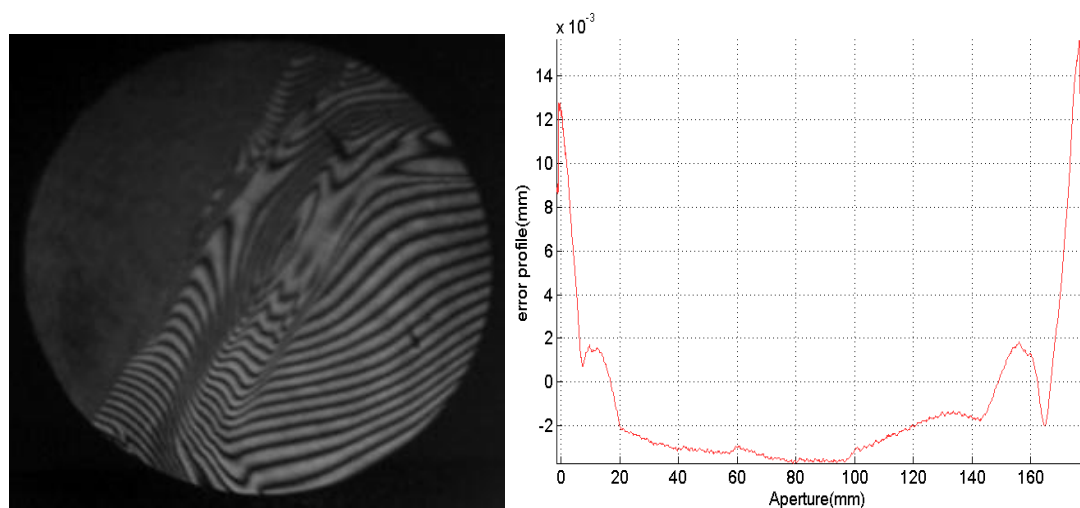
Figure 5.11 The interferogram of the edge and Form-Talysurf measurement (author's data, 2009)

The interferogram of the edge and Talysurf scanning (edge to edge) is shown in **Figure 5.11.** It can be seen that a feature is left on the surface throughout the 'Nodding' zone. However, there is no edge turn-down. This demonstrates that the process is fundamentally sound. The up-standing edge is about 7mm wide. This can be flattened by a pitch polishing process. **Figure 5.12** is the interferogram of the edge after 'Nodding' polishing and pitch polishing. The details about the pitch polishing process will be introduced in **Chapter 7**.
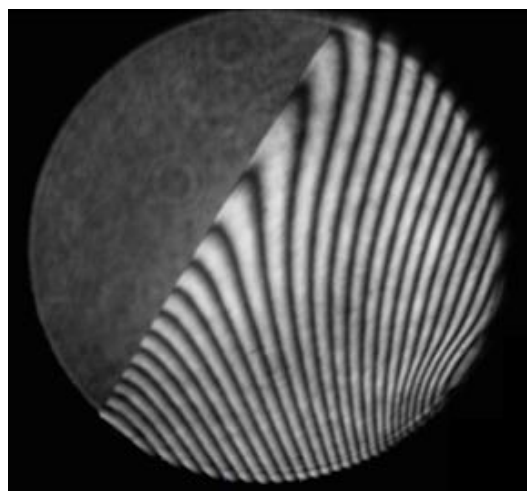
Figure 5.12 The interferogram of the edge after 'Nodding' polishing and pitch polishing process (author's data, 2009)

5.4.5 Summary for 'Nodding' technique

A methodology for edge control has been described in this section in which influence functions with a sharp edge are acquired in the edge zone to avoid the edge roll-down using a 'Nodding' motion. This technique can potentially save time on processing the segments. To demonstrate the feasibility of the 'Nodding' technique, the stability of the tool influence functions was investigated and a preliminary trial was conducted. Narrow (about 7mm wide) and up-standing edges were achieved. The preliminary result shows that this technique is fundamentally sound for edge control. However, to achieve a uniform material removal within the edge zone, the parameters (dwell time and Z-offset) need to be optimised, and accurate influence functions (position and removal rate) are required. Generating a tool path to perform the 'Nodding' motion is also an issue upon which more research is required.

5.5 'Tool lift' technique for edge control

5.5.1 Methodology of the 'Tool lift' technique

Tool lift is the ability to control bonnet spot-size during polishing. The strategy of the 'Tool lift' approach is that comparatively large polishing spots are applied over the bulk surface to give high volumetric removal rates in pre-polishing and form-correction polishing. Tool lift is applied within the edge-zone to leave broad upstanding edges, as shown in **Figure 5.13**. A range of smaller spot-sizes then encroach on the up-stand and progressively reduce its size and width. The lower volumetric removal rates of smaller spots also enhance the sensitivity of the process converging on the final form.
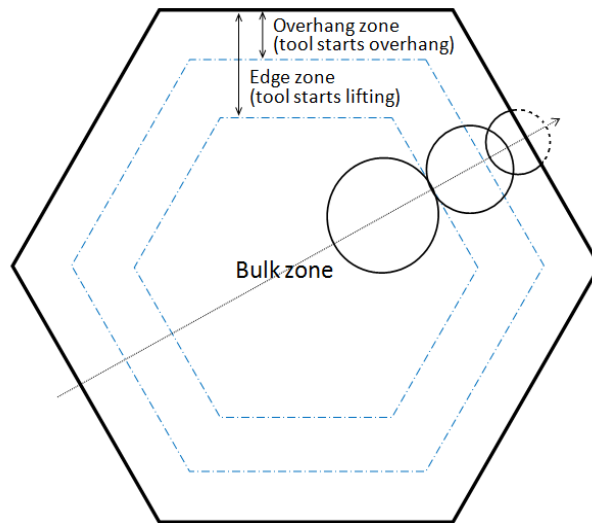
Figure 5.13 The sketch of the tool lift process for edge control (drawn by the author)

Smaller spots are deployed to correct the edge zone, following a roughly Nyquist approach. The Nyquist theorem states that the sampling frequency should be equal to or greater than double the signal frequency to be detected (Deng, 1997). Here it means that the spot size of the tool must be less than half of the bandwidth of the surface error in order to remove a certain frequency feature.

The principle of this approach is that the whole surface always needs to be within the measurement-range of the interferometer. The tool-path is programmed to perform the tool lift. This also conveniently provides a controllable way to manage the local slopes within the dynamic range of the full-aperture interferometer.

5.5.2 Material-removal modelling and experiment

5.5.2.1 The need for material-removal modelling

To maintain a gradual edge, so that the whole surface can be within the measurement-range of the interferometer, the process parameters need to be optimised. The multiple degrees of

freedom (Z-offset, overhang, precess angle, feed-rate, spacing) mean that an unrealistic machine-time would be needed if it is not helped by prediction. The aim of the modelling is to predict the edge profile. The model accepts input data, a family of TIFs within the edge zone.

In this model, the surface is divided into the bulk zone and the edge zone as shown in **Figure 5.13**. A large spot size (e.g. 60mm) is adopted for the bulk zone. When the tool moves into the edge zone, a family of smaller spots is achieved because of tool lift. Therefore, three sets of TIFs are required to predict the removal within edge-zone:

1. The bulk's TIF

2. The TIFs with different Z-offset

3. The TIFs with different overhang

To support modelling of the material-removal, the generation of these TIFs is introduced in the following section.

5.5.2.2 Generation of TIFs with different Z-offsets

When the bonnet moves into the edge zone, a family of different spots is achieved through tool lift. Therefore, the TIFs with different Z-offset values are needed for the material removal modelling. To capture a complete sampling with different Z offsets, interpolation from a more limited sampling of empirical TIFs' data was deployed.

The experiment was performed to generate the TIFs with different Z-offsets. The conditions of this experiment were: 160mm bonnet tool with LP66 polyurethane polishing cloth, Precess angle 15°, Zerodur glass, Dwell time 10 seconds, H-axis speed 800 rpm and Slurry density 1.025. A series of TIFs with Z-offsets of 0.1mm, 0.3mm, 0.5mm up to 2.8mm were chosen. The measurement results are shown in **Figure 5.14**. From these measurements, the TIFs with Z-offsets ranging from 0.2mm up to 2.6mm are extrapolated using MatLab code. The extrapolated results are shown in **Figure 5.15**.
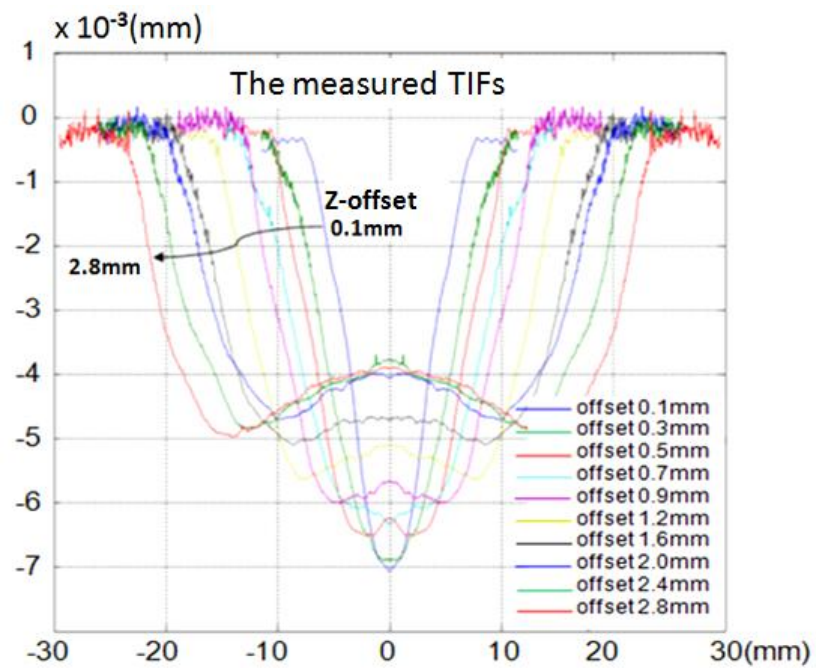
Figure 5.14 Experimental measurements of TIFs with different Z-offsets (author's data)
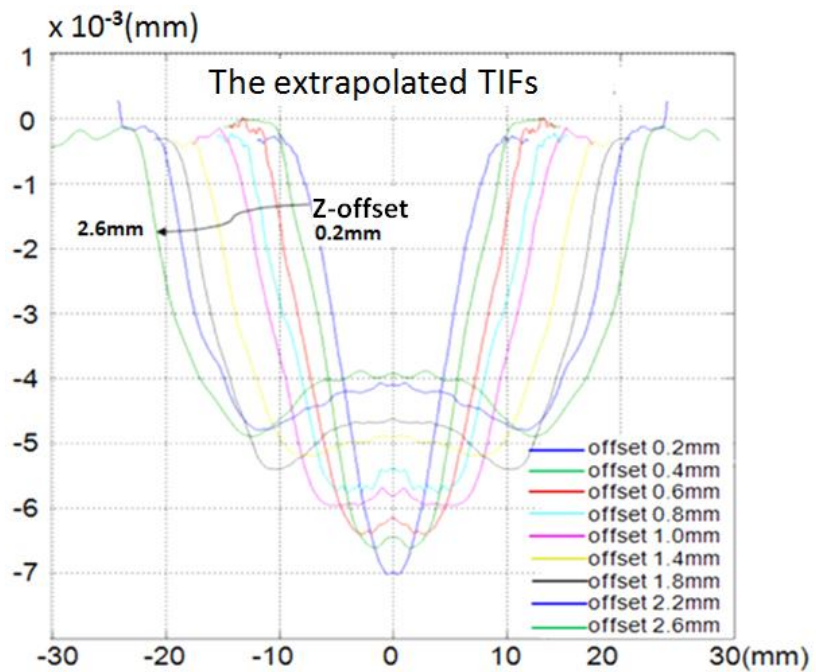
Figure 5.15 Extrapolated TIFs with different Z-offsets (author's data)

5.5.2.3 Stitching of TIFs in the edge zone

When the spot projects beyond the edge of the part, the bonnet material at some level wraps around the edge. The local edge-removal of the TIF then becomes abnormally high. If not managed, this will turn the edge down. Moreover, the resulting slopes can be beyond the measurement-range of full-aperture interferometry. From recent research, a swing arm profilometer has been developed for the measurement of tool influence function (Jing et al., 2010). However, it can only measure those TIFs on a circular-shaped surface.

To obtain the full data of the TIFs at the edge of the part, a simplified measurement method has therefore been developed using both 3D interferometer and 2D Profilometer data. The schematic diagram of this method is shown in **Figure 5.16**. Firstly, the depth of an edge was measured by individual 2D scanning. A line of the boundary of the TIF was then interpolated, as shown in **Figure 5.16 (a).** After the boundary of the TIF is obtained, the 3D of the TIF at the edge of the part is then interpolated, shown in **Figure 5.16 (b)**.

(a)

(b)
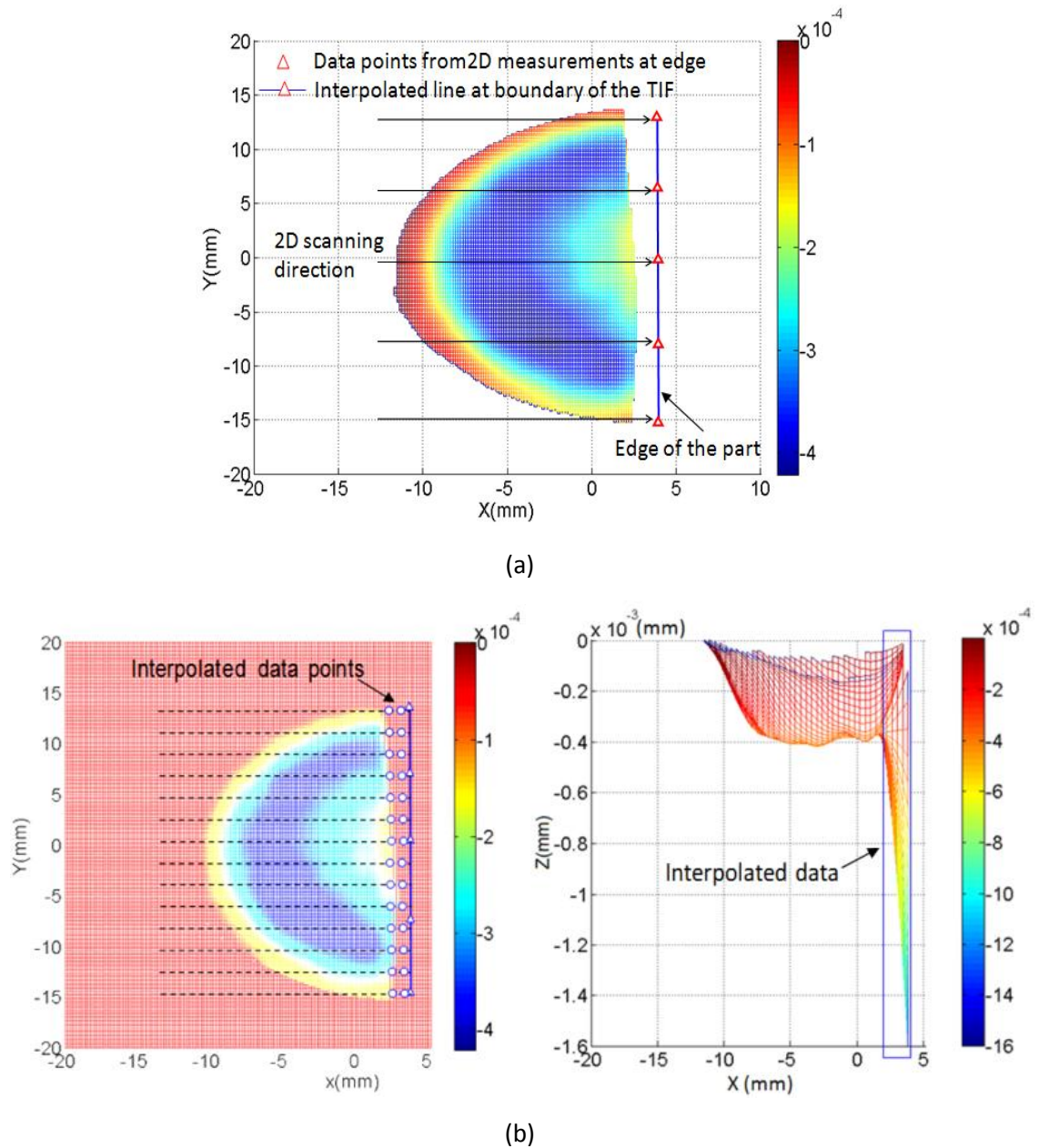
Figure 5.16 The schematic diagram of interpolating 3D TIF at the edge, where (a) 2D scanning and interpolating boundary of TIF (b) Interpolating of 3D in the vicinity of edge of TIF (author's data, January 2011)

The stitched results of TIFs at the edge of the part are shown in the **Figure 5.17**. It can be seen that approximately 2mm of the edge data is lost in the interferometer field, which is recovered with the profilometer. The result obtained in this section is used to verify the removal modelling results in the following section.
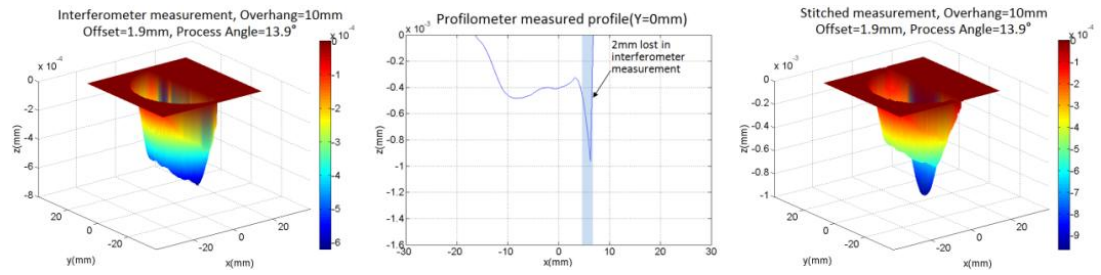
(a) Z-offset=1.5mm, Overhang=10mm, Process Angle=13.9°
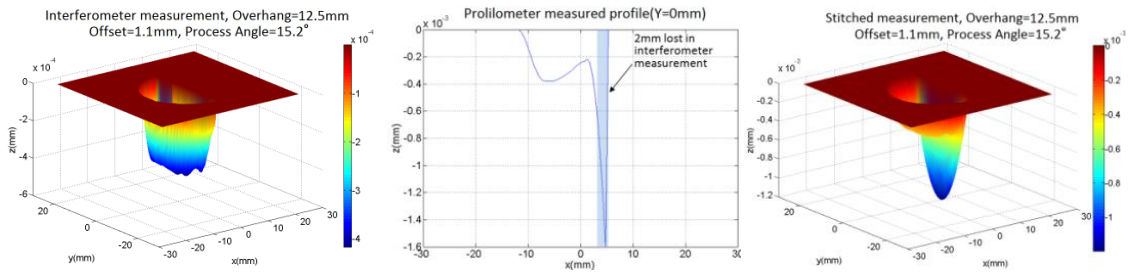
(b) Z-offset =1.1mm, Overhang=12.5mm, Process Angle=15.2°
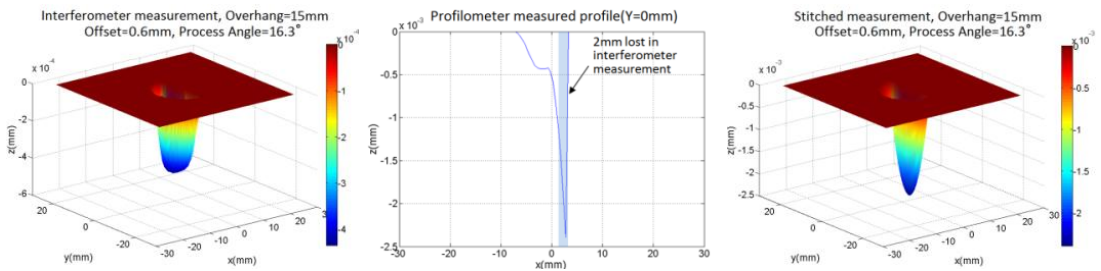
(c) Z-offset =0.6mm, Overhang=15mm, Process Angle=16.3°
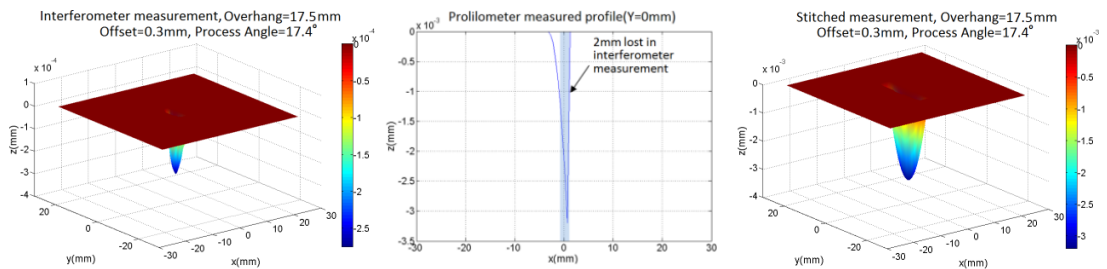
(d) Z-offset =0.3mm, Overhang=17.5mm, Process Angle=17.4°

Figure 5.17 The results of stitched 3D TIFs at the edge (author's data)

5.5.2.4 Material removal modelling and results

1 Superposition of material removal

As introduced in **Section 4.2**, the polishing tool influence function is defined as the average removal value $r(x, y)$ in unit time *T* at the point $q(x, y)$:

$$r(x, y) = \int_0^T k \cdot v(x, y) \cdot p(x, y) \cdot dt \qquad (5.1)$$

where, $v(x, y)$ - Instantaneous relative velocity at point $q(x, y)$;

$p(x, y)$ - Instantaneous pressure at point $q(x, y)$
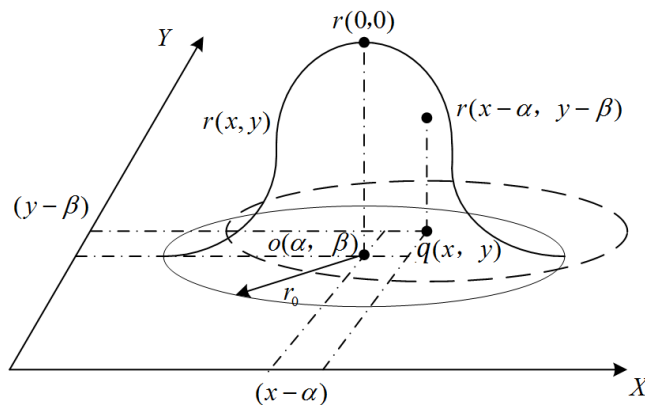
Figure 5.18 The sketch of the superposition of material removal (drawn by the author)

As shown in **Figure 5.18**, during the process, the tool dwells for a certain time $d(x, y)$ at each point. When the removal function is at point $o(\alpha, \beta)$, the removal function has different impacts on the circular domain which is centred at $o(\alpha, \beta)$, of radius r_0. When the polishing tool moves to the point $p(x, y)$ in accordance with the scheduled track, the removed material in each region will be superimposed. So the material removal can be related to the distribution function $h(x, y)$ by the following:

147

$$h(x, y) = \sum_{\alpha} \sum_{\beta} [d(\alpha, \beta) \cdot r(x - \alpha, y - \beta)] \delta\alpha\delta\beta \qquad (5.2)$$

Eq. 5.2 can be written as an integral formula because of the continuous movement of the bonnet tool:

$$h(x, y) = \int_{\alpha} \int_{\beta} d(\alpha, \beta) \cdot r(x - \alpha, y - \beta) d\alpha d\beta \qquad (5.3)$$

The integral formula shows that the removal distribution function $h(x, y)$ is equal to the 2-dimensional convolution between the polishing removal function $r(x, y)$ and the dwell time $d(x, y)$:

$$h(x, y) = r(x, y) ** d(x, y) \qquad (5.4)$$

This convolution operation can be performed using MatLab code if removal functions $r(x, y)$ and dwell time $d(x, y)$ are given. The verification of this modelling by experiment is introduced in the following section.

2 Verification of the modelling

A polishing experiment was carried out on a 200mm across-corners hexagonal part to verify this model. **Figure 5.19** presents the modelling result (purple curve) of a surface profile with significant features using multiple influence function data as generated in the previous section. The red curve is the experimental result with the same process parameters. As can be seen, the model shows good prospects for precisely predicting edge-features, except the asymmetry of the experimental profile. This has been investigated and resolved (see next chapter).

By this model, the parameters of tool lift have been optimized and an up-turn edge profile has been obtained. This is presented in the next section.
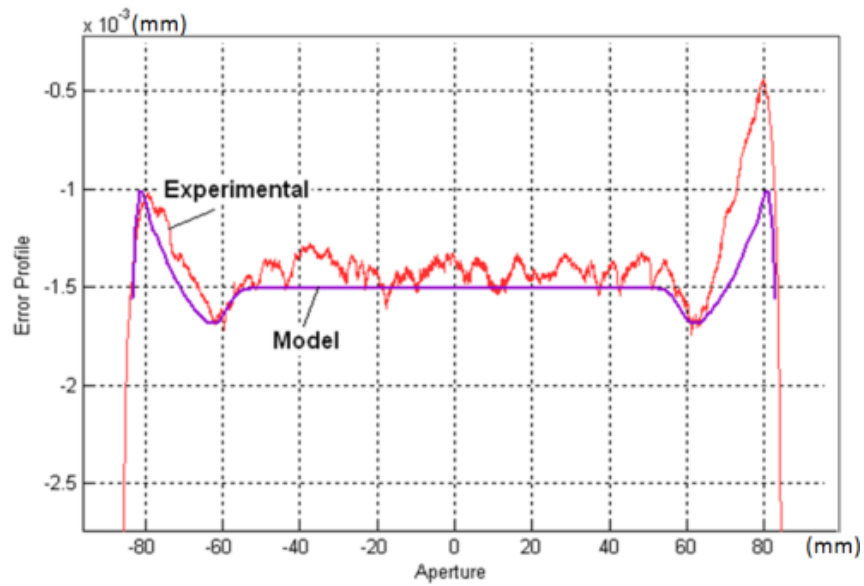
Figure 5.19 Comparison of modelling and experimental results (author's data)

5.5.3 Experimental demonstration

A 200mm across-corners Zerodur hexagonal part was prepared by loose-abrasive hand-lapping. It was then processed in five polishing runs on the IRP1200 machine, comprising three pre-polishing runs and four form-correction runs. The tool-lift parameters for each stage were optimised on separate samples to achieve up-turned edges, systematically within the measurement-range of the interferometer. This is introduced in detail in the following.

5.5.3.1 Measurement set-up

The 4D 6000™ simultaneous phase interferometer was used to measure the 3D error map, set up horizontally on the optical table, as shown on the left of **Figure 5.20**. To identify the true edge of the part, the 'Extended Range' Form Talysurf with a 300mm measurement range was used for 2D scanning. It is shown on the right of **Figure 5.20**.
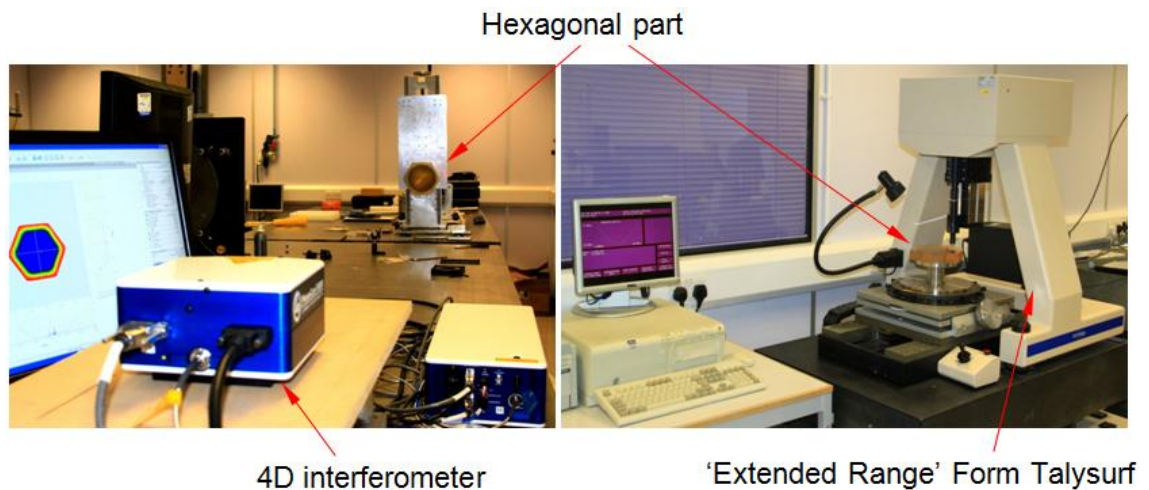
Figure 5.20 The measurement set-up, where on the left is the 4D interferometer, on the right is the 'Extended Range' Form Talysurf (picture by author, March 2011)

5.5.3.2 Pre-polish with R160/60mm spot

1 Parameters for pre-polishing

A R160mm inflated bonnet was used for pre-polishing. The polishing cloth was LP66 polyurethane. The 2.8mm Z-offset was chosen to deliver a 60mm full-diameter spot-size (60mm is the nominal spot-size; the measured spot-size was 51mm). As shown in **Figure 5.21**, due to the elasticity of the bonnet, the actual spot size was smaller than the nominal spot size. The 200mm across-corners Zerodur hexagonal part was rastered in three polishing runs, each orientated corner-to-corner in 120° steps. Each polishing run took 11 minutes, hence 33 minutes for the whole pre-polishing. The edge parameters for the pre-polish are shown in **Figure 5.22**.
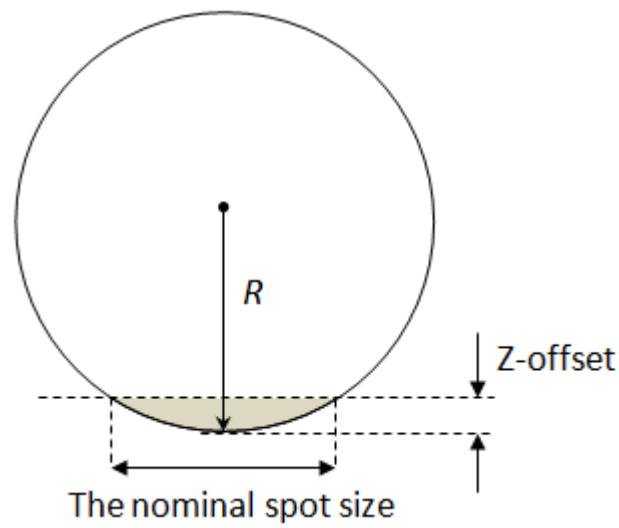
Figure 5.21 The nominal spot size and Z-offset (for R160mm bonnet and 2.8mm Z-offset, the nominal spot size is 60mm) (drawn by the author)
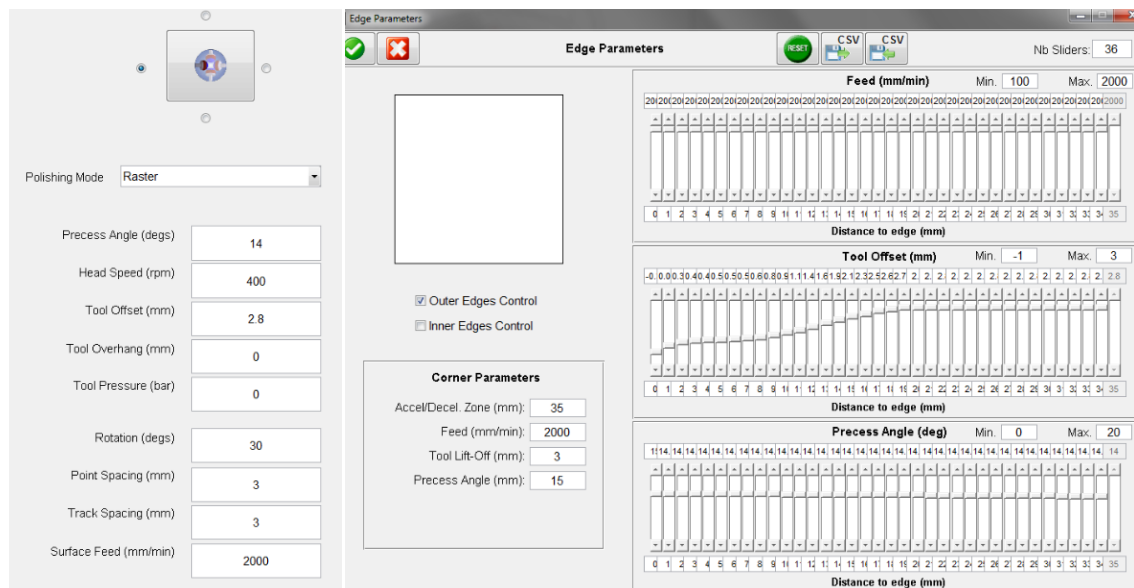
Figure 5.22 Edge parameters for pre-polishing (160mm bonnet) (author's data)

2 Pre-polish results

Figure 5.23 shows the results after pre-polishing. **Figure 5.23 (a)** and **Figure 5.23 (b)** are the interferogram and form error map with PV 3426nm and RMS 992nm for the whole surface. **Figure 5.23 (c)** is the 2D scanning from corner to corner and from edge to edge.

The mark in the centre of the part is a groove introduced with a diamond tool. This mark provides a datum to establish the absolute depths of removal using the Form Talysurf profilometer. By this means, it was established that approximately 8 μm depth of material was removed in processing this part. Note that the 'power' term has not been removed from the measurement, in order to keep a consistent edge height value. It can be seen that, after pre-polishing, upstanding edges with approximately 40mm width were achieved. This can be corrected by using a 20mm spot in the corrective polishing stage.
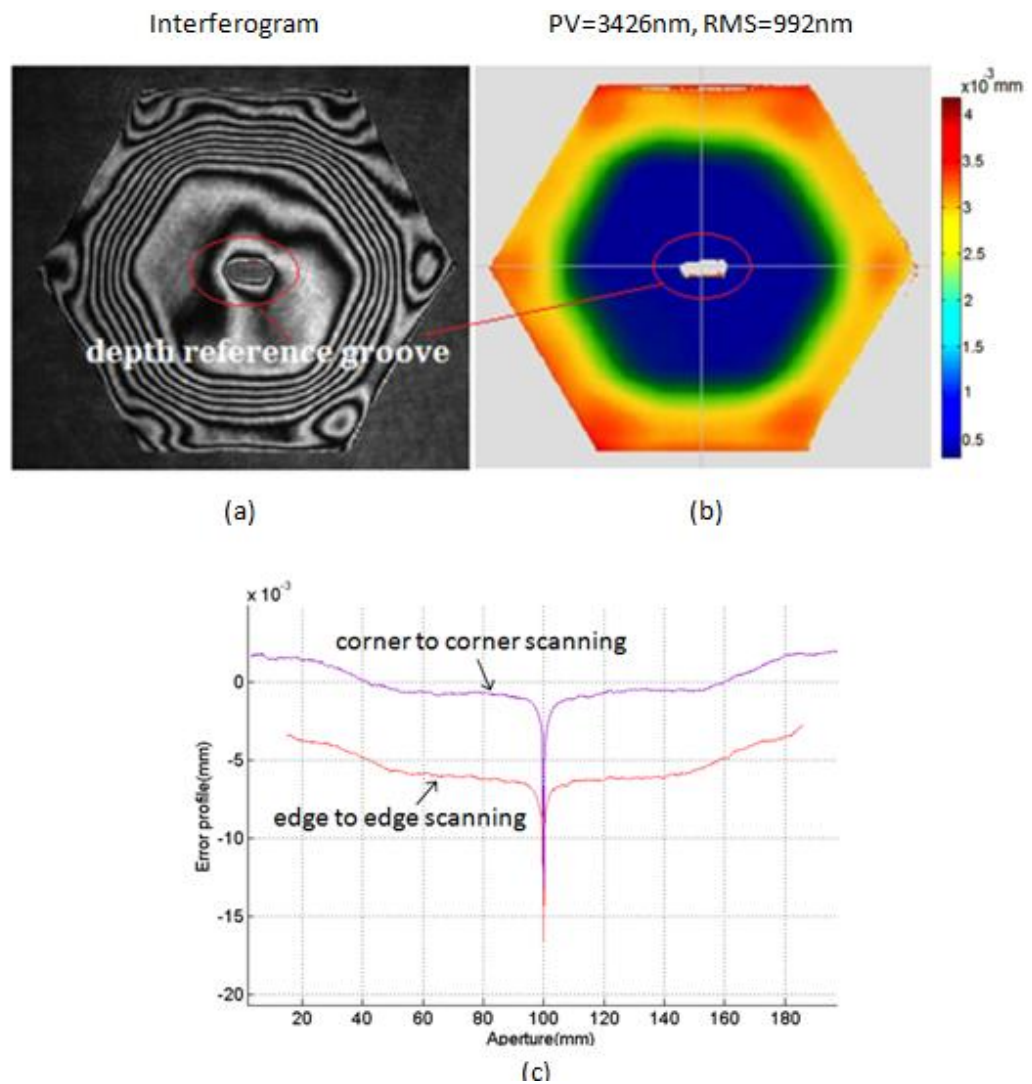
Figure 5.23 The measurements after pre-polishing, where (a) is the interferogram, (b) is the form error map, and (c) is 2D scanning (author's data)

5.5.3.3 Corrective polishing with R80/30mm, 20mm spots

1 Parameters for corrective polishing

An R80mm solid rubber tool with a 0.7mm Z-offset (21mm spot-size) and 1.4mm Z-offset (30mm spot-size) was used in the subsequent form-correction, where the bulk form was controlled at the level needed to establish the true form of the edges.

Each of the four passes constituted a single raster pass with a different precess position, as shown in **Figure 5.24**. The corrections 1, 2 (30mm spot) and 3, 4(21mm spot) are orthogonal. Each of the four correction runs takes about 20 minutes, thus, 80minutes for the whole form-correction. The parameters for form-correction are shown in **Figure 5.25**.
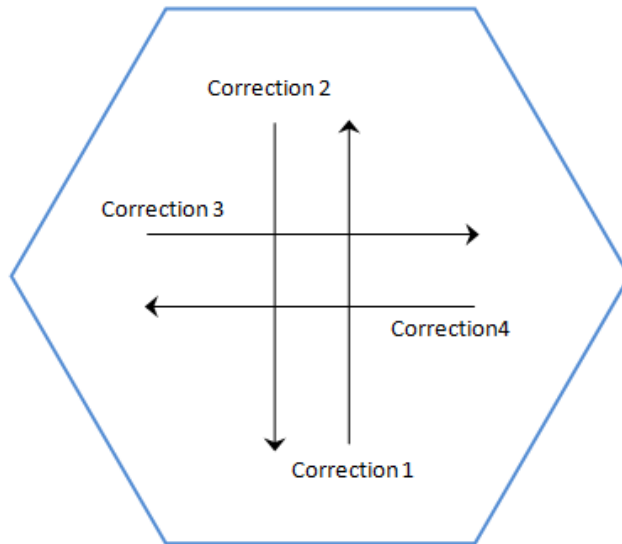
Figure 5.24 Direction of tool moving of correction runs (drawn by the author)
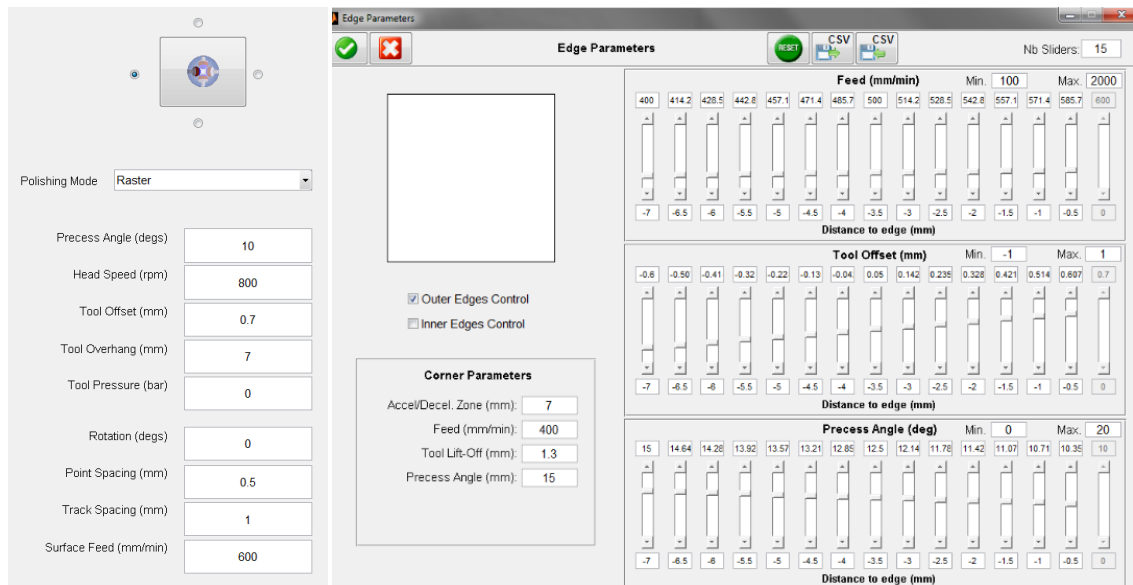
Figure 5.25 Edge parameters for corrective polishing (80mm bonnet) (author's data)

2 Results and analysis

The results in **Figure 5.26** show a form error of 479nm PV and 59nm RMS including the edge zone, after four form correction runs and a pitch tool process. The 'Pitch' process has been developed for surface mid-spatial smoothing and edge treatment (see **Chapter 7**).

Additional interferograms were acquired with masks placed on the surface of the part to identify the true location of the edge, as shown in **Figure 5.26** (b). It can be seen that, in this experiment, the bottom left edge **Figure 5.26** (d) has a narrow up-stand some 300nm high, with no down-turn whatever. The other edges have progressive down-turns, but in each case <1 mm width. This apparently occurs at the final stage using the smallest spot-size. In this experiment, the results show residual asymmetry in the process. This has been investigated and resolved, as reported in the next chapter.
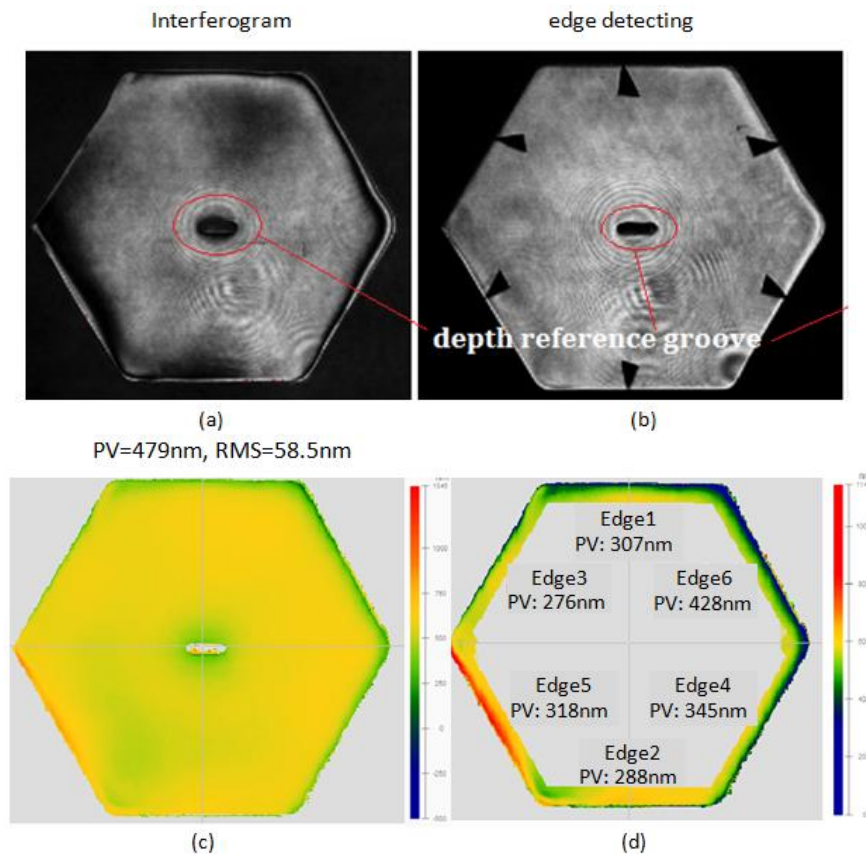
Figure 5.26 The measurements after 4 runs of form correction and smoothing process, where (a) is the interferogram, (b) is the edge detecting masks, (c) is the form error map, and (d) the edge results (author's data, April 2011)

5.5.4 Summary for 'Tool Lift' technique

A methodology of tool lift for edge control with inflated or elastomeric tools is described in this section. In this approach, the edge is left up-standing at every process-step, and a range of smaller spot-sizes encroach on the up-stand and progressively reduce its size and width. To optimise the parameters of tool lift, a numerical model was presented to predict the edge profile, based on empirical influence function data. A demonstration experiment was carried out on a 200mm across corner hexagonal part. The preliminary results show the potential of this process for edge control. The residual asymmetry in the process is investigated in the next chapter.

5.6 Comparison of the potential edge control methods

This chapter presents three edge control approaches: the 'Wasters', the 'Nodding' technique and the 'Tool lift'.

1. With the risks discussed in **Section 5.3**, the 'Wasters' method has been retained as a possible backup solution.

2. The 'Nodding' technique has the prospect of fine edge control with big bonnets and spots. However, there are two main problems that need to be addressed: one is the very high removal at the edge of the tool influence functions (TIFs), distorting the removal. This is believed to be due to the effect of the cross-ply reinforcements in the inflated bonnet membrane. It is likely that an elastomeric bonnet would be much better in this respect. Another problem is that the edge of the 'Nodding' tool influence function is curved, not straight, as shown in the **Figure 5.27**. From the experimental results in **Figure 5.6**, it can be seen that to achieve a straight edge in the 'Nodding' tool influence function, the precess angle needs to be increased (to 90°). This is diagrammed in the **Figure 5.28**. The current tools are limited to a precess angle of 25°. These two issues caused the 'Nodding' approach not to be selected for edge control in the process chain. However, the 'Nodding' approach is a potential technique for edge control of mass manufacturing of segments as big bonnets and spots could be used. 'Nodding' with elastomeric tools is promising approach to address the problems mentioned above.

3. With low risk and preliminary experimental success, the 'Tool Lift' strategy has been chosen for edge control in processing ESO prototype segments. The whole process chain is demonstrated in **Chapter 7**.
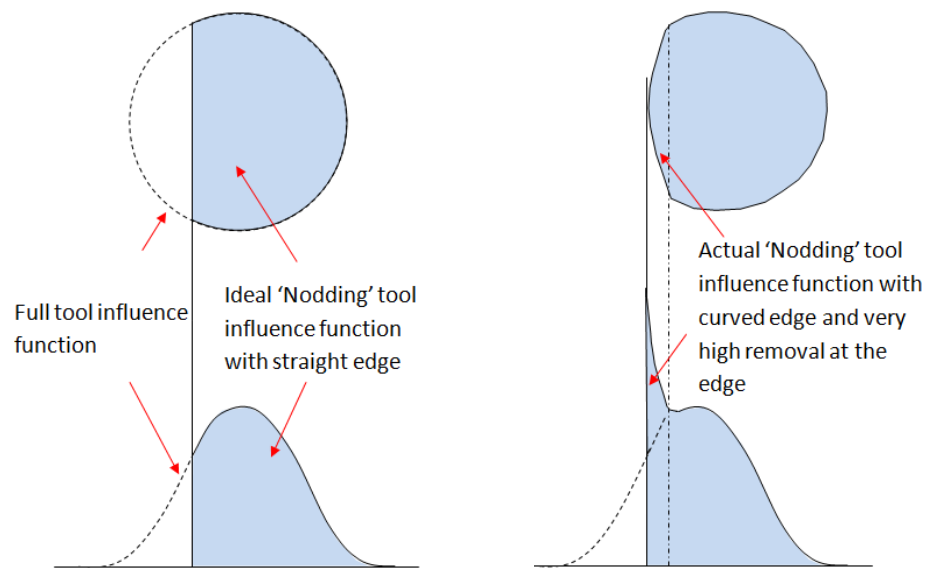
Figure 5.27 The schematic diagram of the ideal and actual 'Nodding' tool influence function (drawn by the author)
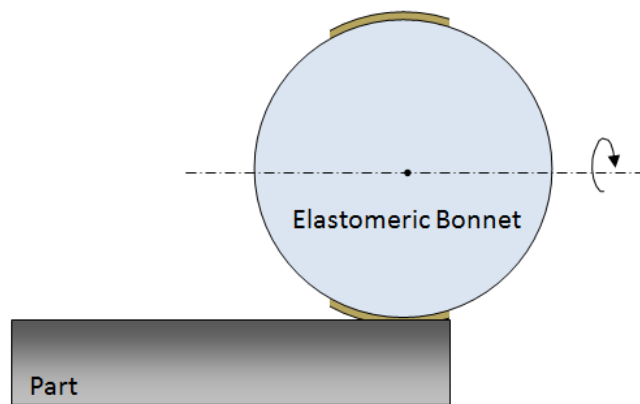
Figure 5.28 The schematic diagram of elastomeric bonnet with 90° process angle (drawn by the author)

Chapter 6

Diagnoses of edge asymmetry of a hexagonal part

Chapter 5 presented three methodologies of the edge control for polishing and form-correcting segments. With low risk, the 'Tool lift' technique demonstrated a preliminary success. In 'Tool lift', the edge is left up-standing at every process-step. However, the results showed an asymmetry on the hexagonal part at the final stage (some edges are rolled-down, as shown in **Figure 5.26**). The work in this chapter is to reveal the possible sources of edge asymmetry, including the machines, the tools and the part. The verification experiment is demonstrated in this chapter.

6.1 Investigation of edge asymmetry

A discussion with the Research & Development team was carried out to investigate the edge asymmetry. The analysis has gone through the whole process including the machine, the tools, the part and other conditions such as the slurry. The possible causes and proposed testing are listed in **Table 6.1**. The testing is introduced in the following section.

Table 6.1 Possible sources of edge asymmetry (Walker, 2011C)

	Possible cause	Proposed testing
1	Errors in the machine virtual pivot alignment shift effective spot positions	Check the virtual pivot of the machine
2	Error in bonnet radii entered into TPG	Test the real tool radii of curvature
3	The part is laterally offset or in rotation with respect to the CNC tool-path	Produce six tool influence functions (TIFs) inside of each edge. Measure the peak of each TIF with respect to each edge of the part. It should all be the same.
4	The blank is not a perfect hexagon, so different edges are treated differently	
5	The bevel is uneven, so that the optical surface is not a perfect hexagon	
6	Incorrect non-linear probing procedure (a procedure to probe the true tilt of the part by a program on machine) has tilted the part's surface with respect to the tool-path: the Z-offset and so spot size is different from one side to the opposite side	
7	The part moves in X,Y,Z,C or tip/tilt under the forces of a polishing run, due to inadequate fixturing	Measure the deflection with a dial gauge when a load equivalent to the expected polishing loads on the part is applied.
8	Legacy of asymmetry from the loose-abrasive grinding stage, which is retained through subsequent stages of processing. This may not be detected because of a relatively large amplitude	Measure the part at each stage with Form Talysurf.
9	Asymmetry introduced by either the pre- or corrective- polishing stages, due to the mismatch between the tool path directions on the hexagonal part as shown in **Figure 5.24**	Raster tool-path in six polishing runs from each corner of the hexagonal part, thus, the edges of hexagonal part are treated equally.
10	Other process variability such as slurry conditions	Measure the density before and after each polishing run.

6.2 Testing and results

As proposed in **Table 6.1**, this work is to explore the possible sources from the machines, the tools, the part and other condition such as slurry.

6.2.1 Virtual pivot of machine testing

The machine's virtual pivot errors (A&B) were checked by clocking. The measurement was: A axis: ±7μm and B axis: ±9μm. This is within the normal range of machine accuracy according to the specification of the machine (A&B errors less than ±10 μm).

6.2.2 Radii and run-out testing of bonnet tools

This work is to find out the true radii and tool surface run-out for R160mm and R80mm solid rubber tools. The tool surface run-out is the deviation between actual surface and ideal spherical surface, which could cause incorrect form correction and asymmetry in the form. The tool radii and the run-out of the tool surface can be tested by use 'Bonnet Probing' program on the machine. The testing results are shown in **Figure 6.1** and **Figure 6.2.**

For the R160mm tool, the true radius is 162.2mm (**Figure6.1**, left) and run-out of the tool surface is 117 μm (**Figure 6.1**, right).

For the R80mm tool, the true radius is 85.8mm (**Figure 6.2**, left) and run-out of the tool surface is 633 μm (**Figure 6.2**, right).

The tool radii that were actually used were 160mm in TPG pre-polishing and 80.3mm in the form-correction. Thus, the differences were 2.2mm for R160 tool and 5.5mm for R80 tool. The run-out of the tool's surface is suggested to be less than 100 μm. These tools were re-dressed after this testing. This is introduced at the next section.
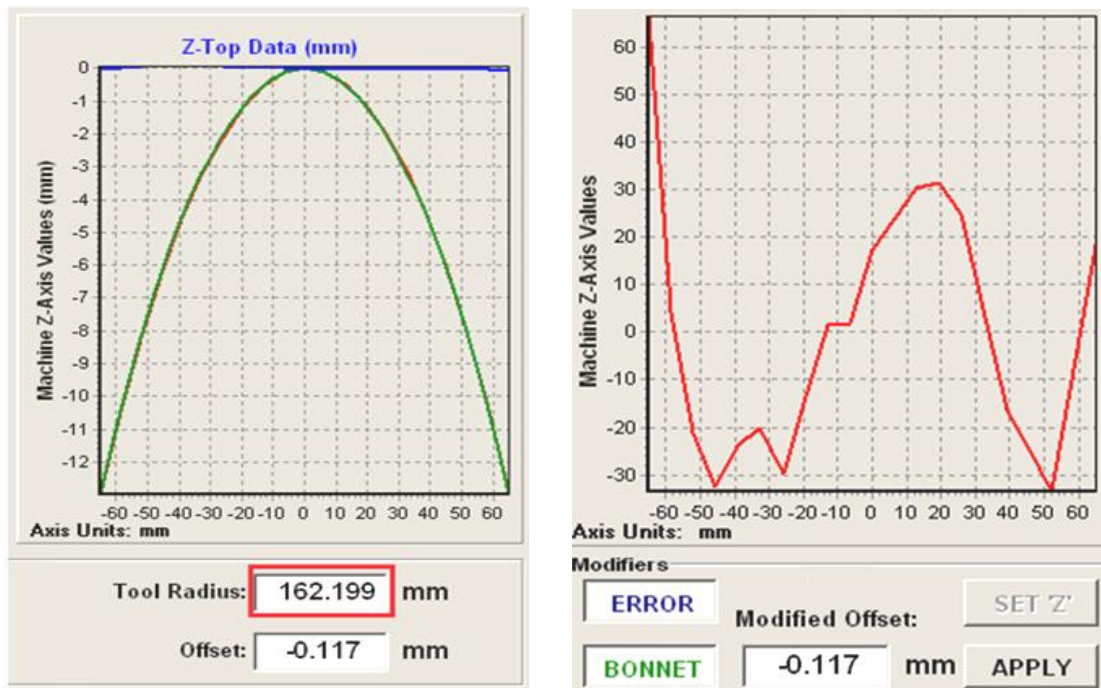
Figure 6.1 R160mm tool testing results, on the left is the tool radius result (R=162.2 mm) and on the right is the tool surface run-out result (117μm run-out) (author's data)
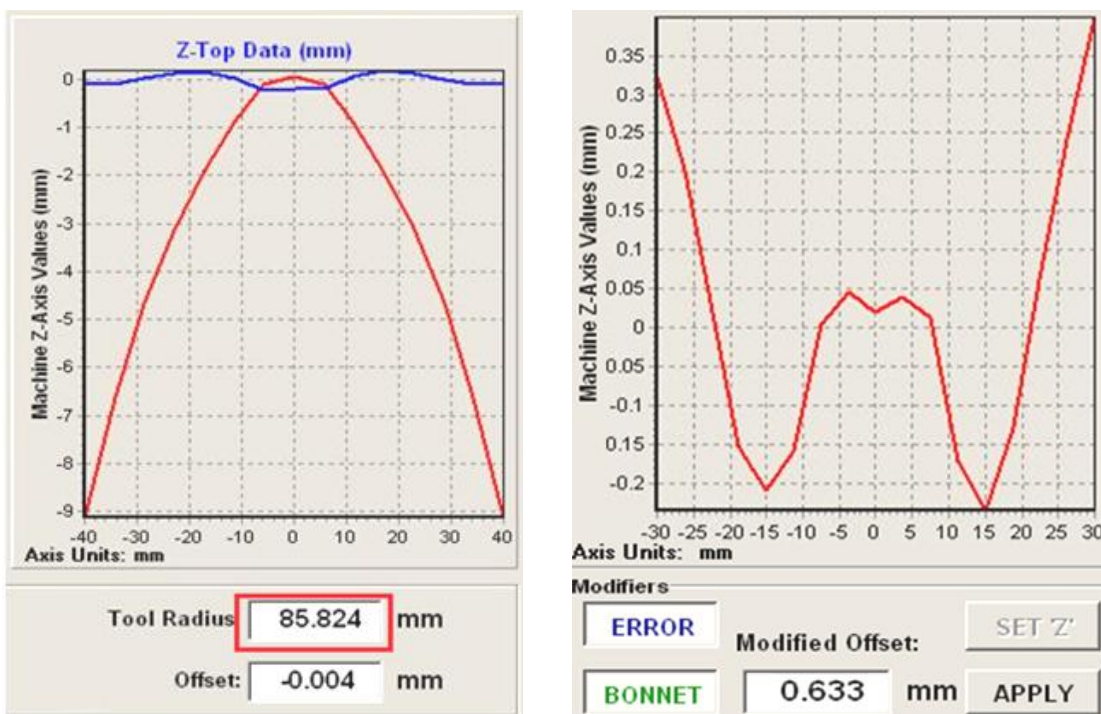
Figure 6.2 R80mm tool testing results, on the left is the tool radius result (R=85.8 mm) and on the right is the tool surface run-out result (633μm run-out) (author's data)

6.2.3 Generation of six TIFs on each edge

As proposed in **Table 6.1**, this work generated six dynamic TIFs near to and equidistant from all six edges, and measured their removal volume, removal depth, width and the distance to the edge with Form Talysurf scanning each TIF individually. Thus, these measurements can help to diagnose the edge asymmetry from the following possible sources:

By measuring the distance from the edge of the TIFs to the edge of the part, it can be determined whether the edges of the part were regular or not, and whether the clocking and alignment were correct or not.

By measuring the width and the removal rate of the TIFs, it can determine whether non-linear probing was correct or not, and whether the removal rate was even or not.

This experiment was carried out on a 200mm cross-corner hexagonal part. This part was the same one that was used for the edge control experiment in chapter 5. The six TIFs and the respective measurement direction are shown in **Figure 6.3**.
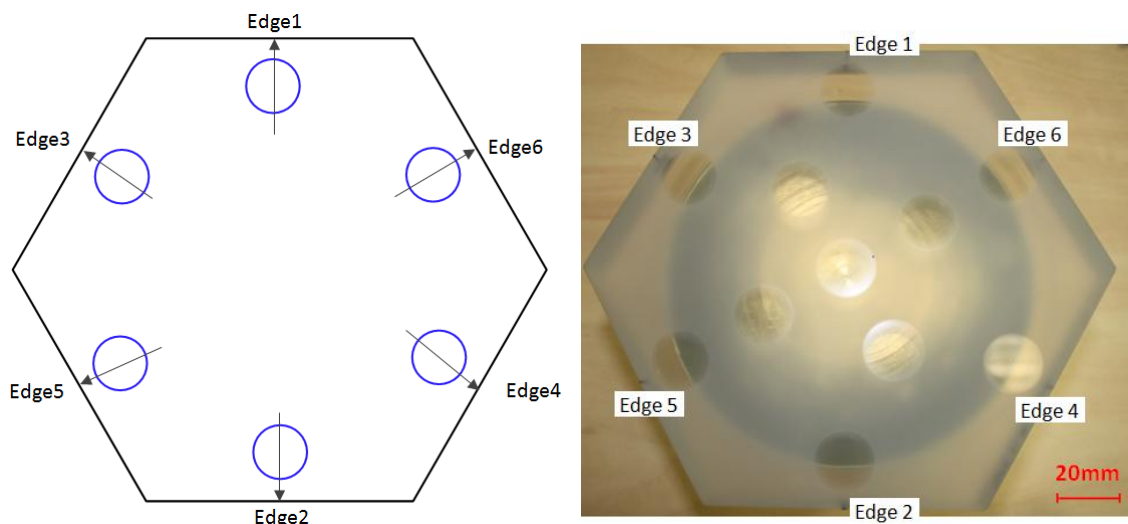
Figure 6.3 The measurement direction of six TIFs on the hexagonal part (picture by author, 2011)

Figure 6.4 shows the Form Talysurf scanning results of six TIFs on each edge. These six TIFs are laid inside of the edge of the part (not overlapping the edges). The measurements and statistics are shown in **Table 6.2**. The measurements of the six TIFs on each edge show the results with no significant errors. The errors of the removal rates, the widths, and distances to the edge are less than 5% (standard deviation/mean). Thus, the regularity of the part, the non-linear probing, the alignment, and the clocking are within the normal range.
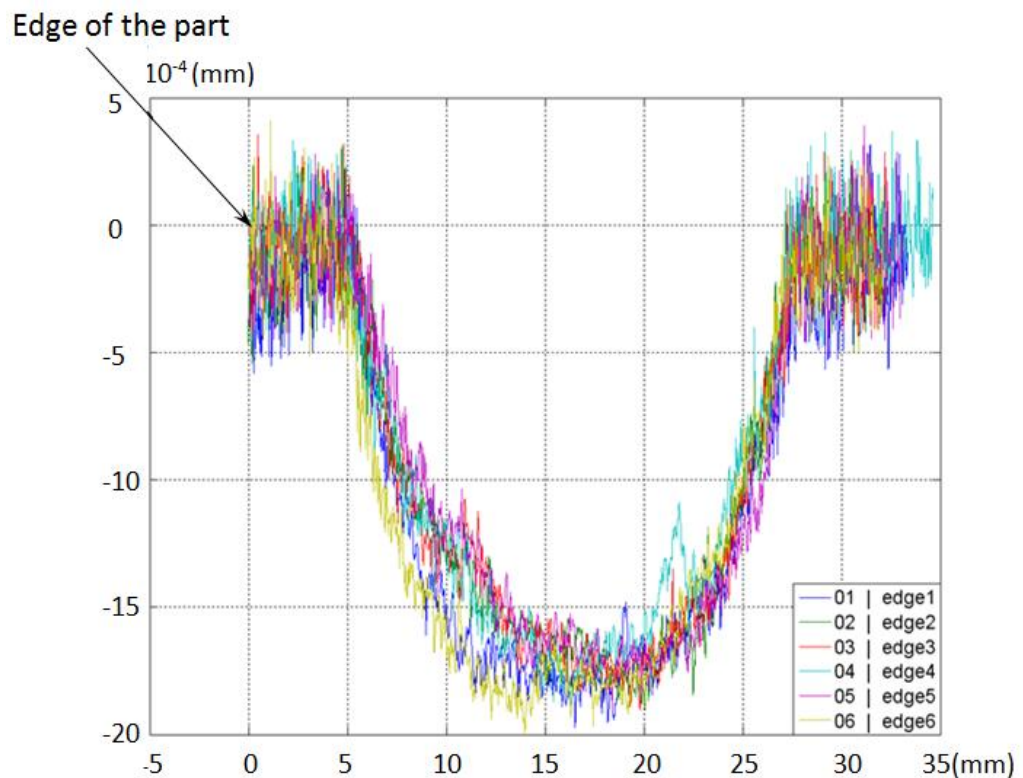
Figure 6.4 The measurements of six TIFs on each edge (author's data)

Table 6.2 The statistics of parameters of six TIFs (author's data)

Location of the TIFs		P-V (µm)	RMS (µm)	Removal volume (µm³/min)	Distance of the peak to edge of the part (mm)	Width (FWHM) (mm)
Edge1		2.2857	0.6823	1.597	16.33	17.9
Edge2		2.2159	0.6644	1.476	16.22	17.2
Edge3		2.2592	0.6761	1.581	16.27	17.1
Edge4		2.2526	0.6820	1.585	16.14	16.7
Edge5		2.3006	0.6680	1.469	16.22	17.1
Edge6		2.3142	0.6755	1.625	16.19	17.8
statistic	mean	2.2714	0.6747	1.5554	16.21	17.3
	σ (standard deviation)	0.036	0.0073	0.0661	0.2481	0.4604
	σ/mean	1.58%	1.08%	4.25%	1.53%	2.66%

6.2.4 Summary of diagnostic results

To diagnose the edge asymmetry, machine testing, tool testing and the generation of six TIFs on each edge of the hexagonal part were carried out. The results are summarised as following:

1. Machine testing

    The virtual pivot error of the machine was ±7µm for A axis and ±9µm for B axis. This was within the normal range of machine accuracy according to the specification of the machine.

2. Tool testing

   For the R160mm tool, there was 2.2mm difference between the true radius and that actually used and 117 μm run-out of the tool surface. For the R80mm tool, the difference was 5.5 mm and the run-out of the tool surface was 633 μm. This is a considerable contributor to the edge asymmetry. The run-out of the tool surface is recommended to be less than 100 μm.

3. Generation of six TIFs in the edge zone

   The measurements of six TIFs on each edge showed no significant errors. Thus, the regularity of the part, the non-linear probing, the alignment and the clocking were not suspected for edge asymmetry.

According to the diagnoses' results, the following aspects are proposed to achieve symmetric edges:

1. Re-dressing of the tools

2. Pre-polishing from all six directions using the R160mm tool

3. Polishing from all six directions in one correction using the R80mm tool

6.3 Verification experiment

The potential causes of the edge asymmetry were diagnosed in the previous section. The tool conditions and the tool-path direction were the main suspects.

To achieve symmetric edges with no down-turn, the strategy of which a raster tool-path in six polishing runs from each corner of the hexagonal part was proposed. Thus, the edges of the hexagonal part were treated equally. The work in this section demonstrates this strategy by experiment.

6.3.1 The part and tools

A 200mm across-corner Zerodur hexagonal part was prepared on a hand lapping machine for this experiment. A groove in the middle of the part was introduced with a diamond tool to establish the absolute depth of removal using Form Talysurf profilometer scanning.

The tools for this experiment are shown in **Figure 6.5**, R160mm solid rubber tool (SN: SRT-160-001) for the pre-polishing and R80mm solid rubber tool (SN: SRT-80-005) for the form-correction. The polishing cloth on both tools was LP66 polyurethane.

Figure 6.5 The tools for the experiment, where on the left is the R160mm tool, and on the right is the R80mm tool (picture by author, 2011)

Both tools were re-dressed and tested on the machine. The tools surface run-out testing results are shown in **Figure 6.6**. It shows that 75µm (before, 117 µm) of run-out for the R160mm tool and 61µm (before, 633 µm) of run-out for the R80mm tool after dressing. The run-out of the tool surface is recommended to be less than 100 µm, thus, this is acceptable.
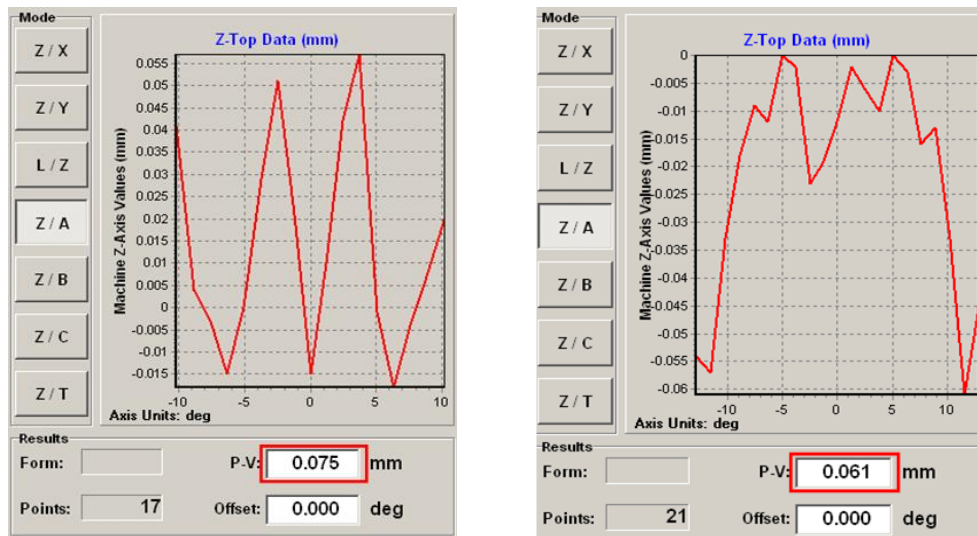
(a) R160mm tool   (b) R80mm tool

Figure 6.6 The run-out testing result after re-dressing, where (a) 61μm for R160mm tool (b) 75μm for R80mm tool (author's data)

6.3.2 Measurement set-up

The 4D 6000 simultaneous phase interferometer and 'Extended Range' Form Talysurf were adopted for these measurements. These are shown in **Figure 6.7**. 2D scanning was applied at each single polishing run to determine the true edges and the cause for the asymmetry. The measurement set-up in this experiment was the same as in chapter 5.

Figure 6.7 The measurement set-up, where left is 4D interferometer, right is 'Extended Range' Form Talysurf (picture by author, 2011)

6.3.3 Pre-polish and results

The R160mm solid rubber tool with a 60mm spot size was used in the pre-polishing. The tool lift parameters were the same as in chapter 5, as shown in **Figure 5.22**. A raster tool-path in the six polishing runs was used, each orientated corner-to-corner in 60° steps. The polishing time of each individual run was approximately 3 minutes, hence 18 minutes in total for the whole pre-polish. The results in **Figure 6.8** show form errors of 3475 nm PV and 981 nm RMS. The 'power' term was not removed from the measurement, to keep a consistent edge height value. The width of the edge upturn was about 40mm. Form Talysurf scans after Pre-polishing show a 6μm removal (at the centre of the part) and no edge roll down in **Figure 6.9**.
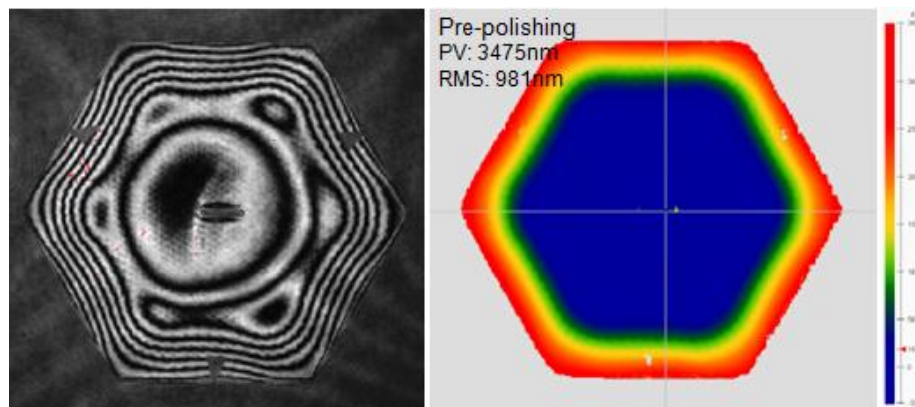
Figure 6.8 Fringe and phase map of surface after pre-polishing (author's data)
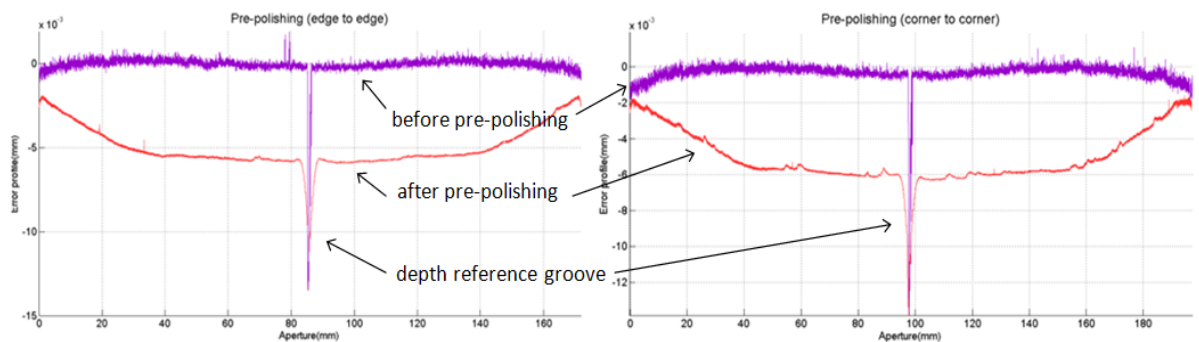
Figure 6.9 Form Talysurf 2D scanning before and after pre-polishing, showing 6μm removal and no edge roll down, left is scanning from edge to edge of hexagon, right is scanning from corner to corner of hexagon (author's data)

6.3.4 Form correction with R80/20mm spot

6.3.4.1 Six direction tool path

An R80mm solid rubber tool with 20mm spot was used for the form correction polishing. The slurry density at this stage was maintained in the range of 1.022-1.023. The tool lift parameters were the same as in **Section 5.5.3.3**, as shown in **Figure 5.25**.

To achieve a symmetric surface form, six polishing runs were carried out for form correction. Each of the six passes constitutes a single raster pass starting from each different corner of the hexagonal part. Every raster trace cuts the edge and is never paralleled to an edge. This was performed by rotating the machine table in 60° steps for each run. Thus, the tool paths of six corrections were identical and the edges of the hexagonal part were treated equally. **Figure 6.10** shows the tool path and the direction of the tool motion for each of the six correction runs.
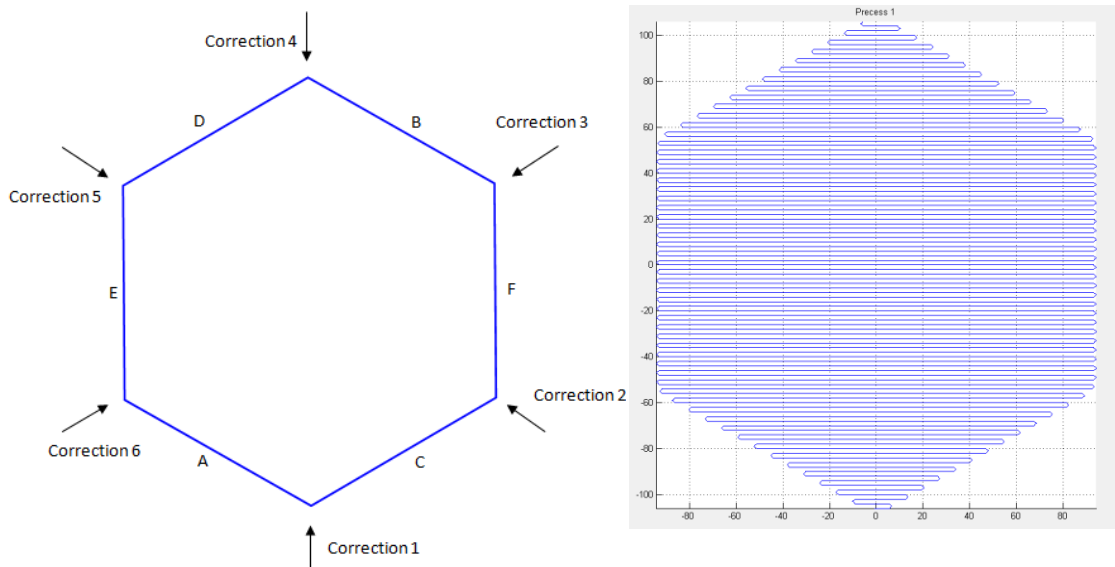
Figure 6.10 The tool path (on the right) and the directions of six correction runs (on the left), the tool path of each run starts from each corner of the hexagonal part (author's picture)

6.3.4.2 Form-correction results

The form-correction was started from a surface error of 981 nm RMS and 3475nm PV including

the edge zone. To ensure each edge was treated equally, the same absolute material removal

was targeted for each correction run. This can be performed by the following:

1. Optimising the removal proportion of the surface error at each correction run to

   keep the absolute removal the same

2. Keeping the polishing time of each correction run the same

The projected pattern and results of each correction run are shown in **Table 6.3**. The surface

error of 91nm RMS and 515nm PV including the edge zone were achieved after six corrections.

From **Table 6.3**, it can be seen that corrections 1 & 2 were under-corrected. After correction 2,

it was observed that the slurry density had fallen to 1.016 (the removal rate was tested with

the density at 1.02). Thus, after correction 2, the starting slurry density was adjusted to

compensate for this decline. After correction 3 and 4, the slurry density was dropped again,

which caused the under-correction of run 5 and 6.

Table 6.3 The projected pattern and results at each correction run (author's data)

	Planned proportion of removal error	Polishing time (minutes)	Started error including edge zone(RMS) (nm)	Residual error including edge zone(RMS) (nm)	Actual proportion of removal error
Correction 1	16.7% (1/6)	23	928	849	9%
Correction 2	20% (1/5)	22	849	794	8%
Correction 3	25% (1/4)	22	794	563	27%
Correction 4	33.3% (1/3)	22	563	338	35%
Correction 5	50% (1/2)	23	338	224	34%
Correction 6	100% (1/1)	20	224	91	61%

The results from correction 1 to correction 6 are shown in **Figure 6.11**. The interferograms were acquired with small masks placed on the surface of the part to identify the true location of the edge at each form-correction run. By this means, it can be seen that the edges of the part were always controlled within the range of the interferometer through the six corrections. The analysis of the edge results is introduced in the following section.
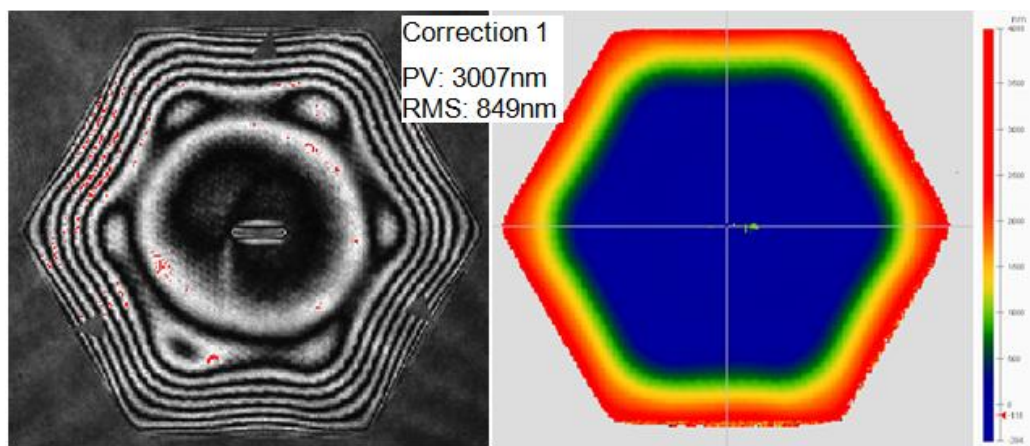
(a) Correction1 (PV: 3007nm, RMS: 849nm)
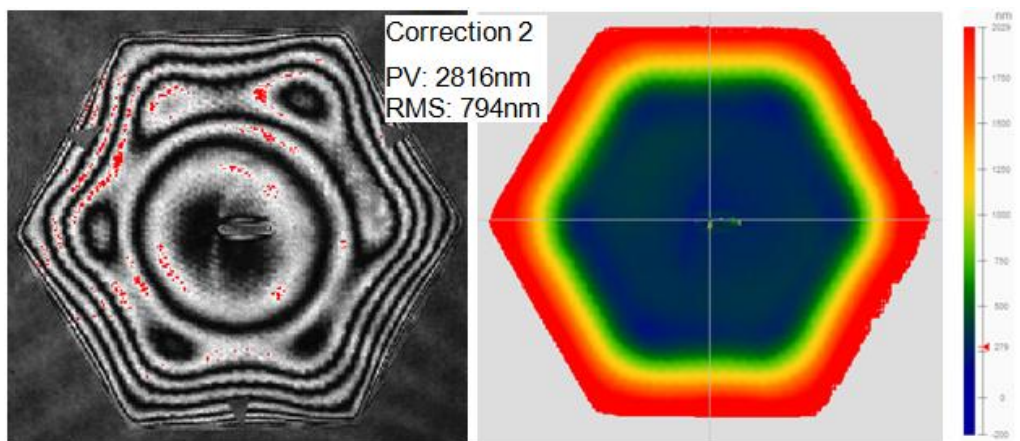
(b) Correction2 (PV: 2816nm, RMS: 794nm)
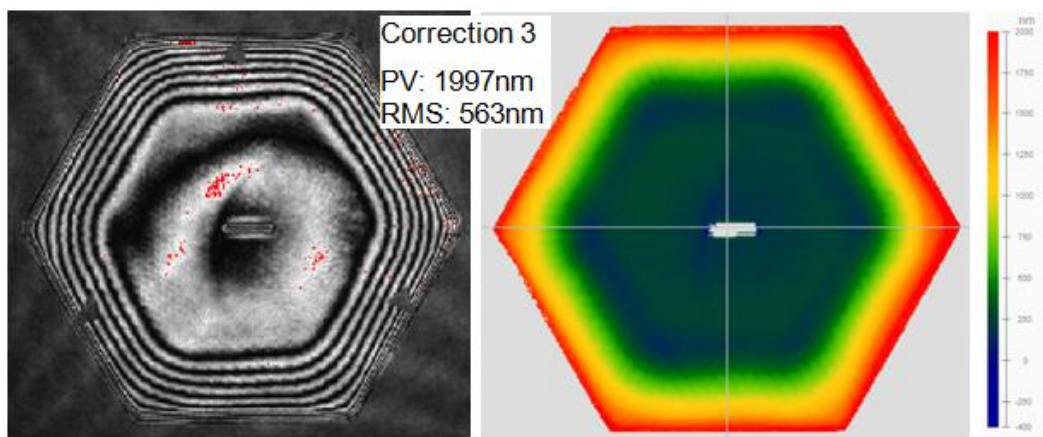
(c) Correction3 (PV: 1997nm, RMS: 563nm)
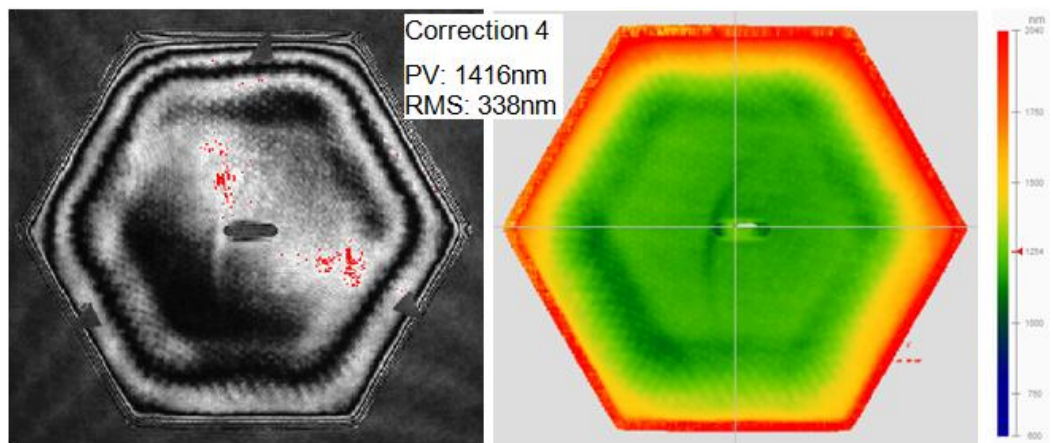
(d) Correction4 (PV: 1416nm, RMS: 338nm)
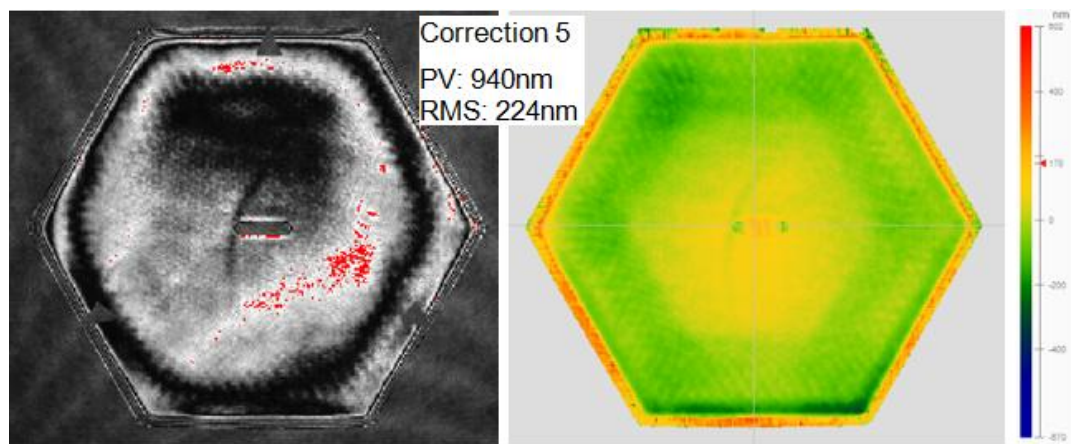
(e) Correction5 (PV: 940nm, RMS: 224nm)
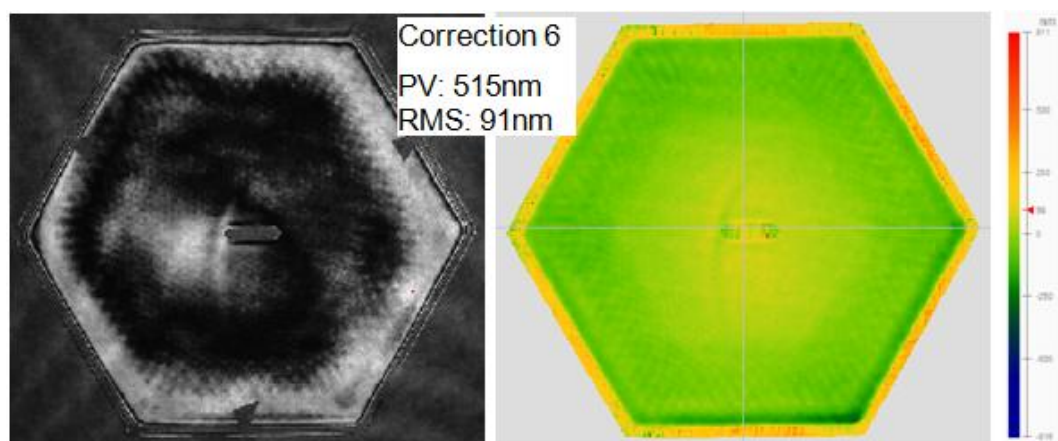
(f) Correction6 (PV: 515nm, RMS: 91nm)

Figure 6.11 The fringe and phase maps of the surface after each form-correction run (author's data)

To identify the true edge of the part and to determine the absolute depths of removal by using the reference groove in the centre of the part, 2D scannings were carried out on the 'Extended Range' Form Talysurf PGI 1240 2D Form Talysurf after each polishing run. All have been plotted together and are shown in **Figure 6.12**, where it can be seen that there is no edge roll down through the whole process. By use of the reference groove, it has been established that approximately 8 μm depth of material removal was removed in the processing of this part.
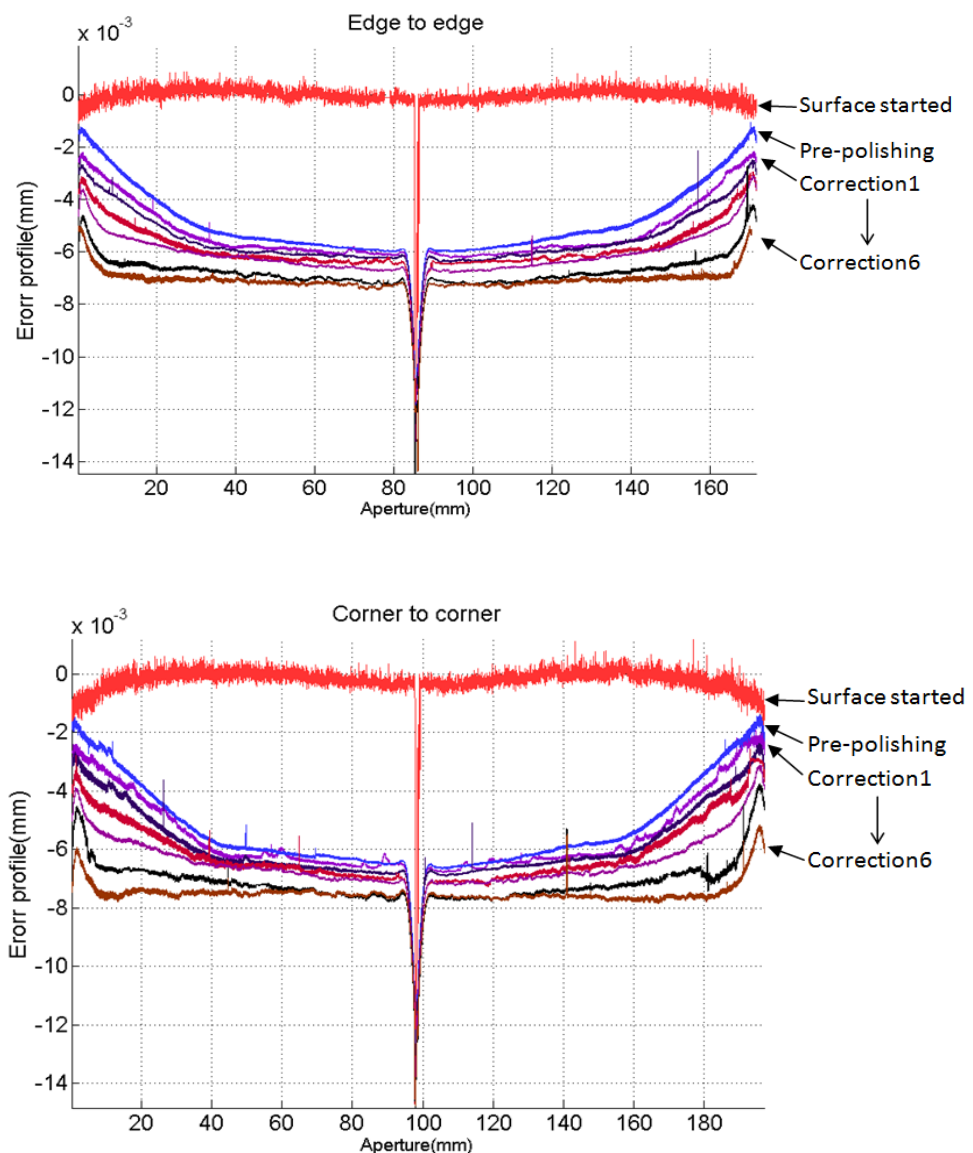
Figure 6.12 Form Talysurf profilometer measurements for each polishing run, the top shows the results from edge to edge of hexagon, and the bottom shows the results from corner to corner (author's data)

6.3.5 Comparison and analysis of the results

The comparisons with the previous results are shown in **Figure 6.13.** On the left are the results achieved from the preliminary edge control experiment in **Chapter 5**, after four form-corrections. It presents asymmetry on the hexagonal part and some edges are already turned-down. The form errors are 1137nm PV and 160nm RMS including the edge zone.

(a) Comparison of the whole measurements

(b) Comparison of the edge results, cutting from (a)
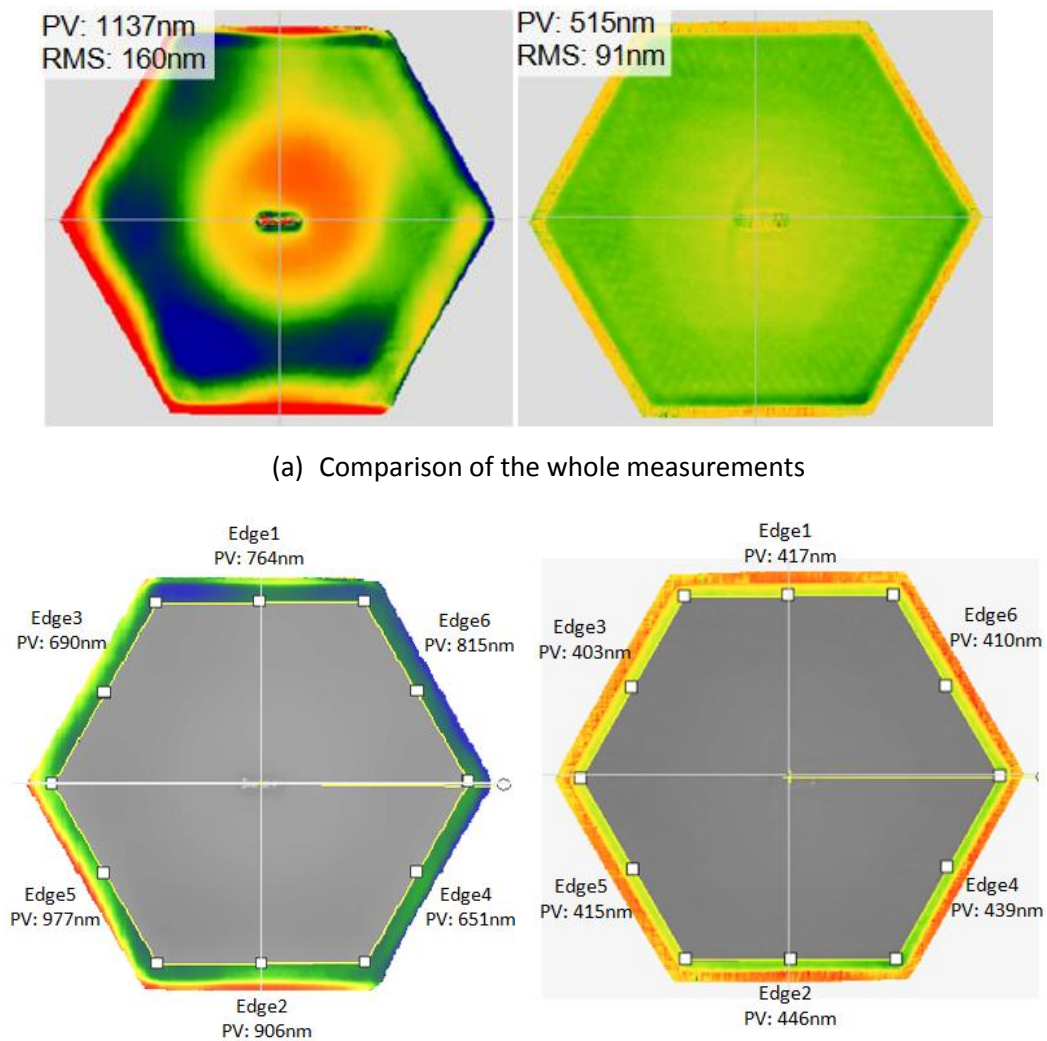
Figure 6.13 Comparison with previous results, where (a) is the comparison of the measurements of the whole part, and (b) is the comparison of the edge results. On the left is the previous result with four directions tool path. On the right is the result with six directions of tool path from each corner and equal absolute removal for each correction (author's data)

On the right of **Figure 6.13** is the result achieved in this experiment with six directions of tool path from each corner and the equal absolute removal for each correction. The results show a form error of 479nm PV and 59nm RMS including the edge zone. All of the six edges are up standing and are controlled within the range of the interferometer through all six corrections. This has been confirmed by means of placing the masks on the surface in the interferogram and Form Talysurf scanning. The symmetric edges are achieved. The up-standing edges can be treated by the subsequent 'Pitch' polishing process. The details of this process are introduced in **Chapter 7**.

6.4 Conclusion

In this chapter, the causes for asymmetric edges have been investigated. It is mainly due to the tools' condition and the mismatch between the tool path directions on the hexagonal part. A strategy to achieve symmetric edges has been demonstrated. For the hexagonal part, six directions of tool path from each corner and an equal absolute removal for each correction run are required. This modified process has been demonstrated by an experiment. The symmetric and up-standing edges have been achieved. These up-standing edges can be treated by the subsequent smoothing process. **Chapter 7** will demonstrate the whole process and finally it reaches the ESO's specifications.

Chapter 7

Experimental demonstration of the process-chain

This chapter presents two sets of experiments with the 'Tool lift' edge control technique of which the material DC-removals are respectively 3μm and 15μm. The aim of the experiments is to demonstrate two possible process-chains for the E-ELT project, following grinding the asphere on the BoX with 8-10 μm subsurface damage.

1. Process-chain 1 (3μm total DC-removal): final rectification after cutting a polished roundel to hexagonal shape after 15 μm depth material removal has been achieved

    1.1 Polishing & Correcting a roundel (15 μm removal)

    1.2 Final rectification after cutting a roundel to hexagonal shape (2-3 μm)

2. Process-chain 2 (15μm total DC-removal): performing all the processing on a hexagonal segment (15 μm removal)

The experiments were conducted on 200mm across-corners, R=3m spherical concave, Zerodur hexagonal parts. The parts were prepared by free-abrasive lapping on a cast iron tool. R160mm and R80mm solid rubber tools were used in the experiments.

7.1 Methodology of practical edge control

In **Chapter 5**, three Methodologies for edge control were presented. With low risk and preliminary experimental success, the 'Tool lift' technique has been adopted in the E-ELT prototype segments' processing-chain. As already mentioned in chapter 5, this strategy for

edge control is described as follows:

1. The comparatively large polishing spots are applied over the bulk surface to give high volumetric removal rates in pre-polishing and form-correction polishing. The edge is left up-standing by tool lift.

2. The smaller spot-sizes then encroach on the up-stand and progressively reduce its size and width.

The principle of this approach is that the whole surface needs to be always within the measurement-range of the interferometer.

The stability of this technique was established over three parts. Typically, after form correction, edges are turned-up with <1μm in height, 7mm in width. To clean up the up-standing edges and surface, a pitch tool polishing process was developed, as introduced in the following section.

7.2 Pitch tool polishing process

Pitch polishing is one of the most historic processes. Polishing with pitch tooling can produce surfaces with low roughness and negligible subsurface damage. As already mentioned in **Section 2.4**, pitch is a viscoelastic material with complex material properties, which are low softening point (55-70°C) and hardness (60-80, by Shore. D) (OSA, 2011). Compared to glass, pitch is very soft; therefore, it takes the shape of the part during the polishing and remains in close contact without scratching. Compositions of the pitch are mostly proprietary. Generally, the material consists of various amounts of tar, oil, wood and rosin (OSA, 2011).

A 100mm diameter pitch tool was developed for the E-ELT project by the Production Team as shown in **Figure 7.1**. The composition consists of two types of optical polishing pitch (Gugolz73

and Gugolz64) and wood flour. The proportions are 70% of Gugolz73, 25% of Gugolz64 and 5% wood flour by weight. To form a pitch polisher, the pitch is warmed and formed to the optic with a 4-5mm layer. A metal tool is then coated. Once the pitch has cooled, the irrigation grooves are cut on the pitch tool surface to allow for slurry access.
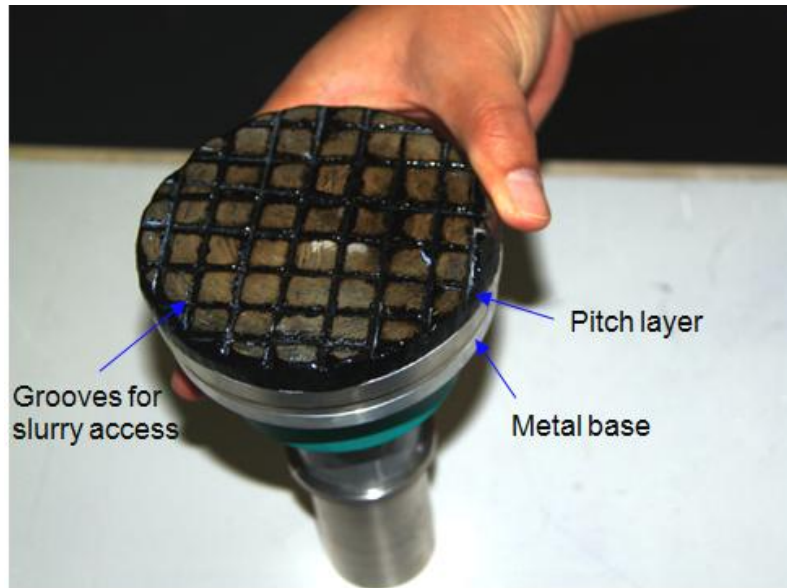
Figure 7.1 The R100mm pitch polishing tool (picture by author, 2001)

The pitch tool polishing for the process in the E-ELT process-chain plays two important roles:

1. Removal of BoX™ mid-spatial features

2. Treatment of up-standing edges after form- correction

Figure 7.2 shows the texture measurements after bonnet polishing and after pitch tool polishing using an ADE Phase Shift MicroAXM white-light texture interferometer. It can be seen that in the measurement region of 1.4mm x 1mm, after bonnet polishing the surface roughness Sa=3.71nm and after pitch polishing Sa=0.502nm.
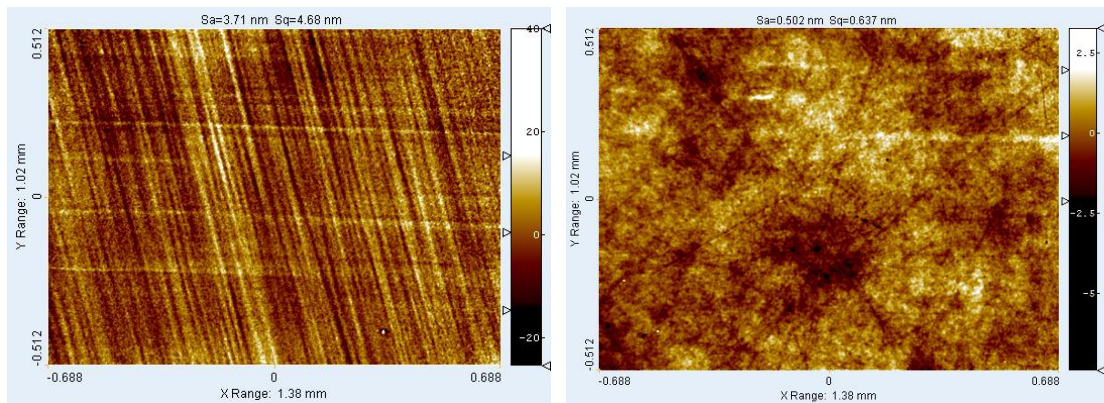
(a) After bonnet polishing   (b) After pitch polishing

Figure 7.2 The texture measurements in the range 1.4mm x 1 mm, where (a) is after bonnet polishing, Sa=3.71nm; (b) is after pitch polishing on the Zeeko machine, Sa=0.502nm (author's data, 2011)

7.3 Process-chain 1 (3µm total DC-removal)

In this process-chain:

1. The pre-polishing and form-corrections have been conducted with an R80mm solid rubber tool with a 20mm spot. The polishing cloth was polyurethane LP66. According to the diagnosis results in **Chapter 6**, the total material DC removal was equally divided into six polishing runs that were three pre-polishing runs and three correction runs. The starting corners were chosen to be evenly distributed.

2. An R100mm pitch tool was used for the cleaning of the up-standing edges and the surface smoothing. At this stage, three sets of pitch runs were carried out and each set included six raster runs, one from each corner.

3. An R80mm solid rubber tool with Uni-Nap polishing cloth was used for the final form correction. Polishing with Uni-Nap provides a low material removal rate and good quality of a surface topography compare with polyurethane, see the removal rate table in the **Appendix**. It is suitable for the final form correction.

181

The part was a 200mm across-corners, R=3m spherical concave, Zerodur hexagon which was prepared by free-abrasive lapping on a cast iron tool. A groove was introduced with a diamond tool in the centre of the test-part to provide a datum that establishes the absolute depth of DC removal using the Form Talysurf profilometer.

The masks were placed on the surface of the part to identify the true location of the edges in the interferogram through each measurement of the whole process-chain.

7.3.1 The results of process-chain 1

7.3.1.1 Pre-polish result

After three pre-polishing runs with R80/20mm spot, the PVq (99%) and the RMS of the entire surface were 860nm and 140nm respectively as shown in **Figure 7.3**. The processing time for pre-polishing was 21minutes x 3=63 minutes.
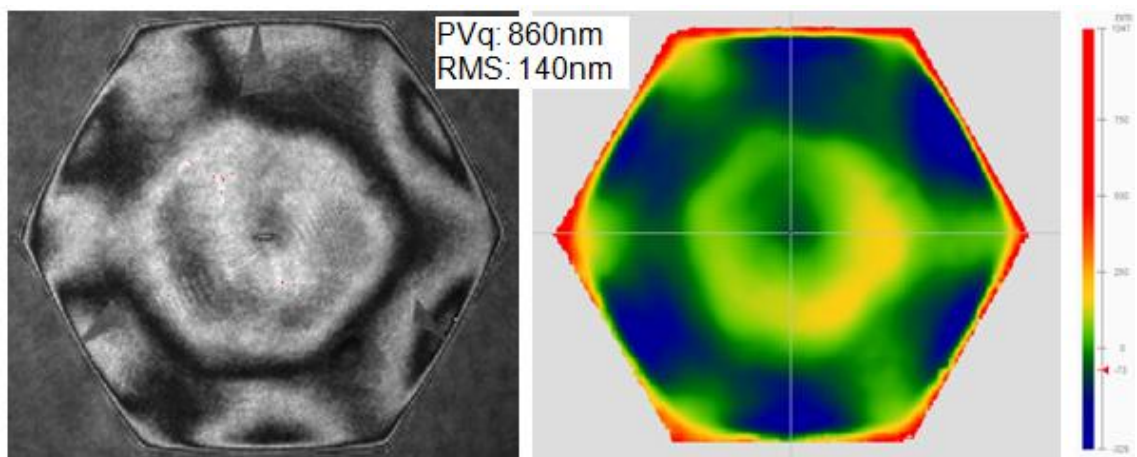
Figure 7.3 Pre-polishing measurement of process-chain 1, where PVq (99%) =860nm and RMS=140nm (author's data)

7.3.1.2 Form-correction result

To maintain the symmetry of edges, the total error was equally divided between three correction runs. **Figure 7.4** shows the measurement after three form-correction runs with R80/20mm spot. PVq (99%) and RMS of the entire surface were 307nm and 43nm respectively. The total processing time for form-correction was 65 (23+21+21) minutes.

Symmetric and up-standing edges were achieved after the form-correction. The edges were about 7mm wide. Although the extreme edge was unable to be acquired through interferometry, it can be brought back by cleaning up the surface and edges with the pitch tool.
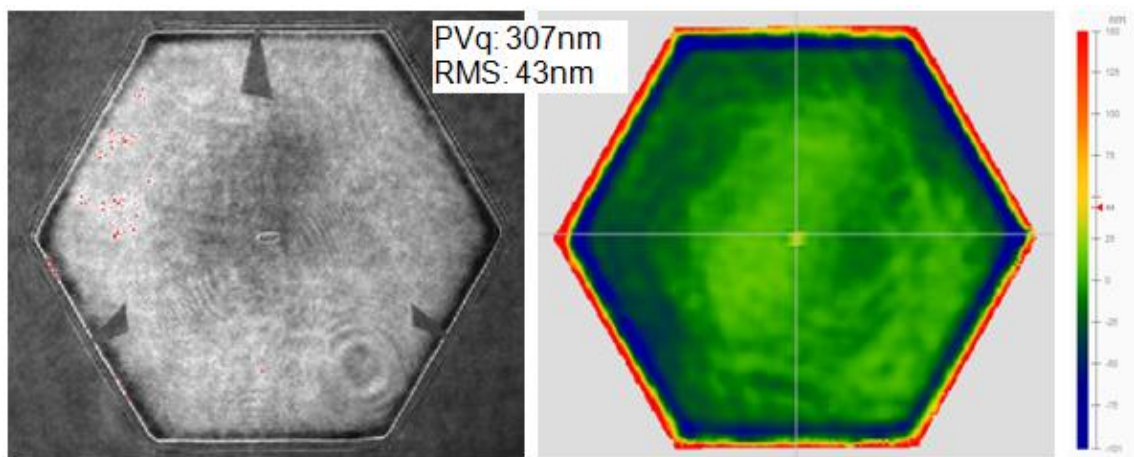
Figure 7.4 Form-correction measurement of process-chain 1, where PVq (99%) =307nm and RMS=43nm (author's data)

7.3.1.3 Pitch tool polishing result

Three sets of pitch polishing process were carried out after the form correction. Each set includes six raster runs, one from each corner. The measurements after the pitch tool polishing are shown in **Figure 7.5**. PVq (99%) and RMS of entire surface are 187nm and 36nm respectively. It can be seen that the up-standing edges have been treated down by the pitch

polishing process and recovered into the measurement-range of the interferometry. The

processing time for pitch polishing was 36 (3 x 6 x 2) minutes.
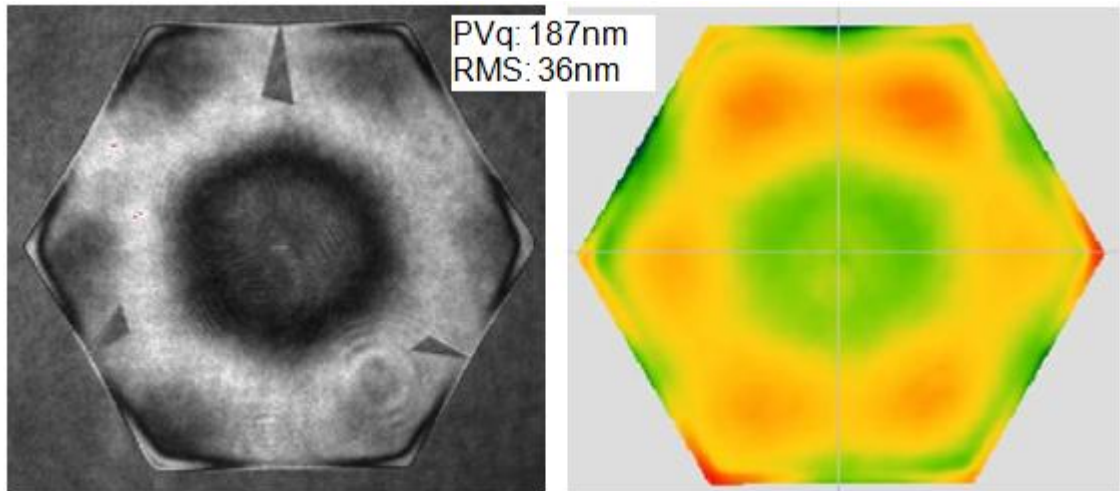
Figure 7.5 The measurement after pitch tool polishing of process-chain 1, where PVq (99%) =187nm and RMS=36nm, up-standing edges have been recovered into the measurement-range of the inteferometry (author's data)

7.3.1.4 Final correction (Uni-Nap polishing cloth) result

The pitch tool polishing process introduces a small regression in the form. It can be restored by final correction with the R80 solid rubber tool with the Uni-Nap polishing cloth. **Figure 7.6** shows that after one correction run with a 20mm spot, PVq (99%) and RMS including edges are 120nm and 22nm respectively. The processing time for this correction run was 17minutes.
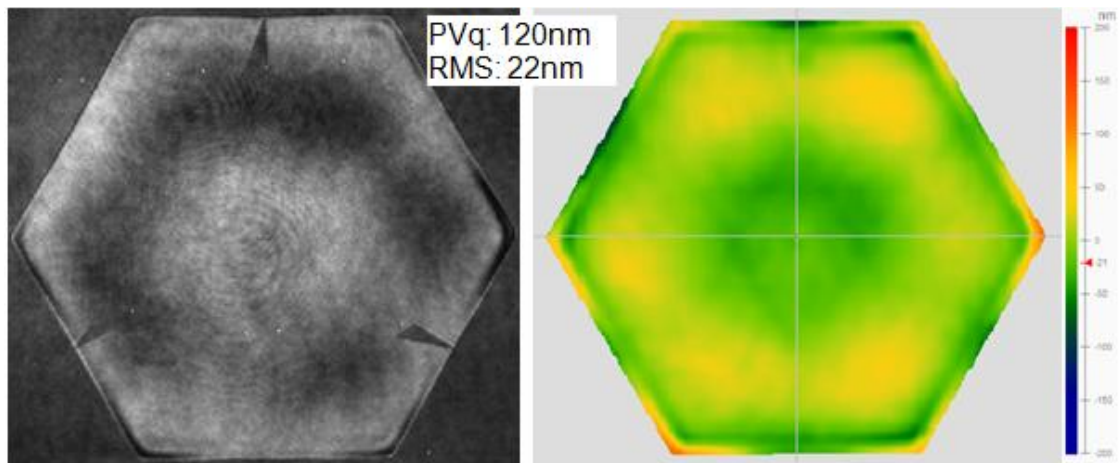
Figure 7.6 Uni-Nap -correction measurement of process-chain 1, where PVq (99%) =120nm and RMS=22nm including edges (author's data)

7.3.1.5 Roughness result

Figure 7.7 is the roughness measurement result after final correction using the ADE Phase Shift MicroAXM white-light texture interferometer. It can be seen that in the measurement region of 1.4mm x 1mm roughness Sa=1.42nm. This is within the ESO specification of 3nm, 2nm goal (see **Section 1.9.2**).

Figure 7.7 The roughness result of the process-chain 1, where, the measurement range is 1.4mm x 1 mm, Sa=1.42nm (author's data)

7.3.1.6 Absolute depth of removal

Using Form Talysurf profilometer measurements, the absolute depth of removal was established by a reference groove on the part. **Figure 7.8** shows the profiles after free-abrasive lapping and after final correction. It can be seen that approximately 3µm DC-removal has been achieved in this process-chain.

Figure 7.8 Absolute material removal measurement of process-chain 1, where, the red profile is the Form Talysurf measurement after free-abrasive lapping and the purple profile is after the final correction, 3µm DC-removal was built into this process-chain (author's data)

7.3.2 Results analysis of process-chain 1

This section reviews the results according to the E-ELT specification. As already mentioned in the **Section 1.9.2**, the ESO specification was ambiguous regarding the datum with respect to which edge mis-figure is measured, also the method of measurements. Walker (2012B), proposed to ESO a refined measurement protocol in January 2012, which ESO has accepted. In this protocol, the 95% PVq (rather than 99% PVq adopted previously) represented a significant but reasonable concession on the segment of ESO. In this chapter, the data is analysed as follows:

1. The part is measured on the interferometer.

2. A 0.5 mm wide band around the periphery is removed from the data, to represent the margin for final bevelling.

3. Tip/tilt, de-focus and astigmatism are removed from the resulting data-set.

4. The useful area is defined as the bulk surface excluding the 10mm wide peripheral zone.

5. The useful area is cut out of the data-set and analysed to provide the RMS.

6. The remaining 10mm wide hexagonal ring is divided into six individual trapezoidal edge-segments, each of which is analysed separately to provide the respective PV and PVq (95%) edge mis-figure numbers.

The analysis of the interferometer data after the final correction is shown in **Figure 7.9**. The statistics of the results are listed in **Table 7.1**. It is shown that the results (maximum edge mis-figure, average edge mis-figure and useful area) in this process chain are numerically lower than the E-ELT specification (as shown in **Table 1.2**). The details of comparison with E-ELT specification is discussed in the following section.

Figure 7.9 Final result of process-chain 1 (3μm DC-removal), where the data-set are analysed after removing 0.5mm margin around edge which represents the margin for final beveling, the data of six edges is PV and PVq (95%) from each trapezoidal sector (10mm in height), useful area of surface is measured excluding 10mm edge-zone (author's data)

Table 7.1 The statistics of the final result of process-chain one (3μm DC-removal) (author's data)

PV for each of six edge zones (nm)			PVq(95%) for each of six edge zones (nm)			Average of PV (nm)	Average of PVq(95%) (nm)	RMS(surface) useful area (nm)	Roughness Sa(nm)
116	163	168	81	107	112	142	92	18	1.42
143	145	118	92	97	67				

7.4 Process-chain 2 (15µm total DC-removal)

7.4.1 The results of process-chain 2

The part for this process-chain was the same part as used in process-chain 1, which was a 200mm across-corners, R=3m spherical concave, Zerodur hexagonal part and prepared by free-abrasive lapping on a cast iron tool. In this process-chain:

1. The pre-polishing was conducted with an R160mm solid rubber tool with 60mm nominal spot size (50mm in actual), which aimed to achieve a high volumetric removal rate over the bulk surface. The polishing cloth was polyurethane LP66. Six pre-polishing runs in total were started from each corner and the processing time of each run was 4.5 minutes. With the 'Tool lift' edge control technique, the broad edges were left up-standing. The pre-polishing result is shown in **Figure 7.10**, where, PVq (99%) and RMS of the entire surface are 4149nm and 1084nm respectively.

2. The form-correction was performed with an R80mm solid rubber tool with a 20mm spot. The polishing cloth was polyurethane LP66. To achieve symmetric edges, the total form error was equally divided into six correction-runs as discussed in chapter 6. The polishing time for each correction run was approximately 20 minutes. The result after six form-corrections is shown in **Figure 7.11**, where, PVq (99%) and RMS of the entire surface are 803nm and 67nm respectively.

3. An R100mm pitch tool was used for cleaning the up-standing. In this process-chain, five sets of pitch runs were carried out and each set included six raster runs, one from each corner. Finally, an R80mm solid rubber tool with Uni-Nap cloth was used for final form-correction. After pitch polishing and one final form-correction, the result is shown in **Figure 7.12**. PVq (99%) =189nm and RMS=26nm including the edge zone have been achieved. The analysis of the results is introduced in the following section.
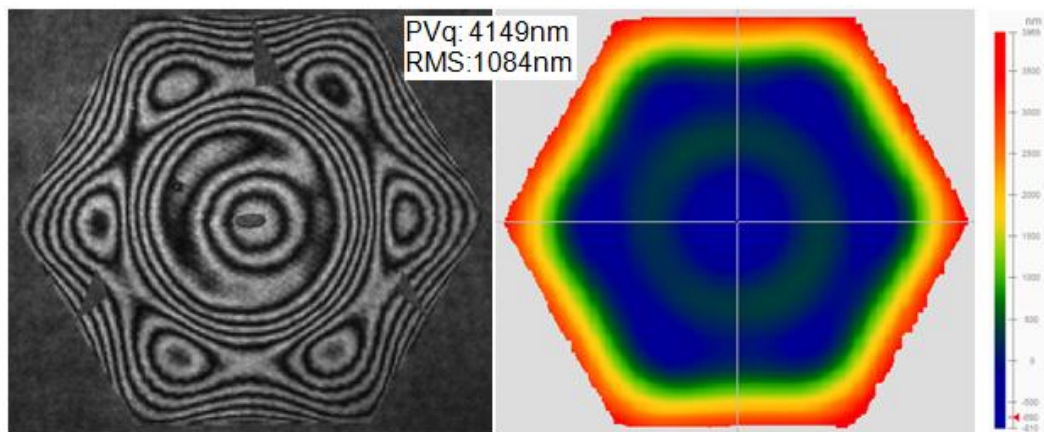
Figure 7.10 Pre-polishing measurement of process-chain 2, where PVq (99%) =4149nm and RMS=1084nm (author's data)
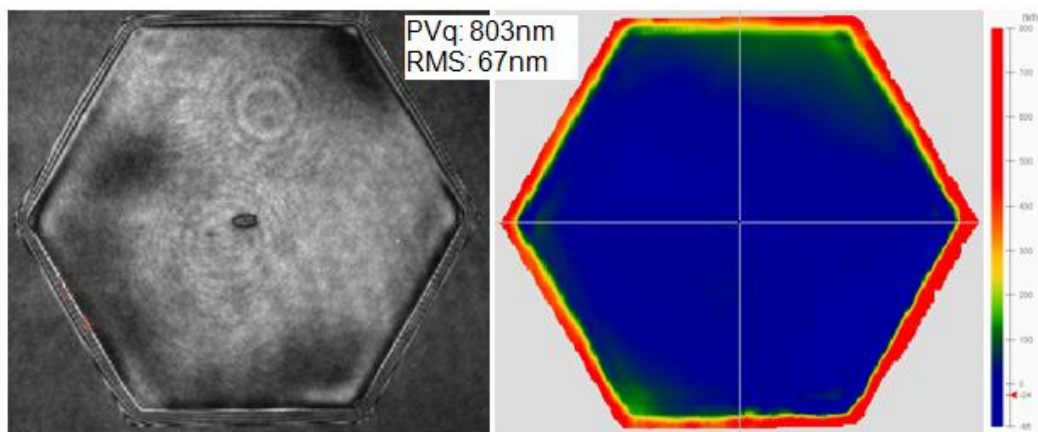
Figure 7.11 The measurement after six form-corrections of process-chain 2, where, PVq (99%) =803nm and RMS=67nm (author's data)
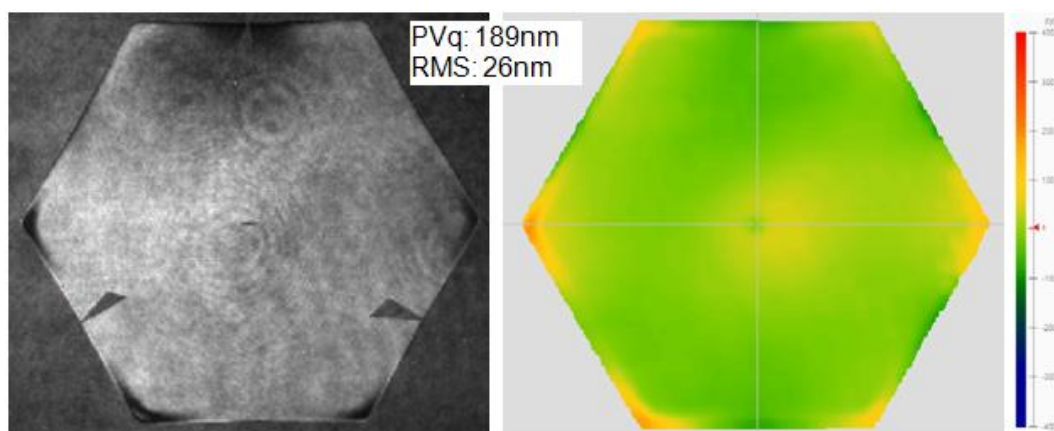
Figure 7.12 The measurement after pitch polishing and Uni-Nap cloth final correction of process-chain 2, where, PVq (99%) =189nm and RMS=26nm (author's data)

The roughness of the final surface was measured using the ADE Phase Shift MicroAXM white-light texture interferometer as shown in **Figure 7.13**. In the measurement region of 1.4mm x 1mm, the roughness Sa=1.42nm. This is within the ESO specification of 3nm, 2nm goal.
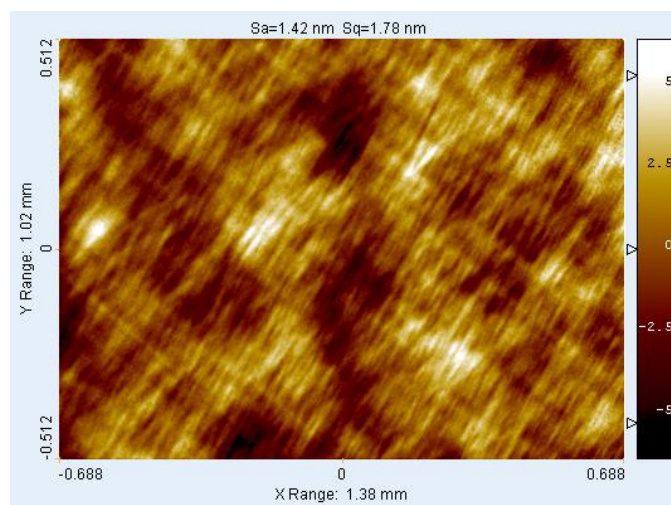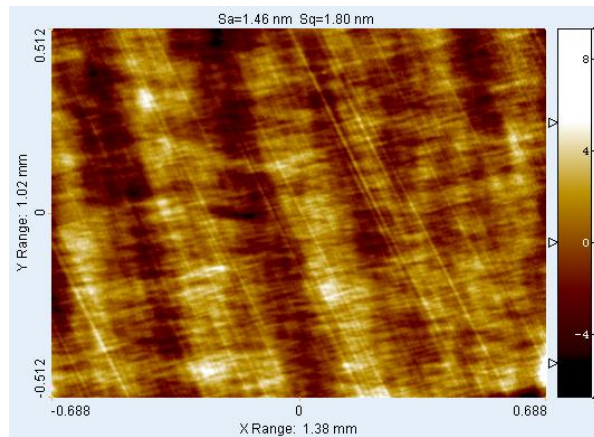

Figure 7.13 The roughness result of the process-chain 2, where, the measurement range is 1.4mm x 1 mm, Sa=1.42nm (author's data)

The Talysurf profilometer measurements of the part after free-abrasive lapping and after final correction are shown in **Figure 7.14**. By the reference groove on the part, it can be seen that approximately 15µm absolute depth DC-removal was achieved in this process-chain.
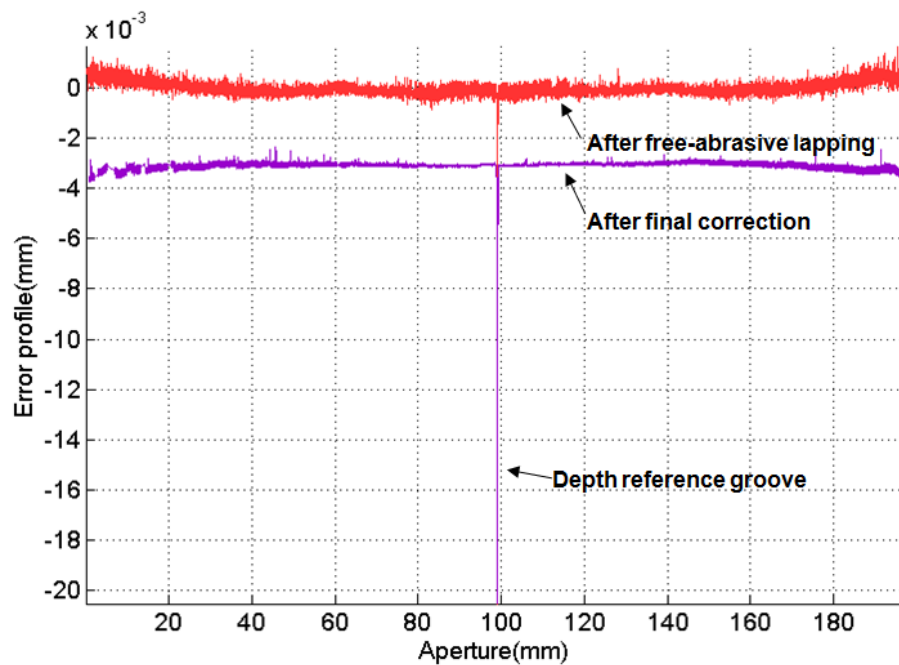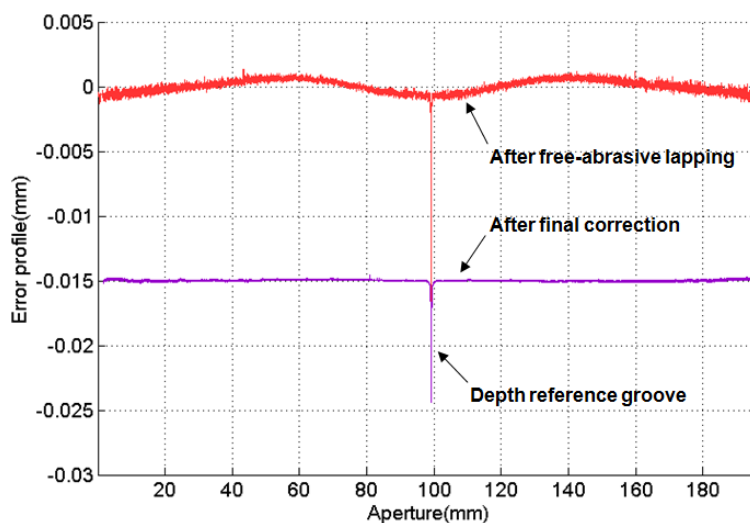

Figure 7.14 Absolute material removal measurement of process-chain 2, where the red profile is the Form Talysurf measurement after free-abrasive lapping and the purple profile is after the final correction, 15µm DC-removal was built into this process-chain (author's data)

7.4.2 Results analysis of process-chain 2

The data are analysed according to the definition, which is listed in **Section 7.3.2**. The analysis of the final interferometer data is shown in **Figure 7.15**. The statistics of the results are listed in **Table 7.2**. To sum up, PVq (95%) of each individual edge is lower than the maximum in the E-ELT specification (200nm, surface). The average PVq (95%) is 138nm, which is above the specified average (100nm, surface). The RMS of the surface of the useful area (excluding 10mm edge-zone) is lower than E-ELT specification (50nm surface).
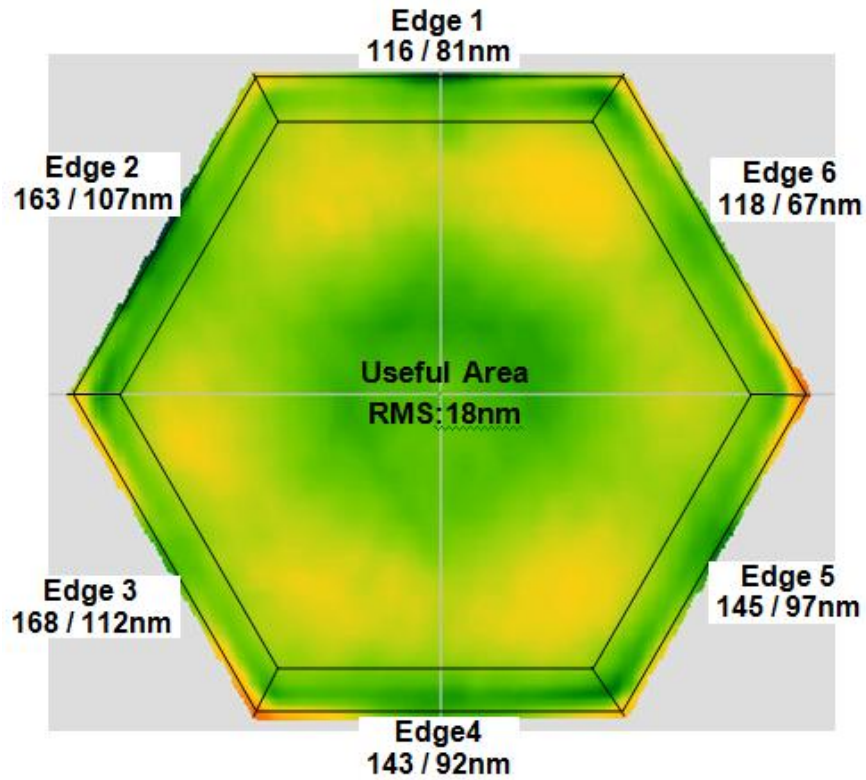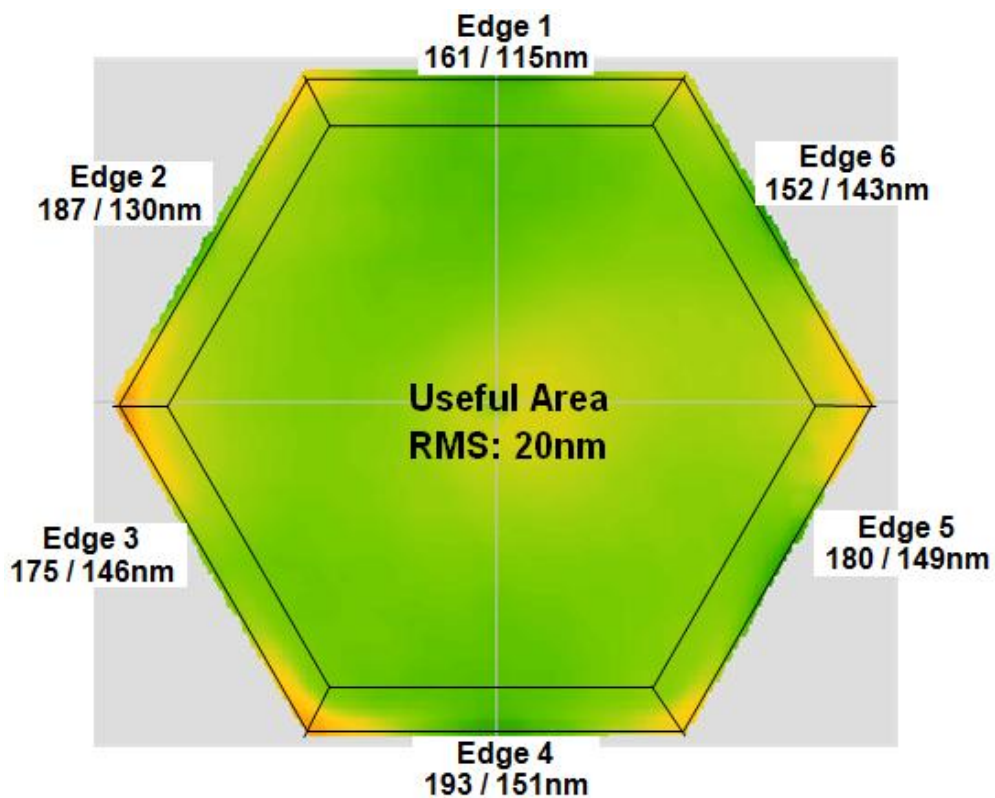

Figure 7.15 Final result of process-chain 2 (15µm DC-removal), where the data-sets are analysed after removing the 0.5mm margin around edge which represents the margin for final beveling, the data of six edges is PV and PVq (95%) from each trapezoidal sector (10mm in height). The useful area of surface is measured excluding 10mm edge-zone (author's data)

Table 7.2 The statistics of the final result of process-chain two (15µm DC-removal) (author's data)

PV for each of six edge zones (nm)			PVq(95%) for each of six edge zones (nm)			Average of PV (nm)	Average of PVq(95%) (nm)	RMS(surface) useful area (nm)	Roughness Sa(nm)
161	187	175	115	130	146	174	138	20	1.46
193	180	152	151	149	143				

7.5 Comparison of the results and E-ELT specification

Two process-chains giving substantial different depth of removals were demonstrated on the 200mm across-corners, R=3m spherical concave, Zerodur hexagonal parts in this chapter. Drawing together, the results for the two process-chains are summarised in **Table 7.3**. The data were analysed according to the definition for E-ELT specification (see **Section 1.9.2**). From comparison with the E-ELT specification, it can be seen that:

1. In process-chain 1, the final results (useful area, the maximum/average edge mis-figures and the roughness) were numerically lower than the E-ELT specification.

2. In process-chain 2, the results of the useful area, the maximum of each individual edges and the roughness were lower than the E-ELT specification. The average of PVq (95%) of six edges is 138nm, which was above the specified average (100nm, surface). It was noted that the dominant edge-defect remaining in the PV numbers was the turning-up of the corners (as shown in **Figure 7.15**), which is currently under investigation. A process of final local edge-rectification to treat the turned-up corner in the edge zone was proposed. The details of this process and some suggestions are introduced in the next chapter.

Table 7.3 The comparison of the results and E-ELT specification (author's data)

	Useful area RMS(nm)		The edges PVq(95%)(nm)		The roughness (nm)
	Overall surface error	Surface error after removal of low- and mid-spatial	Maximum surface error	Average of surface error	
E-ELT specifications for single segment	50	15	200	100	2
Process-chain1 (3µm DC removal)	18	11	112	92	1.42
Process-chain2 (15µm DC removal)	20	14	151	138	1.46

The end-to-end process time for the two process-chains is given in **Table 7.4**. The initial free-abrasive lapping on a cast iron tool is excluded. A prediction of the total process time for an E-ELT segment can be made by scaling all the process-times by the relative areas. For process-chain 1, 3µm DC-removal, an estimated total time of 148 hours is needed for processing an E-ELT segment. For process-chain two, 15µm DC-removal, approximately 167 hours is needed.

This prediction is pessimistic because, on a 200mm hexagon, corrective polishing spends a disproportionately large time reducing the large edge up-stand left by pre-polishing. On an E-ELT segment, most of the time is polishing the bulk surface.

Table 7.4 The prediction of total process time for an E-ELT segment (author's data)

	Time for process-chain one on 200mm across-corners hexagon(mins)	Time for process-chain one on 200mm across-corners hexagon(mins)
Pre-polishing	63 (R80/20mm spot, 1.5µ removal)	25 (R160/20mm spot, 10µ removal)
Corrections	65	120
Pitch polishing	36	60
Uni-Nap cloth correction	17	17
Totals	181	205
Time for simple extrapolation to 1.4m cross-corners segment	8,869 mins = 148 hours	10,045 mins = 167 hours

From **Table 7.4,** it can be seen that, in process-chain 2 attributed to using a large tool (R160/50mm spot) for pre-polishing, the process speed has been significantly increased. It needed only 19 hours extra processing time, and the DC-removal is increased from 3µm to 15µm. Therefore, a large tool (e.g. R200mm) is suggested for further speeding-up of the process. The new R200mm solid rubber tool is currently being developed by the Design Team, see **Section 8.2.2**.

Chapter 8

Conclusion and future work

This thesis has reviewed different techniques for fabrication of the large aspheric surface. The *'Precessions'* polishing technique with many advantages has been adopted as the core technique for manufacturing the prototype mirror segments for the European Extremely Large Telescope (E-ELT). The specifications of these segments' surface are highly challenging, and the manufacture of 931 such segments in a few years demands a new process that requires deterministic, automation of fabrication, metrology and handling, and minimization of manual interventions. The research work in this thesis has been involved in developing an advanced manufacturing process for E-ELT's segments. The purpose of this study is to address some key techniques for the *'Precessions'* polishing approach, such as: characterising tool influence functions; edge control; diagnoses of the edge asymmetry of hexagonal parts; optimisation of process parameters and the speed-up of the whole process. This goal was achieved and two possible process-chains for E-ELT project have been developed and demonstrated on a 200mm across corners, Zerodur, hexagonal part, which are following after grinding the asphere on the BoX with 8-10 μm subsurface damage:

1. Process-chain 1 (3μm total DC-removal) for the final rectification after cutting a polished roundel to hexagonal shape after 15 μm depth material removal has been achieved

2. Process-chain 2 (15μm total DC-removal): performing all the processing on a hexagonal segment

8.1 Overview of the technical advance recorded in the thesis

The tool influence functions (TIFs) characterise the local effect of the process and therefore is of fundamental importance for a successful deterministic '*Precessions*' process. According to the Preston equation, a model that can predict the shape of the TIF for a given tool and condition has been established by means of finite element analysis (FEA). The demonstration of simulation showed a good agreement with the experimental result.

The edge effect is regarded as one of the most difficult technical issues with segment production. Three strategies for edge control have been presented and compared. With low risk and experimental success, the 'Tool lift' edge control technique has been adopted in the E-ELT prototype segments' processing-chain. In 'Tool lift', the edge is left up-standing at every process-step, and a range of smaller spot-sizes encroach on the up-stand and progressively reduce its size and width. To optimise the parameters of the 'Tool lift', a numerical model was presented to predict the edge profile, based on empirical influence function data. To obtain the full tool influence function in the edge zone, a novel hybrid-measurement method was presented, which uses both simultaneous phase interferometry and profilometry.

In order to avoid edge asymmetry on the hexagonal part at the final stage, the causes for the asymmetry have been investigated. A strategy that can avoid the edge asymmetry has been demonstrated by experiments. Therefore, two process-chains given substantial different depth of removals have been developed and considered as top-level strategies for manufacturing E-ELT's prototype segments.

8.2 Proposed future works

8.2.1 Small tool for local edge rectification

In the final results presented in **Chapter 7** (as shown in **Figure 7.9** and **Figure 7.15**), the dominant edge-defect remaining in the PV numbers is the turning-up of the corners. It is believed that the use of a rigid pitch tool must polish the edges more than the corners, because the overlap at the corner is less. This leaves raised corners. This factor indicates that it needs local treatment in the edge zone using a small tool (e.g. R20mm tool / 5mm spot size), as shown in **Figure 8.1**.
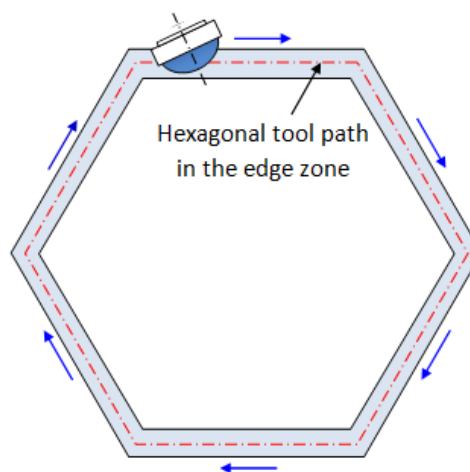
Figure 8.1 The diagram of the edge zone local treatment using hexagonal tool path (drawn by the author)

To establish its feasibility, the removal function for an R20mm tool / 5mm spot size has been tested by polishing three wedges trenched into a part with different feed rates. The test conditions were: 0.15mm Z-offset (5mm spot-size); Head-speed 800 rpm; 15° precess angle; slurry density 1.02; polyurethane polishing cloth and Zerodur glass. The cross sections of the three trenches were measured using the Form-Talysurf, as shown in **Figure 8.2**.
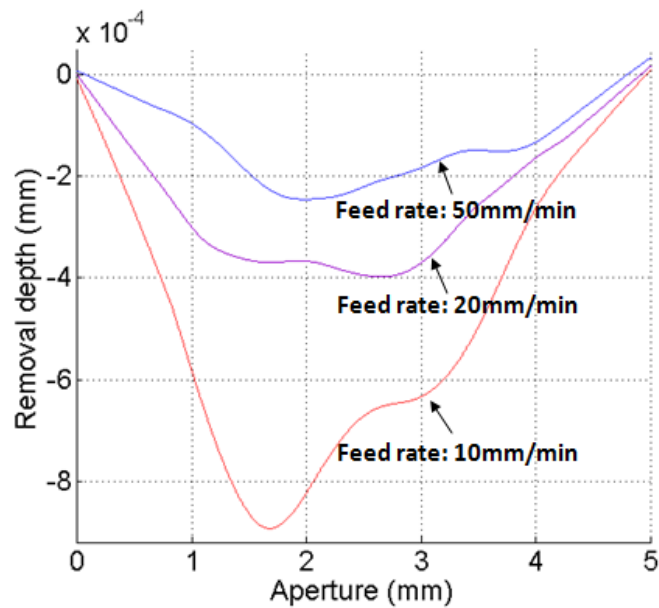
Figure 8.2 The removal trench test for R20mm tool/5mm spot-size (author's data)

A model that can predict the edge profile after local edge zone polishing was established. In this model, only a constant feed rate can be accepted. **Figure 8.3** shows the modelling result after hexagonal tool path polishing with 15mm/min feed rate, 20mm tool / 5mm spot-size. It can be seen that the up-standing edge of the edge zone has been pushed-down. This demonstrated that local edge zone polishing with a small tool has the potential for final edge treatment.

The tool-lift and feed-rate moderation within the edge zone are limited by Zeeko's current software. With this proposal, Zeeko Ltd has written an extension to their standard '*Precessions*' optimisation software, in which:

1. The continuous Hex-Hex spiral tool-path is constrained to lie within the defined inner and outer boundaries of the edge-zone.

2. The software - extension allows the user to specify different tool-lift parameters for the inner and outer boundaries.

3. Given a family of measured influence functions for a range of tool-lift parameters, the extension is able to compute the numerically optimum dwell-time map (and so feed-rates) for the tool-lift parameters as specified.

This software extension has been completed, and is now waiting for the experimental test on a machine.
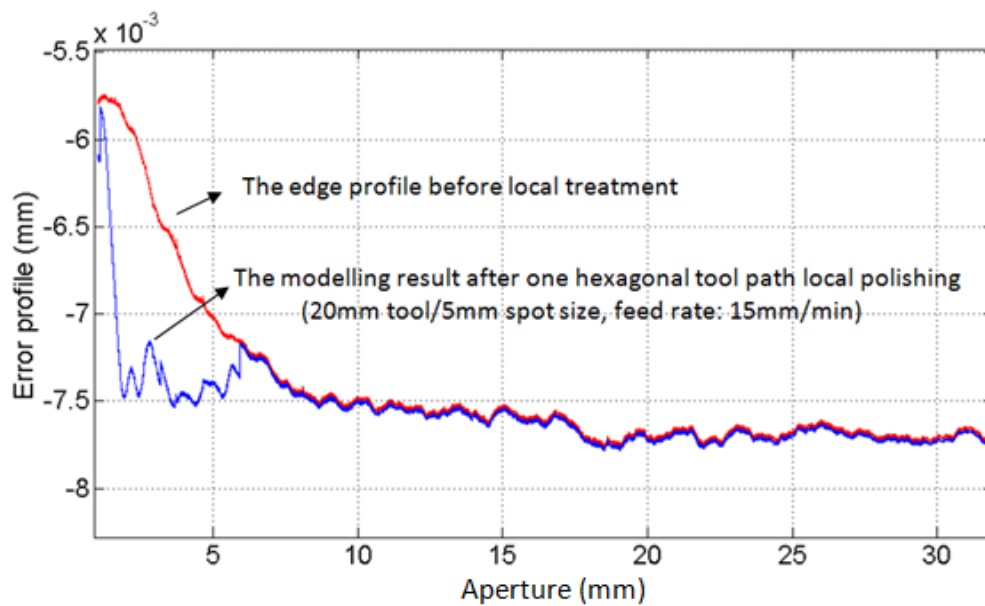
Figure 8.3 The modelling result after hexagonal tool path local polishing (R20mm tool/5mm spot-size) (author's data)

8.2.2 Development on R320mm tool to speed up the process

As presented in **Chapter 7**, attributed to the use of a large tool (R160/60mm nominal spot size) for pre-polishing in process-chain 2, the overall process speed has been significantly increased. Zeeko's IRP1600 machine is designed to be able to accommodate tool sizes up to a radius of 320mm, which is able to deliver a maximum spot-size of 150mm. Thus, increasing the tool size is a potential and reasonable way to speed up the whole process for the manufacturing of the segments.

A R200mm solid rubber tool has been designed and successfully moulded at OpTIC, as shown in **Figure 8.4**. The tool influence functions (TIFs) were tested on a Zerodur part. The testing parameters were 2.25 mm Z-offset (60mm nominal spot size), 15° Precess angle, 800 rpm Head speed, 10 seconds testing time, Polyurethane cloth, Slurry density 1.02. The 2D Talysurf measurements are shown in **Figure 8.5**. The volumetric removal rate is calculated as 14.2mm^3/min.

For comparison, the removal rate of an R160mm solid rubber tool (currently in use) with a 60mm nominal spot size is 8.61 mm^3/min (experiment conditions are the same as the R200mm tool). Therefore, a 1.65 gain in volumetric removal rate was achieved from increasing the tool size from R160mm to R200mm. It has been seen that the measured spot size of the R200mm tool is approximately 53mm (60mm nominal spot size) and the measured spot size of the R160mm tool is approximately 44mm (60mm nominal spot size). Currently, design work on the R320mm solid rubber tool is in progress.

Figure 8.4 New R200mm solid rubber tool with Polyurethane cloth on the IRP 1200 machine (author's picture, 2012)
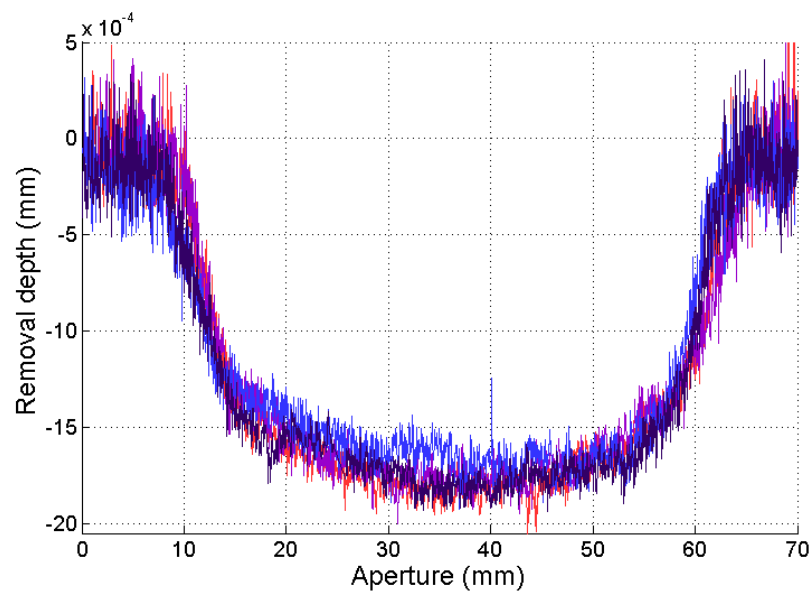
Figure 8.5 2D tool influence functions of the R200mm solid rubber tool (Z-offset: 2.25mm, 60mm nominal spot size, Precess angle: 15°, Head speed: 800rpm, Testing time: 10 seconds) (author's data)

Appendix

Removal rate table for the process

The tests in the table below were under same conditions of H axis speed 800 rpm, Precess angle 15°.

A1 The removal rate table

Bonnet	Test dwell Time (seconds)	Z-offset (mm)	Nominal spot size (mm)	Measured spot full width(mm)	Slurry density	Force (Kg)	Volumetric removal rate (mm^3/min)
R200 solid rubber tool with polyurethane	10	2.25	60	53	1.023	27.9	14.320
R160 solid rubber tool with polyurethane	10	2.8	60	43	1.023	15.9	8.607
R160 filled silicone with polyurethane	5	2.8	60	45	1.025		7.785
R160 inflated with polyurethane with 1 bar	5	2.8	60	51	1.025	7.7	5.249
R80 inflated with polyurethane with 1 bar	60	1.4	30	25	1.028	2.4	1.230
	120	0.7	20	16	1.028	1.7	0.583
R80 Solid rubber tool with polyurethane	10	1.4	30	25	1.022	14.9	4.961
	10	0.7	20	17	1.022	4.4	2.045
R80 Solid rubber tool with Uni-Nap	10	0.7	20	16	1.022		0.326

List of Publications

1. H. Li, G. Yu, D. D. Walker, Evans. R. Modelling and measurement of polishing tool influence functions for edge control. *Journal of the European Optical Society-Rapid Publications*, vol.6 2011

2. G. Yu, H. Li, D. D. Walker. Removal of mid spatial-frequency features in mirror segments. *Journal of the European Optical Society-Rapid Publications*, vol.6, 2011

3. D. D. Walker, G. Yu, H. Li. Research in new polishing techniques for off-axis mirror segments. *Proc. ASPE*: American Society for Precision Engineering, vol.52,2011

4. G. Yu, D. D. Walker, H. Li. Research on Fabrication of Mirror Segments for E-ELT. *Proc. SPIE* : Advanced Optical Manufacturing and Testing Technologies 2012 (editing)

5. W. Wang, M. Xu, H. Li, G. Yu. Polishing Large-Aperture Mirror Using Ultra-Precise Bonnet and PSD Result Analysis. *Proc. SPIE* : Advanced Optical Manufacturing and Testing Technologies 2012 (editing)

6. D. D. Walker, A. Beaucamp, G. Yu, H. Li. Edge-control on mirror segements. *Optical Fabraction and Testing*, Optical Society of America, 2010

7. D. D. Walker, C. Atkins, I. Baker, R. Evans, S. Hamidi, P. Harris, H. Li, W. Messelink, J. Mitchell, M. Parry. Jones, P. Rees, G. Yu. Technologies for producing segments for extremely large telescopes' *Proc. SPIE*: Optical Manufacturing and Testing IX, vol.8126 2011

8. D. D. Walker, G. Yu, H. Li, W. Messelink, R. Evans, A. Beaucamp. Edges in CNC polishing: from mirror-segments, towards semiconductors. Paper 1: edges on processing the global surface. (submitted to *Optics Express*)

Bibliography

Abdulkadyrov, M., Belousov, S., Ignatov, A., Patrikeev, A., Patrikeev, V., Pridnya, V, Polyanchikov, A., Rumyantesev, V., Samuylov, A., Semenov, A. and Sharov, Y. (2004). Fabrication of blank, figuring and testing of solid and segmented astronomical mirrors. *Proc. SPIE*, **5382,** pp. 296-304.

Amodei, D. and Padin, S. (2003). Mirrors with regular hexagonal segments. *Applied optics*, **42**(25), pp. 5130-5135.

Anderson, D., Angel, J., Burge, J., Davison, W., DeRigne, S., Hille, B., Ketelsen, D., Kittrell, W., Martin, H., Nagel, R., Trebisky, T., West, S., and Young, R. (1991). Stressed-lap polishing of a 3.5-m f/1.5 and 1.8-m f/1.0 mirrors. *Proc. SPIE*, **1531**, pp. 260-269.

Andersen T., Ardeberg, A., Beckers, J., Goncharov, A., Petersen, M., Riewaldt, H., Snel, R., Walker, D. (2003). 'The Euro 50 Extremely Large Telescope' in Future Giant Telescopes, Editors: J. R. P. Angel, R. Gilmozzi, *Proc. SPIE* , **4840**, pp. 214-225.

ANSYS, (2011). The history of ANSYS introduction, online, [Accessed on 16th, December, 2011]; Available form: http://www.ansys.com/en_uk

Alvarez, P., Castro, J., Rutten, R., Hoeven, M., Alvarez, C. and Perez-García.(2010) A. The GTC Project: from commissioning to regular science operation. Current performance and first science results. *Proc. SPIE*, **7733**, pp. 77330501-15.

Baade, W. (1948). A program of extragalactic research for the 200 inch Hale telescope. *Publications of the Astronomical Society of the Pacific*, **60**(355), pp. 230-233.

Babcock, H. (1953). The possibility of compensating astronomical seeing. *Publications of the Astronomical Society of the Pacific*, **65**(386), pp. 229-236.

Barker, P. Edited and corrected based on the version by Carlos, E. S. London, 1880. (2004).

Sidereus Nuncius. Oklahoma city: Byzantium Press.

Bastaits, R. (2010). Extremely large segmented mirrors: dynamics, control and scale effects. Thesis (Ph.D.), University Libre de Bruxelles (ULB).

Bely, P. Y. (2003). The Design and Construction of Large Optical Telescopes. Springer.

Bingham, R. G., Walker, D. D., Kim, D-H., Brooks, D., Freeman, R. and Riley, D. (2000). A Novel Automated Process for Aspheric Surfaces. *Proc. SPIE*: 45th Annual Meeting, the International Symposium on Optical Science and Technology, **4093**, pp. 445-448.

Bougoin, M. and Deny, P. (2004). The SiC Technology is ready for the next generation of rxtremely large telescopes. *Proc. SPIE*, **5494**, pp. 9-18.

Burge, J. H., Benjamin, S., Caywood, D., Noble, C., Novak, M., Oh, C., Parks, R., Smith, B., Su, P., Valente, M. and Zhao, C. (2009). Fabrication and testing of 1.4m convex off-axis aspheric optical surfaces. *Proc. SPIE,* **7426**, pp. 74260L1-10.

Brug, H., Groeneveld, M., Booij, S. M. and Braat, J. J. M. (2002). In-process measurements of material removal influid jet polishing. *Proc. SPIE,* **4778**, pp. 243-250.

Cayrel, M., Paquin, R. A., Parsonage, T. B., Stanghellini, S. and Dost, K. H. (1996). Use of Beryllium for the VLT secondary Mirror. *Proc. SPIE*, **2857**, pp. 86-98.

Canales, V. F., Oti, J. E., Valle, P. J. and Cagigal, M. P. (2006). Reduction of the diffraction pattern in segmented apertures. *Optical Engineering*, **45**(9), pp. 098001-1-6.

Celotti, A., Miller, J. and Sciama, D. (1999). Astrophysical evidence for the existence of black hole. *Classical and Quantum Gravity*, **16**(12A), pp. A3-A21.

Chen, M., Feng, Y. , Wan, Y., Li, T. and Fan. B. (2010). Neural network based surface shape modelling of stressed lap optical polishing. *Applied optics*, **49**(8), pp. 1350-1354.

Cordero-Davila, A., Gonzalez-Garcia, J., Pedrayes-Lopez, M., Aguilar-Chiu, L. A., Cuautle-Cortes, J. and Robledo-Sanchez, C. (2004). Edge effects with the Preston equation for a

circular tool and workpiece experiment. *Applied optics*, **43**(6), pp. 1250-1254.

Cranfield University. 2011, personal communication.

Cunningham, C. (2009), The European Extremely Large Telescope. *INGENIA*, **39**

Dai, G. and Mahajan, V. (2008). Orthonormal polynomials in wavefront analysis: error analysis. *Applied optics*, **47**(19), pp. 3433-3445.

DeMarco, M. (2005). Optical manufacturing with Magneto-Rheological Finishing (MRF). Optifab 2005: Technical Digest, *Proc. SPIE*, **TD03**, pp. 28-30.

Deng, X., Li, Y., Fan, D. and Qiu Y. (1997). A fast algorithm for fractional Fourier transforms. *Optics Communications*, **138**(4-6), pp. 270-274.

Dohring, T., Hartmann, P., Jedamzik, R. and Thomas, A. (2004). ZERODUR Mirror Blank for ELTs: Technology and production Capacity at SCHOTT. *Proc. SPIE*, **5382**, pp. 285-295.

Dohring, T., Hartmann, P., Jedamzik, R., Thomas, A. and Lentes, F. T. (2006). Properties of Zerodur mirror blank for Extremely Large Telescopes. *Proc. SPIE*, **6148**, pp. 61480G1-G8.

Dierickx, P. (2000). Optical fabrication in the large. At editors: Andersen, T. Ardeberg, A and Gilmozzi, R. Workshop on extremely large telescopes, pp. 224.

Drueding, T. W., Fawcett, S. C., Wilson, S. R. and Bifano, T. G. (1995). Ion beam figuring of small optical components. *Optical Engineering*, **34**(12), pp. 3565-3571.

Dunn, C. R. (2008A). Pseudo-random tool paths for sub-aperture polishing technologies. Thesis (Ph.D.), University College London.

Dunn, C. R. and Walker, D. D. (2008B). Pseudo-random tool paths for CNC sub-aperture polishing and other applications. *Optics Express*, **16**(23), pp. 18942-18949.

ESO, (2001). E-ELT programme: technical specifications for polishing, integration and final figuring of the segment assemblies of the primary mirror of the E-ELT. E-SPE-ESO-300-1048,

ISSUE 1

Edward, E. M. and Glenn, W. Z. (1998). The case for segmentation of the primary mirror of large aperture space telescopes. *Proc. SPIE*, **3356**, pp. 788-798.

Enard, D., Marechal, A. and Espiard, J. (1996). Progress in ground-based optical telescopes. *Rep. Prog. Phys*, **59**

Espinosa, J. M. and Alvarez, P. (1997). Gran Telescopio Canarias: a 10-m telescope for the ORM. *Proc. SPIE*, **2871**, pp. 69-73.

Fähnle, O. W. (1998A). Shaping and finishing of aspherical optical surfaces. Thesis (Ph.D.), Technische Universiteit Delft.

Fähnle, O. W., Brug, H. and Frankena, H. (1998B). Fluid jet polishing of optical surfaces. *Applied optics*, **37**(28), pp. 6771-6773.

Fähnle, O. W. and Brug, H. (1999). Novel approaches to generate aspherical optical surfaces. *Proc. SPIE*, **3782**, pp. 170-180.

Fanara, C., Shore, P., Nicholls, J. R., Lyford, N., Sommer, P. and Fiske, P. (2006A). A New Reactive Atom Plasma Technology (RAPT) for precision machining: the etching of ULE optical surfaces. *Proc. SPIE*, **6273**, pp. 62730A-1-12.

Fanara, C., Shore, P., Nicholls, J., Lyford, N., Kelley, J., Carr, J. and Sommer, P. (2006b). A new Reactive Atom Plasma Technology (RAPT) for precision machining: the etching of ULE surfaces. *Advanced Engineering Materials*, **8**(10), pp. 933-939.

Flores, J. L., Paez, G. and Strojnik, M. (2003). Optimal aperture configuration for a segmented and partially diluted extremely large telescope. *Journal of modern optics*, **50**(5), pp. 729-742.

Frank, T., Lotz, M., Hackel, T., Theska, R. and Höhne, G. (2005). Extreme light weight stage mirrors for precision positioning combining silicon and Zerodur. *Proc. ASPE*, 20th Annual meeting.

Gale, A. L. (1978). Ion machining of optical components. *Optical Society of America Ann,* **68**, pp. 1445-1446.

Geyl, R., Cayrel, M. and Tarreau, M. (2004). Glan Tlescope Canarias optics manufacture: Progress report3. *Proc. SPIE*, **5494**, pp. 57-61.

Gilmozzi, R. (2004). Science and technology drivers for future giant telescopes. *Proc. SPIE*, **5489**, pp. 1-10.

Glaswerke S. (2006). Zerodur Glass Ceramic, SCHOTT report.

Golini, D., Kordonski, W. I., Dumas, P. and Hogan, S. (1999). Magnetorheological finishing (MRF) in commercial precision optics manufacturing. *Proc. SPIE* , **3782**, pp. 80-91.

Golini, D., DeMarco, M., Kordonski, W. and Bruning, J. (2001). MRF polishes calcium fluoride to high quality. *Laser Focus World*, July.

Gonzalez-Garcıa, J., Davila, A. C., Luna, E., Nunez, M., Luis Salas, E. R., Cabrera-Pelaez, V. H., Cruz-Gonzalez, I. and Sohn, E. (2004). Static and dynamic removal rates of a new hydrodynamic polishing tool. *Applied optics*, **43**(18), pp. 3623-3631.

GTC. (2011). Grab Telescopio Canaria website, online, Available form: http://www.gtc.iac.es/en/ [Accessed on 24th, October, 2011].

Guo, P., Fang, H. and Yu, J. (2006). Edge effect in fluid jet polishing. *Applied optics*, **45**(26), pp. 6729-6735.

Harris, D. C. (2011). History of Magnetorheological Finishing. *Proc. SPIE*, **8016**, pp. 80160N01-22.

Hartmann, P. and Dohring, T. (2006). 'Mirror Blank Production for ELTs' SCHOTT, report,

HET. (2011). Hobby-Eberly Telescope, online, Available form: http://hetdex.org/ [Accessed on 20th, October, 2011]

Hook, I. (2004). Highlights from the science case for a 50- to 100-m extremely large telescope. *Proc. SPIE*, **5489**, pp. 35-46.

Hook, I. and the OPTICAN ELT Science Working Group. (2005). Science with Extremely Large Telescopes. *The Messenger 121*

Hou, X., Wu, F. Y, L. and Chen, Q. (2006). Comparison of annular wavefront interpretation with Zernike circle polynomials and annular polynomials. *Applied optics*, **45**(35), pp. 8893-8901.

Hu, H., Dai, Y., Peng, X. and Wang, J. (2011). Research on reducing the edge effect in magnetorheological finishing. *Applied optics*, **50**(9), pp. 1220-1226.

Iye, M. and Nishimura, T. (1994). Scientific and engineering frontiers for 8-10m telescopes. *Frontiers science* series **14**, Tokyo, Japan, Universal Academic Press,

Jacobs, S. D., Golini, D., Hsu, Y., Puchebner, B. E., Strafford, D., Kordonski, W. I., Prokhorov, I. V., Fess, E., Pietrowski, D. and Kordonski, V. W. (1995). Magnetorheological finishing: a deterministic process for optics manufacturing in Optical Fabrication and Testing, *Proc. SPIE* **2576**, pp. 372-383.

Jacobs, S. D., Kordonski, W. I., Prokhorov, I. V., Golini, D., Gorodkin, G. R. and Strafford, T. D. (1998). Deterministic magnetorheological finishing. U.S. patent 5,795,212.

Jacobs, S. D. (2004). International innovations in optical finishing in *Current Developments in Lens Design and Optical Engineering V*, edited by Mouroulis, P. Z., Smith, W. J. and Johnson, R. B. (SPIE, Bellingham, WA, 2004), *Proc. SPIE*, **5523,** pp. 264-272.

Jing, H., King, C. and Walker, D. D. (2010). Measurement of influence function using swing arm profilometer and laser tracker. *Optics Express*, **18**(5), pp. 5271-5281.

Jones, R. A. (1977). Optimization of computer controlled polishing. *Applied optics*, **16**(1), pp. 218-224.

Jones, R. A. (1978). Fabrication using the computer controlled polisher. *Applied optics*,

17(12), pp. 1889-1892.

Jones, R. A. (1982). Segmented mirror polishing experiment. *Applied optics*, **21**(3), pp. 561-564.

Jones, R. A. (1986). Computer-controlled optical surfacing with orbital tool motion. *Optical Engineering*, **25**(6), pp. 785-790.

Jones, R. A. and Rupp, W. (1991). Rapid optical fabrication with computer-controlled optical surfacing. *Optical engineering*, **30**(12), pp. 1962-1969.

KECK Observatory. (2011). 'Keck's Mirror' online, Available form: http://keckobservatory.org/about/mirror [Accessed on 11th, December, 2011]

Kendrew, S. (2006). Lightweight deformable mirrors for ground- and space-based imaging systems. Thesis (Ph.D.), University College London.

Kendrick, S. E. (2009). Monolithic versus segmented primary mirror concepts for space telescopes. *Proc. SPIE*, **7426**, pp. 74260O1-12.

Kim, H. (2000). On the removal of material for polishing aspheric optics. Thesis (Ph.D.), University College London.

Kim, D. W., Kim, S. W., Jones, R. and Rupp, W. (2005). Static tool influence function for fabrication simulation of hexagonal mirror segments for extremely large telescope. *Opt. Express*, **13**(3), pp. 910-917.

Kim, D. W., Park, W. H., Kim, S. W. and Burge, J. (2009). Parametric modelling of edge effects for polishing tool influence functions. *Opt. Express*, **17**(7), pp. 5656-5665.

Kishi, T., Goto, N., Kawashima, Y., Suzuki, K., Yoshizawa, K. and Suzuki, K. (2010). Material characteristics of CLEARCERAM-Z HS for use in large diameter mirror blanks. *Proc. SPIE*, **7739**, pp. 77390K01-09

Kordonski, W., Shorey, A. and Sekeres, A. (2003). New magnetically assisted finishing

method: material removal with magneto-rheological fluid jet in Optical Manufacturing and Testing. *Proc. SPIE*, **5180**, pp. 1077-114

Krabbendam, V. L., Sebring, T. A., Ray, F. B. and Fowler, J. R. (1998). Development and performance of Hobby-Eberly Telescope 11-m segmented mirror. *Proc. SPIE*, **3352**, pp. 436-445.

Lee, H. (2010). Use of Zernike polynomials for efficient estimation of orthonormal aberration coefficients over variable noncircular pupils. *Optics letters*, **35**(13), pp. 2173-2175.

Li, Z., Li, S., Dai, Y. and Peng, X. (2010). Optimization and application of influence function in abrasive jet polishing. *Applied optics*, **49**(15), pp. 2947-2953.

Li, Z., Wang, J., Peng, X., Li, S. and Yin, Z. (2010). Abrasive jet polishing and its application in surface finishing. *American Journal of Manotechnology*, **1**(2), pp. 86-93.

Lin, C., Kuo, C., Lai, C., Tsai, M., Chang, Y. and Cheng, H. (2011). A novel approach to fast noise reduction of infrared image. *Infrared Physics & Technology*, **54**(1), pp. 1-9.

Love, G. and Saxena, A. K. (1994). Active and adaptive optics for the new generation of large telescopes. *CURRENT SCIENCE*, **66**(5), pp. 349-355.

Love, G., Myers, R., Wilson, R., Buscher, D., Butterley, T. and Morris, T. (2004). Sensing the atmosphere on the upward path: LGSs without FA for ELTs. *Proc. SPIE*, **5382**, pp. 462-467.

Lubliner, J. and Nelson, J. E. (1980). Stressed mirror polishing. 1: A technique for producing nonaxisymmetric mirrors. *Applied optics*, **19**(14), pp. 2332-2340.

Malacara, D. and Thompson, B. J. (2001). Handbook of optical engineering. Marcel Dekker, Inc..

Martin, H. M. (1990). Aspheric polishing with a stressed lap. *Optics and Photonics News*, **1**(6), pp. 22-24.

Martin, H. M., Burge, J., Cuerden, H. B., Miller, S. M., Smith, B. and Zhao, C. (2004). Manufacture of 8.4m off-axis segments: a 1/5 scale demonstration. *Proc. SPIE*, **5494**, pp. 62-

70.

Martin, H. M., Allen, R. G., Cuerden, B., Hill, J. M., Ketelsen, D. A., Miller, S. M., Sasian, J. M., Tuell, M. T. and Warner, S. (2006). Manufacture of the second 8.4m primary mirror for the Large Binocular Telescope. *Proc. SPIE*, **6273**, pp. 62730C1-10.

Marra, M. (2000). New astronomy library in Bologna is named after Guido Horn D'Arturo: a forefather of modern telescopes. *Journal of the British Astronomical Association*, **110**(2), pp. 110-88.

Mast, T. S and Nelson, J. E. (1982). Figure control for a fully segmented telescope mirror. *Applied optics*, **21**(14), pp. 2631-2641.

Mast, T. S. and Nelson, J. E. (1990). The fabrication of large optical surface using a combination of polishing and mirror bending. In Advanced technology optical telescope IV. editor: Barr, L. D. **1236**, pp. 670-681.

Matson, L. E. and Mollenhauer, D. H. (2004). Advanced materials and processes for large, lightweight, space-based mirrors. *The AMPTIAC Quarterly*, **8**, pp. 67-74

Meiring, J. G., Buckley, D. A. H., Lomberg, M. C. and Stobie, R. S. (2003). Southern African Large Telescope (SALT) project: progress and status after two years. *Proc. SPIE*, **4837**, pp. 11-26

Nelson, Gabor, J., G., Hunt, L. K., Lubliner, J. and Mast, T. S. (1980). Stressed mirror polishing 2: Fabrication of an off-axis section of a paraboloid. *Applied optics*, **19**(14), pp. 2341-2352.

Nelson, J. E. and Gillingham, P. (1994). An overview of the performance of the W. M. Keck Observatory. *Proc. SPIE*, **2199**, pp. 82-93.

Nelson,J. E. (2000). Design concepts for the California Extremely Large Telescope (CELT). *Proc. SPIE*, **4004**, pp. 282-289.

Nelson, J. E. (2005). Segmented mirror Telescopes in Optics in astrophysics, NATO Science Series, II. Mathematics, *Physics and Chemistry,* **198**, Springer, pp. 61.

Bibliography

NPG. (2001). Nature Publishing Group. Encyclopaedia of astronomy and astrophysics. Institute of Physics Publishing

OHARA. (2012). 'CSR Report 2010' online OHARA company official website., Available form: http://www.ohara-inc.co.jp [Accessed on 20th, March, 2012]

OSA. (2011). Optical Society of America Rochester university section. Optical polishing pitch. online, Available form: http://www.opticsexcellence.org/SJ_TeamSite/RS_polPitch.html [Accessed on 11th, December, 2011]

Oschmann, J. M. and Simons, D. A. (1997). Gemini 8-m telescopes performance estimates opdate. *Proc. SPIE*, **2871**, pp. 88-99.

Pantin, E. (2012). Observations of proto-planetary disks with the JWST/MIRI and the E-ELT/METIS instruments' online, Available form: http://www.eso.org/sci/facilities/eelt/ [Accessed on 26th, January, 2012]

Parsonage, T. (2004). JWST Beryllium Telescope: Material and substrate fabrication. *Proc. SPIE*, **5494**, pp. 39-48.

Palunas, P., MacQueen, P., Booth, J., Calder, R., Fowler, J., Shetrone, M., Odewahn, S., Segura, P., Wesley, G., Damm, G., Martin, J. and Odoms, P. (2006). Imaging performance of the Hobby-Eberly Telescope. *Proc. SPIE*, **6267**, pp. 62673V-1-9.

Pollicove, H., Jacobs, S. D., Ruckman, J. and Richard, M. (2000). Next Generation Optics Manufacturing Technologies. *Proc. SPIE*: Advanced Optical Manufacturing and Testing Technology, **4231**, pp. 8-14

Ponin, O., Sharov, A., Galyavov, I., Kopan, T. Swiegers, J. and Swat, A. (2003). Demonstrating the suitability of Sitall for the SALT primary mirror. *Proc. SPIE*, **4837**, pp. 795-804

Preumont, A., Bastaits and Rodrigues, R. G. (2009). Scale effects in active optics of large segmented mirrors. *Mechatronics,* **19**(8), pp. 1286-1293.

Preston, F. W. (1927). The theory and design of plate glass polishing machines. *J. Glass*, **11**,

pp. 214-257.

Prokhorov, I. V., Kordonsky, W. I., Gleb, L. K., Gorodkin, G. R. and Levin, M. L. (1992). OSA Optical fabrication and Testing Workshop.

Ramsay, S., D'Odorico, S., Casali, M,. González, J. C., Hubin, N., Kasper, M., Käufl, H.U., Kissler-Patig, M., Marchetti, E., Paufique, J., Pasquini, L., Siebenmorgen, R., Richichi, A., Vernet, J. and Zerbi, F. M. (2010). An overview of the E-ELT instrumentation programme. *Proc. SPIE*, **7735**, pp. 7735241-15

Roggemann, M. and Welsh, B. (1994). Signal-to-noise for astronomical imaging by deconvolution from wave-front sensing. *Applied optics*, **33**(23), pp. 5400-5414.

Ruch, E. (2011). The challenge of the Optics in Future Extremely Large Telescopes. in '*Astronomy at the Frontiers of Science'* pp. 229, Springer.

Sabia, R., Edwards, M., Brocklin, R. and Wells. B. (2006). Corning 7972 ULE material for segmented and large monolithic mirror blanks. *Proc. SPIE*, **6273**, pp. 627302-1-8.

Salinas-Luna, J., Machorro, R., Camacho, J., Luna, E. and Nunez, J. (2006). Water jet: a promising method for cutting optical glass. *Applied optics*, **45**(15), pp. 3477-3481

SALT. (2011). The Southern African Large Telescope, online, Available form: http://www.salt.ac.za [Accessed on 24th, October, 2011]

Sanders, G. H. (2008). Managing a big ground-based astronomy project: the Thirty Meter Telescope (TMT) project. *Proc. SPIE*, **7017**, pp. 70170H1-11.

Schinhael, M., Geiss, A. and Rascher, R. (2006). Cohence between influence function size, polishing quality and process time in the magnetorheological finishing. *Proc. SPIE*, **6288**, pp. 62880Q1-09.

Schulz, G. (1987). Imaging performance of aspherics in comparison with spherical surfaces. *Applied optics*, **26**(23), pp. 5118-5124

Semenov, A. P., Abdulkadyrov, M. A., Ignatov, A. N. and Patrikeev, V. (2004). Fabrication of blank, figuring, polishing and testing of segmented astronomic Mirrors for SALT AND LAMOST project. *Proc. SPIE*, **5494**, pp. 31-38.

Spano, P., Zerbi, F. M. and Norrie, C. J. (2006). Challenges in optics for Extremely Large Telescope instrumentation. *Astron. Nachr*, **327**(7), pp. 649-673.

Stark, A. A., Chamberlin, R. A., Ingalls, J. G., Cheng, J. and Wright, G. (1997). Optical and mechanical design of the Antarctic sub-millimetre telescope and remote observatory. *Rev. Sci. Instrum.* **68**(5), pp. 2200-2213.

Storm, S. E., Stepp, L. M. and Gregory, B. (2003). Giant Segmented Mirror Telescope: a point design based on science drivers. *Proc. SPIE*, **4840**, pp. 116-128.

Subrahmanyan, P. K. and Gardopee, G. (2008). Reactive atom plasma (RAPTM) processing of mirrors for astronomy. *Proc. SPIE*, **7018**, pp. 70180901-12.

Tobin, W. (1987). Foucault's invention of the silvered-glass reflecting telescope and the history of his 80-cm reflector at the observatoire de Marseille. *Vistas in Astronomy*, **30**, pp. 153-184.

Tokunaga, A. T. and Jedicke, R. (2007). New Generation Ground-Based Optical/Infrared Telescopes' in Encyclopaedia of the Solar system 2nd edition, Academic Press.

Tricard, M., Shorey, A., Hallock, B. and Murphy, P. (2006). Cost-effective, sub-aperture approaches to finishing and testing astronomical optical. *Proc. SPIE* **6273**, pp. 62730L01-10.

Troy, M. and Chanan, G. (2003). Diffraction effects from giant segmented mirror telescopes. *Applied optics*, **42**(19), pp. 3745-3756.

Wagner, R. E. and Shannon, R. R. (1974). Fabrication of aspherics using a mathematical model for material removal. *Applied optics*, **13**(7), pp. 1683-1689.

Walker, D. D., Freeman, R., McCavana, G., Morton, R., Riley, D., Simms, J., Brooks, D., Kim, E. and King, A. (2001A). Zeeko/UCL process for polishing large lenses and prisms. *Proc. SPIE*:

Large Lenses and Mirrors conference, **4411**, pp. 106-111.

Walker, D. D., Brooks, D., Freeman, R., King, A., McCavana, G., Morton, R., Riley, D. and Simms, J. (2001B). The first aspheric form and texture results from a production machine embodying the *'Precession'* process'. *Proc. SPIE*: 46th Annual Meeting of SPIE, **4451**, pp. 267-276.

Walker, D. D., Brooks, D., King, A., Freeman, R., Morton, R., McCavana, G. and Kim, S. (2003). The '*Precessions*' tooling for polishing and figuring flat, spherical and aspheric surfaces. *Optics Express*, **11**(8), pp. 958-967.

Walker, D. D., Beaucamp, A. T. H., Brooks, D., Doubrovski, V., Cassie, M., Dunn, C., Freeman, R., King, A., Libert, M., McCavana, G., Morton, R., Riley, D. and Simms, J. (2004). New results from the *'Precessions'* polishing process scaled to larger sizes. *Proc. SPIE*: Optical Fabrication, Metrology, and Material Advancements for Telescopes, **5494**, pp. 71-80.

Walker, D. D., Beaucamp, A. T. H., Doubrovski, V., Dunn, C., Freeman, R., McCavana, G., Morton, R., Riley, D., Simms, J. and Wei, X.(2005). New results extending the '*Precessions'* process to smoothing ground aspheres and producing freeform parts. *Proc. SPIE*: Optical Manufacturing and Testing VI, **5869**, pp. 79-87.

Walker, D. D., Beaucamp, A. T. H., Doubrovski, V., Dunn, C., Evans, R., Freeman, R., Kelchner, J., McCavana, G., Morton, R., Riley, D., Simms, J., Yu, G. and Wei, X. (2006A). Automated optical fabrication: first results from the new Precessions 1.2m CNC polishing machine. *Proc. SPIE*: Opt mechanical Technologies for Astronomy, **6273** pp. 62730901-08.

Walker, D. D., Beaucamp, A. T. H., Doubrovski, V., Dunn, C., Evans, R., Freeman, R., McCavana, G., Morton, R., Riley, D. and Simms, J. (2006B). Commissioning of the first '*Precessions*' 1.2m CNC polishing machines for large optics. *Proc. SPIE*: Current Developments in Lens Design and Optical Engineering, **6288**, pp. 62880P.

Walker, D. D., Freeman, R., Morton, R., McCavana, G. and Beaucamp, A. T. H. (2006C). Use of the *Precessions* ^TM^ process for pre-polishing and correcting 2D &2.5 D form. *Optics Express*, **14**(24), pp. 11787-11796.

Walker, D. D., Baldwin, A., Evans, R., Freeman, R., Hamidi, S., Shore, P., Tonnellier, X., Wei,

S., Williams, C. and Yu, G. (2007). A Quantitative comparison of three grolishing techniques for the *Precessions* ™ process. **6671**, pp. H-1-9.

Walker, D. D., Beaucamp, A. H., Dunn, C., Evans, R., Freeman, R., Morton, R., Wei, S. and Yu, G. (2008). Active control of edges and global microstructure on segmented mirrors. *Proc. SPIE*, **7018** pp. 701812-1-9.

Walker, D. D., Yu, G. and Li, H. (2011A). Research in new polishing techniques for off-axis mirrors segments. *Proc. ASPE*: American Society for Precision Engineering, **52**, pp. 31-34.

Walker, D. D., Atkins, C., Baker, I., Evans, R., Hamidi, S., Harris, P., Li, H., Messelink, W., Mitchell, J., Jones, M. P., Rees, P. and Yu, G. (2011B). Technologies for producing segments for extremely large telescopes. *Proc. SPIE*: Optical Manufacturing and Testing IX, **8126** pp. 812604-13.

Walker, D. D. (2011C). The internal report: The draft on the investigation edge asymmetry.

Walker, D. D. (2012A). The personal communication. January, 2012

Walker, D. D. (2012B). The internal report for ESO meeting. January, 2012

Walker, D. D. (2012C). The personal communication. February, 2012

Wang, B., Yan, J., Zhang, X. and Gu, Y. (2007). Edge effects on the diffraction of the segmented aperture. *Proc. SPIE*, **6625**, pp. 66250S1-9.

Wilson, R. N., Franza, F. and Noethe, L. (1987). Active Optics I. A system for optimizing the optical quality and reducing the costs of large telescopes. *Journal of Modern Optics,* **34**(4), pp. 485-509.

Wilson, S. R. and McNeil, J. R. (1987). Neutral ion beam figuring of large optical surfaces. in Current Developments in Optical Engineering, *Proc. SPIE*, **818**, pp. 320-323.

Wilson, R. N. (2004). Reflecting Telescope Optics I, Second Edition. Springer.

Yaitakova, N., Dohlen, K. and Dierickx, P. (2003). Diffraction in OWL: Effects of segmentation and segments edge mis-figure. *Proc. SPIE*, **4840**, pp. 171-182.

Yaitakova, N. and Troy, M. (2011). Rolled edges and phasing of segmented telescopes. *Applied optics*, **50**(4), pp. 542-553.

Yuan, X. and Wang, X. (1999). Precision and ultra-precision technology. pp. 2-8, Beijing, China Machine Press.

Yu, G., Li, H. and Walker, D. D. (2011). Removal of mid spatial-frequency features in mirror segments. *Journal of the European Optical Society-Rapid Publications*, **6**, pp. 1104401-04.

Zeeko. (2011). Zeeko Ltd official website, online, Available form: http://www.zeeko.co.uk/ [Accessed on 16th, October, 2011]

Zeiders, G. W., Montgomery, E. E. (1998). Diffraction effects with segmented apertures. *Proc. SPIE*, **3356**, pp. 799-839.

Zernike, F. (1934). Beugungstheorie des Schneidenverfahrens und seiner verbesserten Form, der Phasenkontrastmethode. *Physica,* **1**, pp. 689-704.

Zeuner, M. and Nestler, M. (2010). Ion-beam based polishing error correction in mass production of precision optics. *Photonik*. in German.

Zhu, L., Sun, P., Bartsch, D. U., Freeman, W. R. and Faunman, Y. (1999). Wave-front generation of Zernike polynomial modes with a micro machined membrane deformable mirror. *Applied optics*, **38**(28), pp. 6019-6026.